UNIVERSIDADE DE LISBOA
FACULDADE DE CIÊNCIAS
DEPARTAMENTO DE FÍSICA

Characterisation and functional test of the full readout chain of a microdosimeter using scintillating plastic optical fibres

Matilde Maria Sobreiro Santos

Mestrado Integrado em Engenharia Física

Dissertação orientada por:
Dr. João Gentil Mendes Saraiva
Prof. Guiomar Gaspar de Andrade Evans

2021

Acknowledgments

Durante o meu percurso académico, contei com o apoio e ajuda de várias pessoas, sendo que sem elas não teria sido possível concluir esta etapa da minha vida académica. Por isso, uso esta secção para agradecer a todos eles.

Agradeço em primeiro lugar à Professora Guiomar Evans, por todo o apoio, por toda a dedicação que demonstra aos seus alunos e por ter aceitado ser a minha orientadora nesta etapa final. Agradeço também ao Dr. João Gentil, por todo o conhecimento, paciência e tempo que me dedicou durante a realização desta tese, a qual não teria sido realizada sem o seu apoio.

Ao meu colega de laboratório, Duarte Guerreiro, um obrigada pela companhia, ajuda, partilha e troca de conhecimento.

Para todas pessoas que contribuíram para a realização deste trabalho, agradeço a disponibilidade e partilha de conhecimento: Professor Luís Peralta, Professor Jorge Sampaio, Pedro Assis e Luís Gurriana.

Um agradecimento especial à Jane Ribeiro pela ajuda e última correcção do meu inglês, da qual estou bastante grata, e à Cristina Ribeiro, por ter facilitado o contacto tão prontamente.

Um obrigada enorme aos meus amigos André Sistelo, André Torcato, Bruna Sousa, Diogo Sucena, Filipa Neves, Inês André, Renato Alegria, Romeu Abreu e Sofia Mansoa, por todo o apoio e amizade durante estes últimos anos.

Às minhas grandes amigas: Beatriz Ponte, Inês Serrenho, Joana Vital, Mafalda Leal e Vanessa Machado, precisava de fazer um destaque e obrigada especial. Por saber que posso sempre contar com a vossa amizade, apoio incondicional, pelos ombros amigos e por me fazerem rir quando as circunstâncias não eram tão fáceis, agradeço-vos do fundo do coração. Espero contar sempre com vocês no futuro.

Ao João Morgado, um especial obrigada pelo amor, carinho e interminável apoio que me transmites não só durante esta fase tão difícil, mas como também durante os anos de faculdade. Obrigada também pela motivação a sair fora da minha zona de conforto, porque sei que estás sempre aqui ao meu lado.

À minha família, em especial o meu Avô Justino e o meu Pai, pelo amor e carinho que sempre me deram.

À minha Mãe, só a ti poderia dedicar esta tese. Pelo amor incondicional de mãe, experiência e conhecimento que me transmites, como também as asas para voar e explorar o mundo que me rodeia. A mulher que sou hoje, deve-se a ti e é a maior gratidão que carrego. Obrigada, Mãe.

Abstract

Instruments with a high spatial resolution are necessary to measure dosimetric quantities at a cellular level in order to have a better delineation of treatment plans in radiotherapy. The work here described is within a project aiming to develop a new detector capable of measuring real-time absorbed dose with sub-millimetre resolution. The device is constructed using juxtaposed scintillating plastic optical fibres (SPOF) readout by a multi-anode photomultiplier (MAPMT, Hamamatsu H8500D) and a data acquisition (DAQ) system. In this thesis a first validation of the full readout chain is done, going through the characterisation of the different elements composing this detector.

Using a dedicated test bench SPOFS (Kuraray SCSF-78) of 1 mm and 0.5 mm were optically characterised, measuring basic properties, such as light yields and attenuation lengths, before measuring the crosstalk between juxtaposed optical fibres. Methods of analysis were designed to compare the signal from an isolated and ribbon SPOF.

Next, the MAPMT's key characteristics were studied using a UV-LED exciting SPOF, to guide the light to individual MAPMT cells, and a picoammeter as a readout system. Concerning the assembly of the MAPMT in a detector assembly, the ideal conditions to achieve a light tight setup were evaluated.

The full readout chain was completed by including a costumed DAQ board. Pulsed LEDs were firstly used to evaluate main limitations in signal response of the readout chain. Radioactive sources were then used to test the sensibility to particles (betas, gammas and alphas).

In terms of results, the crosstalk study needs further revision, specially quantifying its value. The MAPMT's performance was characterised and validated, whereas the DAQ board observed saturation and response to particles needs more understanding. However, the integration of the three elements of the microdosimeter was achieved and could be implemented into a first prototype.

Keywords: Proton therapy, Microdosimetry, Scintillating plastic optical fibres, Multi-anode photomultiplier, Data board

Resumo

Nos últimos anos, a prototerapia tem vindo a ganhar popularidade no tratamento do cancro pelo facto de distribuir dose pelos tecidos cancerígenos, não prejudicando substancialmente os tecidos saudáveis circundantes. Este efeito é possível devido à presença do pico de Bragg característico dos protões. Para tal é imprescindível desenvolver equipamentos de alta precisão que sejam capazes de medir em tempo real os valores de dose absorvida ao nível dos tecidos e DNA dos pacientes durante os tratamentos do cancro.

Este trabalho encontra-se inserido num projecto que pretende criar um novo detector capaz de medir em tempo real valores de dose com uma resolução sub-milimétrica. Este dispositivo vai ser construído utilizando fibras ópticas de plástico cintilantes (SPOFs) justapostas, cujo sinal vai ser lido por um fotomultiplicador multi-ânodo (MAPMT, 64 canais) e um sistema de aquisição de dados (DAQ) apropriado. Os materiais cintilantes, nomeadamente as fibras ópticas, absorvem energia da radiação ionizante e emitem vários fotões, com espectros de comprimento de onda característicos, sendo o seu número proporcional à energia depositada. Esses fotões cintilantes produzidos são transportados pelas fibras ópticas até chegarem ao fotomultiplicador, onde são absorvidos e transformados num sinal elétrico. De seguida, o sinal elétrico gerado é lido por um sistema de aquisição de dados. O trabalho incluido nesta dissertação consiste na caracterização total desta cadeia de deteção. Como tal, verifica-se a necessidade de estudar e validar os dados adquiridos utilizando para esse fim diversos instrumentos de leitura e fontes de excitação, como LEDs, nas várias etapas. Este processo de validação da cadeia termina com a introdução de fontes radioactivas para simular o comportamento esperado por partículas, que será assim o ponto inicial para simular os tratamentos de prototerapia, como é pretendido no futuro.

As medições decorreram no Laboratório de Instrumentação e Física Experimental de Partículas (LIP) e na Faculdade de Ciências da Universidade de Lisboa (FCUL). Os testes iniciaram-se com a leitura do sinal dos LEDs utilizando um mini espectrómetro, de forma a obter para além das curvas características de cada um deles, os respectivos comprimentos de onda de forma a comprovar que se encontram dentro dos espectros de absorção dos dois tipos de fibras ópticas utilizadas, as cintilantes SCSF-78 e deslocadoras de comprimento de onda Y-11. Sendo estas últimas utilizadas como referencia em um dos bancos de testes utilizado.

Para a caracterização do sinal proveniente das SPOFs de 1 e $0,5$ mm utilizou-se como sistema de leitura um banco de testes de fibras ópticas do LOMaC/LIP (Fibrómetro) e um LED como fonte de excitação. Primeiro, o sinal das SPOFs é lido estando estas isoladas umas das outras, através de varrimentos transversais e longitudinais, para medir as suas propriedades básicas, como o comprimento de atenuação e rendimento luminoso. Durante estas medições verificou-se que os comprimentos atenuação variavam entre 150 a 225 cm para fibras de 1 mm e 100 a 160 cm para as de 0,5 mm; a diferença do sinal das SPOFs com diâmetros diferentes ($31-53\%$), como também o sinal entre SPOFs novas e velhas ($44-57\%$). Estas últimas, visto existirem em grande quantidade, serão utilizadas nos primeiros protótipos durante as fases iniciais de otimização.

De seguida foram realizados testes para comparar o sinal proveniente de SPOFs isoladas e SPOFs colocadas justapostas umas às outras. Estes testes serviram para quantificar a diafonia óptica que pode ocorrer nas SPOFs. A diafonia óptica pode ser originada a partir de duas situações independentes: fotões cintilantes atravessando uma SPOF para outra ou a criação de novos fotões de cintilação. Durante estas medições, variou-se a posição da fonte de excitação

tal como o tamanho dos colimadores, os quais controlavam a quantidade de luz que entrava no sistema de leitura do Fibrómetro. Como um método auxiliar para análise dos resultados simulou-se numericamente o resultado utilizando distribuições normais. No caso de presença de diafonia óptica, esta pode ser descrita como o surgimento de uma nova fonte de luz próxima à fonte inicial, criando assim uma deformação do sinal proveniente das SPOFs juntas.

De seguida, os dados obtidos experimentalmente foram submetidos a dois métodos de análise desenvolvidos, utilizando folhas de cálculo e a linguagem de programação PYTHON. Os resultados obtidos foram posteriormente comparados com as simulações realizadas. Apesar de nenhum resultado conclusivo tenha sido obtido na localização e quantificação dos valores de diafonia óptica, estes testes forneceram uma etapa inicial para resolver este problema. Novos métodos de análise e uma melhoria da montagem experimental são fundamentais num trabalho futuro e para realizar medições com SPOFs de $0,25$ mm.

Quanto ao fotomultiplicador multi-ânodo, como não tinha sido utilizado antes, era importante inferir as suas características de forma a entender o seu funcionamento para integrar nesta cadeia de deteção. As características estudadas foram a estabilização temporal, a corrente escura, a diafonia eléctrica entre as células do fotocátodo quando apenas uma célula estava iluminada por uma SPOF, a relação entre a corrente lida do MAPMT e a alta tensão fornecida, e, por fim, a sua linearidade usando filtros de densidade que regulavam a transmissão de luz. A sua validação foi realizada utilizando como sistema de leitura um picoamperímetro e uma montagem experimental adequada, a qual englobava uma fonte de alta tensão para alimentar o MAPMT, uma fonte de baixa tensão para o LED e uma caixa preta. Esta caixa preta continha o MAPMT, as SPOFs e o LED, prevenindo assim o contacto da luz exterior com o MAPMT e evitado reflexões secundárias no seu interior que prejudicam as medições. Verificou-se que para uma alta tensão de - 900 V, existe um valor de corrente escura de - 0,143 nA; entre as células do fotocátodo existe uma diafonia elétrica igual ou inferior a 3%; a dependência da corrente do MAPMT em relação à alta tensão segue uma função potência e a linearidade das curvas para diferentes valores de alta tensão e diferentes células apresentam 1% de erro.

Tendo este trabalho decorrido em paralelo com o desenvolvimento do desenho inicial, uma questão tornou-se pertinente no caso em que o fotodetector não esta encapsulado no volume do detector (i.e. contactos eléctricos na face do detector onde se acopla a eletrónica de aquisição) e afastado de qualquer luz externa. A questão colocada foi se a presença de luzes externas, as quais não estejam apontando directamente para as células do fotocátodo, interfeririam na resposta do MAPMT. Nestas medições verificou-se que se as células do fotocátodo estiverem devidamente isoladas, o sinal lido será semelhante a se o LED estivesse desligado.

A placa de aquisição de dados foi desenvolvida, tendo como principal intuito a medição de posições e taxas dos muões cósmicos. Neste trabalho, é necessário validar a funcionalidade da placa para medir o valor da energia depositada nas fibras ópticas, a qual não foi testada anteriormente. Testes iniciais foram efectuados com um LED, este sendo pulsado recorrendo a um gerador de sinais. Nestes testes, visto que tinha ja decorrido uma validação anterior da mesma placa de aquisição numa tese de mestrado, por questões práticas apenas se ligaram dois canais entre o MAPMT e a placa de aquisição. Começou-se por medir os limiares de resposta dos dois canais, seguindo-se a resposta em frequência, verificando-se a gama dinâmica de resposta da montagem.

Depois foram realizados testes utilizando várias fontes radioactivas existentes em laboratório e usualmente utilizadas como referências experimentais, nomeadamente césio 137, cobalto 60,

tálio 204 e amerício 241. Todas as fontes foram comparadas com medidas de fundo, ou seja, sem qualquer fonte. Nesta fase, constatou-se que existe visivelmente uma distinção entre a resposta com a presença de fonte e sem fonte, como era esperado. Para a fonte de césio realizaram-se testes variando os valores da fonte de alimentação de alta tensão do MAPMT e verificou-se que, como esperado, a taxa de eventos aumenta com o aumento da alta tensão. Os dados obtidos com as fontes radioactivas foram comparados com simulações realizadas num trabalho paralelo das respostas das fibras ópticas para as respectivas fontes. Contudo, a comparação destes dados não é intuitiva. Por isso, em trabalho futuro será necessário estudar melhor esta resposta, quer partindo duma análise de outros parâmetros do funcionamento da placa quer de uma otimização da montagem experimental.

Com este trabalho foi possível estudar os três elementos da cadeia de detecção para a construção do microdosímetro. Tendo-se avaliado cada um dos elementos de forma independente pode-se concluir que a presente montagem poderá ser utilizada para um primeiro prototipo do microdosimetro. Contudo, é necessário desenvolver e estudar novas abordagens para os problemas aqui explicitados, desde alterações às montagens experimentais como à criação de novos métodos de análise de dados com maior precisão e clareza na interpretação dos dados.

Palavras-chave: Terapia com protões, Microdosimetria, Fibras ópticas cintilantes de plástico, Fotomultiplicador multi-ânodo, Placa de aquisição de dados

Contents

List of Tables

List of Figures

List of Abbreviations

AD Analog-Digital

CT Computed Tomography

CTN Campus Tecnológico e Nuclear.

D Dose.

DAQ Data Acquisition.

DIS Direct-ion Storage

EM Electromagnetic.

EPD Electronic Personal Dosimeter

ESTAR Stopping Powers and Ranges for Electrons

FCUL Faculty of Science of University of Lisbon

FNTD Fluorescent Nuclear Track Detectors

FP Fluorinated Polymer

FPGA Field-programmable gate array.

HV High Voltage

ICNAS Instítuto de Ciências Nucleares Aplicadas à Saúde.

IPO Instituto Português de Oncologia de Lisboa Francisco Gentil

LED Light-emitting Diode

LET Linear Energy Transfer.

LIP Laboratório de Instrumentação e Física Experimental de Partículas

LS Longitudinal Scan

LV Low Voltage

MAPMT Multi-anode photomultiplier

NIST National Institute of Standards and Technology

OD Optical Density

PLC Power Line Cycles

PMMA Polymethyl Methacrylate

PMT Photomultiplier tubes.

PS Polystyrene

PT Proton Therapy.

RBE Relative Biological Effectiveness.

ROI Region of Interest

RPC Resistive Plate Chamber.

RS Radiation Source

SOBP Spread-Out Bragg Peak

SPOF Scintillating Plastic Optical Fibre

TEPC Tissue-Equivalent Proportional Counter

TLD Thermo Luminescent Dosimeter

WCD Water Cherenkov Detector.

Chapter 1

Introduction

1.1 Motivation

As reported by the World Health Organisation [1], cancer is the second leading cause of death worldwide. In 2018, cancer was responsible for 9.6 million in mortality, representing 1 in 6 deaths. A large number of cancer patients receive radiation therapy during their treatment, as a sole treatment or in combination with surgery or chemotherapy [2].

Radiation therapy damages cells by destroying the genetic material, which is how cells control growth and division. This type of therapy damages both healthy and cancerous cells. However, the goal is to reach a compromise between destroying as few healthy cells as possible while killing the most cancerous cells.

The current radiotherapy treatments available in Portugal are external beam radiotherapy and brachytherapy, both photon therapy methods. However, there is an ongoing discussion to build a hadrontherapy centre at *Campus Tecnológico e Nuclear* (CTN) for proton therapy (PT) treatments.

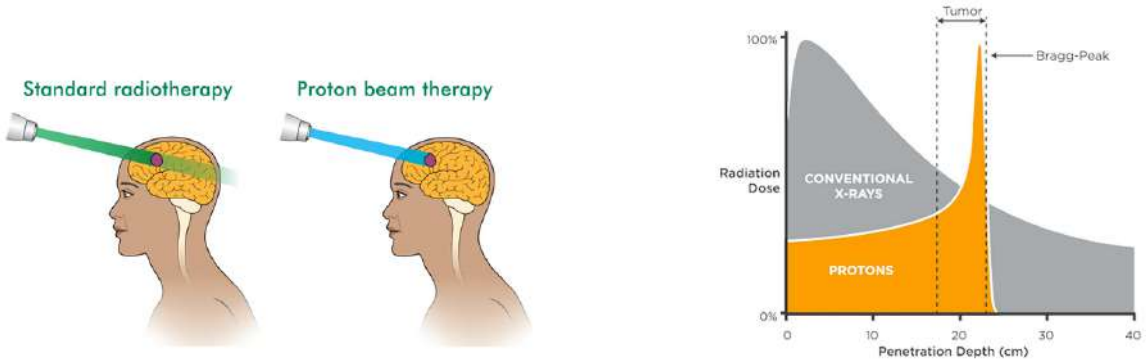

(a) (b)

Figure 1.1: (a) Difference between standard beam radiation and proton beam radiation [3]. (b) Depth profile for conventional X-rays (gray) and protons (orange) [4].

In radiotherapy, one of the most fundamental concepts is deciding how much energy has to be deposited in a targeted volume to eliminate cancerous cells. Although both photons and protons [2, 5] are able to provide a uniform amount of energy, photons have the downside of affecting the healthy tissues around the target volume as seen in figures 1.1. Protons have a well-defined range of penetration (Bragg Peak), which will be further explained on chapter 2.

In every treatment plan, one of the most fundamental parameters is the effectiveness of protons regarding their potential to induce biological effects in tissues because it determines the tumour dose prescription and organ at risk dose constraints. Current treatment plans show that for the same physical dose, the biological effect of protons on the tumour volume is 10% greater than the biologic effect in conventional photon radiotherapy.

Proton therapy is mainly used for eye-related cancers and cancer in children, on the brain or the spinal cord since it lessens the chance of harming healthy and growing tissue. Additionally these procedures treat several other cancers in other parts of the body such as lung, breast, liver, pancreas, prostate and benign tumours.

The field that studies the amount of ionising radiation deposited in tissue and its effects is called radiation dosimetry [6], or simply dosimetry. The parameters that influence the study of dosimetry are the following:

- The damage caused by the radiation type;
- The administered dose;
- The dose rate.

Thus, the quantities obtained from dosimetry calculations are fundamental to estimating radiation protection, risk assessment, diagnostic dose estimates, and treatment planning.

When preparing a radiotherapy session, the focus will be on a determined organ of the human body. However, the effects of the radiation will be at a cellular level. Since most human cells have a diameter, $d = [2, 120]$ μm [7, 8], the desired scale of study is the micro. The measurement of the spatial, temporal and energy distributions of energy imparted in cellular and sub-cellular biological structures and the relationship of such distributions to biologic effects is called microdosimetry. Figure 1.2 shows the dose-dependence at different tissues scales/levels.

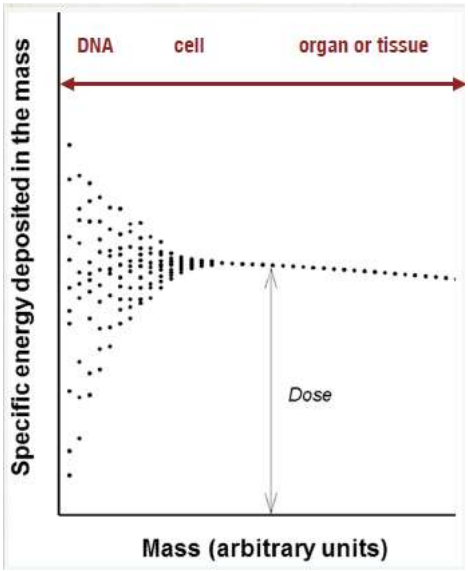

Figure 1.2: Specific energy (dE/dm) deposited by radiation in matter as a function of mass with the macroscopic dose being constant [9].

At a tissue or organ level, the specified energy deposited by the mass unit tends to a mean value. However, as the scale downsizes, this value's variance rises. To study the radiation effects at cell level there is a need for high precision instruments, namely microdosimeters.

1.2 Dosimeters and Microdosimeters

A dosimeter [10] can be defined as any device that is capable of providing a reading, r, measuring the absorbed dose, D, deposited in a sensitive volume, V, by ionising radiation. There are two main categories of dosimeters [11]:

- **Passive Dosimeters**: produces a radiation-induced signal, then stores it in the device for later processing and analysis of the output;
- **Active Dosimeters**: measures a radiation-induced signal and displays a direct reading of the detected dose or dose rate in real-time.

Table 1.1: Different types of dosimeters.

Types of dosimeters	Examples of dosimeters	Dose measure
Passive Dosimeters	**Thermo Luminescent Dosimeter (TLD)** [12]**:** consists of a thermoluminescent material, normally calcium sulphate doped with dysprosium ($CaSO_4$: Dy) or lithium fluoride (LiF) which measures ionising radiation exposure by the light output produced by the electrons relaxation. Example in figure 1.3(a).	0.01-10000 mGy
	Film Badge Dosimeters [11]**:** monitors cumulative radiation dose due to ionizing radiation, a similar process as X-ray pictures. Example in figure 1.3(b).	10 Gy
	Fluorescent Nuclear Track Detectors (FNTD) [13]**:** based on an aluminium oxide crystals doped with carbon and magnesium impurities ($Al_2O_3 : C, Mg$) and confocal laser scanning fluorescence microscopy technique for dose measurements. Monitoring 3D track structure of particles.	0.2-30 mGy
	CR-39 [14, 15]**:** type of polymeric nuclear track detector, mostly used for neutron dosimetry due to their insensitivity to low linear energy transfer radiations and convenient to expose, process and analyse.	5.12 Gy
	Direct-ion Storage (DIS) Dosimeter [16] **:** a combination of an ion chamber and a non-volatile electronic charge storage element, in which incident radiation causes ionisation in the chamber wall and gas, and then the charge is stored for subsequent readout.	1 μGy-1 Gy
Active Dosimeters	**Electronic Personal Dosimeter (EPD)** [11]**:** measures a continuous readout of cumulative dose and current dose rate in real-time. Their main use is as a safety warning for the user when it is reached a specified dose rate or a cumulative. The device is powered by batteries either small Geiger-Mueller tube or a semiconductor. Example in figure 1.3(c).	1 μGy-10 Gy
	MOSFET Dosimeter [11]**:** monitors and direct reading of radiation dose rate.	0.16–2.70 mGy/s
	Self-reading Dosimeter [17]**:** like EPD, they are devices worn on the body to measure accumulated dose. However, they do not need batteries.	50-200 mGy

In the table 1.1 as well as in the following figures 1.3, there are some examples of dosimeters available commercially. Each of them is specialized for different applications in physics.

(a) (b) (c)

Figure 1.3: Examples of dosimeters: (a) TLD [18], (b) Film Badge Dosimeter [19] and (c) EPD [20].

Ideally, to measure dose at cellular and sub-cellular levels, there are requirements to be met when developing a dosimeter:

- Tissue-equivalence: the detector's walls and sensitive volume must have a composition similar to tissues;
- Radiation resistant, meaning they be must be resistant to damage or malfunctions because of high ionizing energy;
- Spatial resolution at the microscale to better determine the region in space in which energy deposition from the ionizing particle can affect the operation of a device;
- Low threshold, which means having output signal at lower values;
- Low power operation, compact and low cost.

Bellow are three examples of the most common types of microdosimeters in the current market.

Ionisation Chambers

Ionisation chambers [21, 22] are simple gas-filled detectors, measuring exposure by detecting freed electron charges created by x-ray and gamma photons ionising the gas. These chambers need a high positive voltage applied at the collecting anode. It is mainly used in determining the intensity of a radiation beam or for counting individual charged particles, being perfect instruments for calibration tests. In fact, they are widely used as reference during the development of dose measuring instruments.

Tissue-equivalent Proportional Counters (TEPCs)

Tissue-equivalent proportional counter (TEPC) is a microdosimeter described as a walled ionisation chamber operated at high voltage. In the figure 1.4, an example of TEPC is shown, in this case, the "Hawk" TEPC from NASA. TEPC measures the dose in complex fields, which are

composed of several particles, and are the most common type of detector used in microdosimetry as they can measure event by event basis. Moreover, the energy deposited by particles in the gas is equal to the energy deposited in a cell because the pressure is adjusted to equal the energy loss at the cell scale. Since they operate at low pressure, this allows the tissue equivalence, meaning that the energy deposited on a small site of tissue density can be mimicked. As a result, if the gas and wall material have the same atomic composition, the fluence (J/cm^2) of secondary charged particles should be independent of density variations, excluding the influence of the density effect on the stopping power.

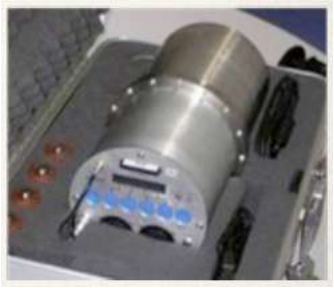

Figure 1.4: "Hawk" TEPC from NASA [23].

However, for proton beams, the energy deposited in a single event can be overestimated due to the detector wall effects, causing distortions in their reading. Another problem is their size since this detector is too large to model arrays of cells. Therefore, it is difficult to achieve a resolution at a micro-scale, and more vulnerable to any pile-up effects in radiotherapy level dose rates because of simultaneous multiple events. In experimental setups, TEPC is difficult to operate due to requiring a high voltage bias (> 900 V), gas supply requirements and low irradiation fluence rates conditions [2, 24].

Si-based Microdosimeters

Si-based microdosimeters [24] are useful for the prediction of single-event upsets in microelectronics, as they measure ionisation via electron-hole pair creation in a depletion layer [2]. As an advantage, because these detectors have a higher density than ionisation chambers, they are 18000 times more sensitive and, as the energy needed for ionisation is ten times smaller than ionisation chamber, they do not have any gas supply requirement and are resistant to radiation. Due to their closeness in size to the region of interest, Si-based microdosimeters have a spatial resolution with an order of 10 μm and a reduction of the wall-effects present in TEPCs. Nonetheless, they also have their limitations, such as recombination effects that can limit their charge collection efficiency, limited signal-to-noise ratio due to the lack of intrinsic amplification and energy-dependent conversion to tissue-equivalent doses.

1.3 A microdosimeter Using Scintillating Plastic Optical Fibres

In the last decades, there have been many discussions on building scintillating dosimeters for radiology or other radiotherapy applications, due to their particular characteristics such as real-time detection, water-equivalency, energy independence and a high spatial resolution [25, 26].

The work plan of my master thesis is included in the development of a new detector for proton therapy radiobiology studies, capable of measuring real-time doses with sub-millimetre

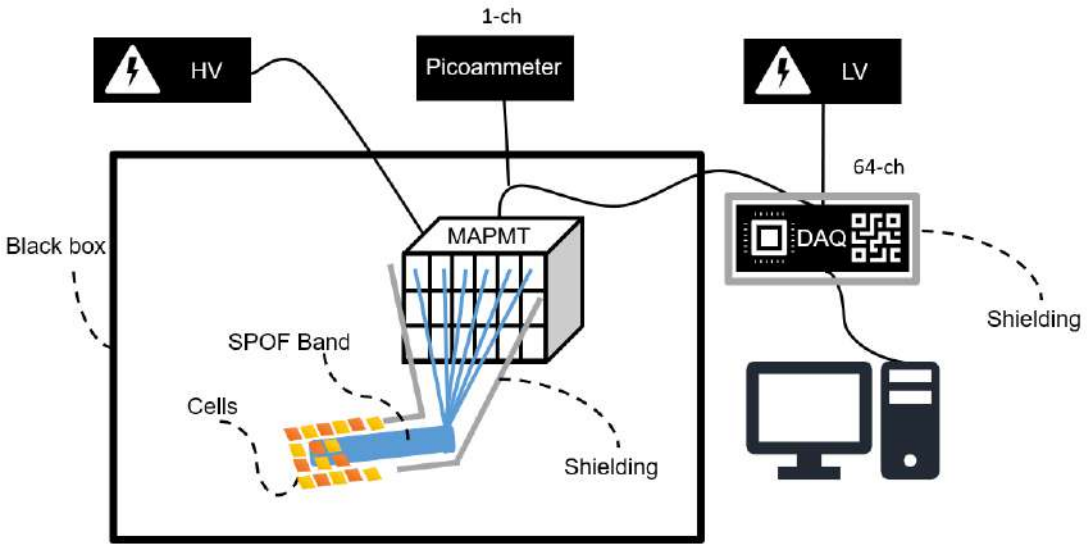

Figure 1.5: Concept of the microdosimeter prototype.

$(1 - 0.250\ \mu\text{m})$ resolution. The intended detector will be constructed using juxtaposed thin scintillating plastic optical fibres (SPOFs) coupled with a readout by a multi-anode photomultiplier (MAPMT, 64 channels), as seen in figure 1.5. This master thesis will present a study and characterisation of the full detection chain, including the validation of the MAPMT readout using a data acquisition board (DAQ) as well as the full tests concerning the characterisation of the scintillated optical fibres for the measurement and validation of the deposited energy from ionising radiation.

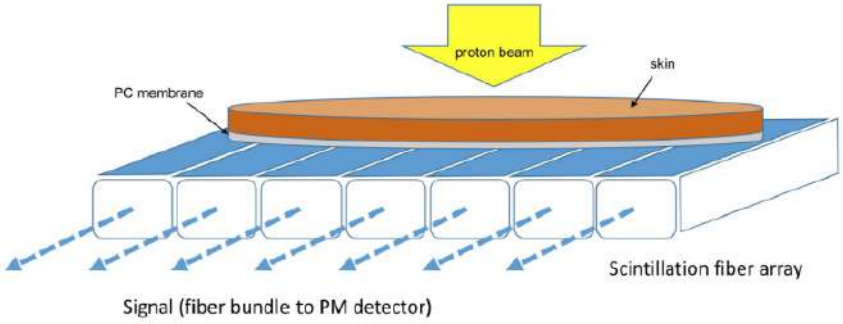

Figure 1.6: Visual representation of the set-up arrangement of the scintillating fibres array sensor with the skin tissue placed onto the surface, to be irradiated by the proton beam. The signal is collected by the fibres and guided to a bundle towards the detector.

In a later stage, a team of biochemists from BioIsi[1] and ITQB-NOVA[2] will take part in the growth and characterisation of the biological system to be irradiated, which means growing the cells and tissues on the detector itself, as seen in figure 1.6. Since skin is a dose-limiting organ for any radiotherapy session when considering the type of beam delivery and the risk of exposure is higher, this is a highly relevant study for the response of the skin to PT as well as other tissues. The plan is to grow a 3D skin model onto scaffolds (supporting structure) and place them over

[1]BioSystems and Integrative Sciences Institute from University of Lisbon - Faculty of Science.
[2]Instituto de Tecnologia Química e Biológica António Xavier from University NOVA of Lisbon.

the detector.

This proposed plan opens the possibility of new radiobiology studies in the transition from the cellular level to tissues and therefore, shed new light on the relative biological effect values from cell lines to living tissues and organs.

The aim of this project is primarily for the laboratory environment, keeping in mind a possible adaptation into a commercial product in future work.

1.3.1 Why Using Scintillating Plastic Fibres?

Scintillating fibre-optic dosimeters offer a number of advantages, such as [27, 28]:

- Spatial resolution, providing the spatial resolutions desired and the possibility to achieve spatial resolutions equal to the optical fibre's diameter (0.25, 0.5 and 1.0 mm)[3];
- Considerable flexibility, able to adapt to various geometries;
- Tissue or water equivalence, because they are made of hydrocarbon molecules with similar scattering properties as living tissues;
- Remote and real-time sensing;
- Immunity to electromagnetic interference (EMI), due to being made of an insulating material and able to transport signal containing the dose information do reasonable long distances ($100 - 200$ cm);
- Radiation hardness.

Although the diameter of the optical fibres is large while compared with the average cells size it should be noted that several types of cells still fill in the range of the available fibre dimensions. It should be also added that including several planes of optical fibres allows an increase of the spatial resolution of the detector as demonstrated in ATLAS fibre tracker [29] and more recently in LHCb tracker [30].

In chapter 2, the theoretical foundation needed to be taken into consideration for this work will be discussed, from defining dosimetry parameters, such as dose, LET and RBE, to the scintillation process. In chapter 3, all the materials and procedures are described, followed by the obtained results in chapter 4. In the end, conclusions and future work.

[3]However the manufacturer Kuraray Co. has shown the availability of producing fibres with a smaller diameter on demand.

Chapter 2

Dosimetry Physics

2.1 Introduction

When a body is submitted to an irradiation process, there is a certain amount of energy that will be deposited on the various body tissues. This deposited energy, when quantified by a mass unit is called dose (J/kg). The dose is directly related to the biological effects arising from irradiation and it is important to be studied and understood.

2.1.1 Dose

Dose, D, or absorbed dose, is defined as the expectation value of the energy imparted to matter per unit mass at a point [10] and can be illustrated in figure 2.1.

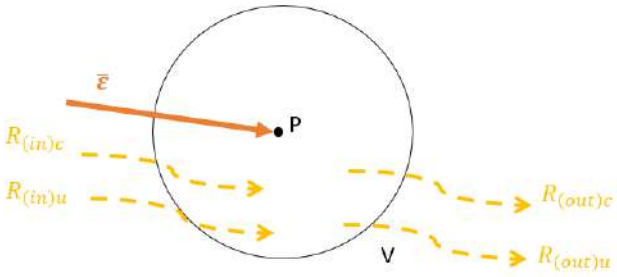

Figure 2.1: Visual representation of the absorbed dose at a point P in a volume V.

The equation that defines energy imparted by ionising radiation to matter of mass m in a finite volume V is:

$$\bar{\epsilon} = (R_{in})_u - (R_{out})_u + (R_{in})_c - (R_{out})_c + \Sigma Mc^2 \tag{2.1}$$

in which $(R_{in})_u$ is the radiant energy of uncharged particles entering V, $(R_{out})_u$ is the radiant energy of all the uncharged radiation leaving V, $(R_{in})_c$ is radiant energy of the charged particles entering V, $(R_{out})_c$ is the radiant energy of the charged particles leaving V, and ΣMc^2 is the net energy derived from the rest mass in V.

The dose D is defined at any point P in a volume V as:

$$D = \frac{d\bar{\epsilon}}{dm} \tag{2.2}$$

2.1.2 Linear Energy Transfer

Linear Energy Transfer (LET), also known as the restricted linear collision stopping power, is a common metric for radiation quality [10]. It determines the ratio of the average collisional energy loss, dE, traversing a distance, dl, for energy transfers below a cutoff value Δ [27], as seen in equation 2.3:

$$L_\Delta = \left(\frac{dE}{dl}\right)_\Delta \tag{2.3}$$

LET varies with the species and energy of the particle. Since radiation beams have a spectrum of LET values at any given spatial location, it is necessary to use an average value of the LET at the region of interest. LET is obtained via Monte Carlo calculations.

2.1.3 Relative Biological Effectiveness

For an equal physical dose, the various radiation types will not cause an equivalent amount of biological damage nor will all tissues react analogously to a given physical dose. To account for the differences in biological damage it resorts to a scaling factor known as the relative biological effectiveness (RBE). The RBE is the ratio of the radiation dose called standard radiation and a dose that produces the same biological effect [31], as depicted in figure 2.2.

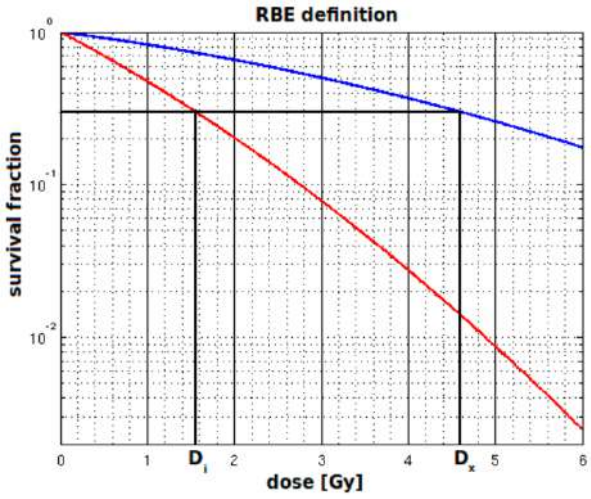

Figure 2.2: Cell culture irradiated by photons (blue curve) and by carbon ions (red curve) [31].

The standard radiation typically is 250 keV X-ray beam photons or a source of cobalt-60 gamma rays:

$$RBE = \frac{D_\gamma}{D_{particle}} \tag{2.4}$$

where D_γ is a reference absorbed dose of radiation of a standard type as defined above, and $D_{particle}$ is the absorbed dose of radiation of type particle that causes the same amount of biological damage. Both doses are quantified by the amount of energy absorbed in the cells.

Both doses are quantified by the amount of energy absorbed in the cells. The biological effect of protons depends strongly on the track-structure of the particles in tissues. The clustering of energy deposition determines the degree of cell damage and the ability of cells to repair.

Thus, what is important for radiobiology experiment studies is the measurement of doses and estimation of LET values with high spatial resolution at the micro-scale.

2.2 Interaction of Radiation with Matter

2.2.1 Proton Interactions

There are several mechanisms in which protons interact with matter [2, 32]: Coulombic interactions with atomic electrons (ionisation), Coulombic interactions with the atomic nucleus (scattering), nuclear reactions, and Bremsstrahlung.

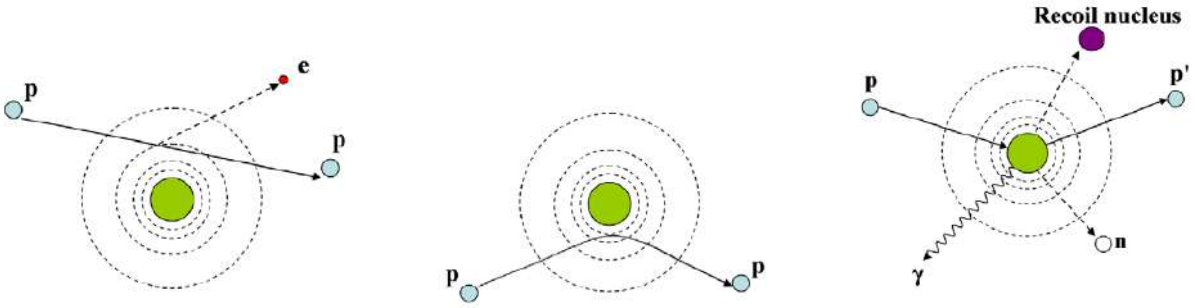

(a) (b) (c)

Figure 2.3: Schematic illustration of proton interaction mechanisms: (a) energy loss via inelastic Coulombic interactions, (b) deflection of proton trajectory by repulsive Coulomb elastic scattering with nucleus, (c) removal of primary proton and creation of secondary particles via non-elastic nuclear interaction (p: proton, e: electron, n: neutron, γ: gamma rays) [32].

Ionisation

Ionisation, as seen in figure 2.3(a) is the process that represents the continuous energy loss that the proton suffers via frequent inelastic Coulombic interactions with atomic electrons. Due to the larger mass of the proton compared to the mass of the electron, the proton's trajectory is linear.

Scattering

Scattering, or Multiple Coulomb Scattering, as seen in figure 2.3(b), represents the deflection of a proton by a single atomic nucleus. When a proton passes close to the atomic nucleus, it experiences a repulsive elastic Coulombic interaction that appears due to its dependence on the atomic number (Z) or the number of protons in the nucleus. Even though the proton loses a negligible amount of energy, a small change in its trajectory can be of the upmost importance, especially in the dose distribution in the surrounding tissues.

Nuclear Interactions

In a nuclear reaction, as seen in figure 2.3(c), the proton enters the nucleus and the result may be the emission of a proton, or heavier ion or one or more neutrons. Although non-elastic nuclear reactions between protons and the atomic nucleus are less frequent, they directly affect

the therapeutic region of a proton field because of the removal of primary protons. On the contrary, elastic collisions are considered negligible since the trajectory deviation from primary to secondary particles is minimal.

Bremsstrahlung

Bremsstrahlung [33] is the German word for *"braking radiation"* and describes the production of electromagnetic radiation by the immediate slowdown or deflection of particles as they pass near-atomic nucleus. However, for the proton beam energies used at a clinical level (up to 250 MeV), the proton Bremsstrahlung can be ignored, due to their small cross-section, making the probability of it occurring much lower than the other three mechanisms previously mentioned [34].

2.2.2 Protons Path Through Matter and Bragg Peak

As seen in figure 2.4 protons moving through matter slow down as they lose energy in atomic or nuclear interaction. With the reduction of the proton's energy, there will be an increase in interaction with orbiting electrons. The number of interactions will continuously rise until they reach a maximum at the end of the range, which causes a maximum energy release within a targeted area [35] called Bragg Peak. This is explained by the rapidly rising number of ionisation events. The Bragg Peak's depth can be described as a function of the beam energy while its width will be connected to the beam spread and energy straggling.

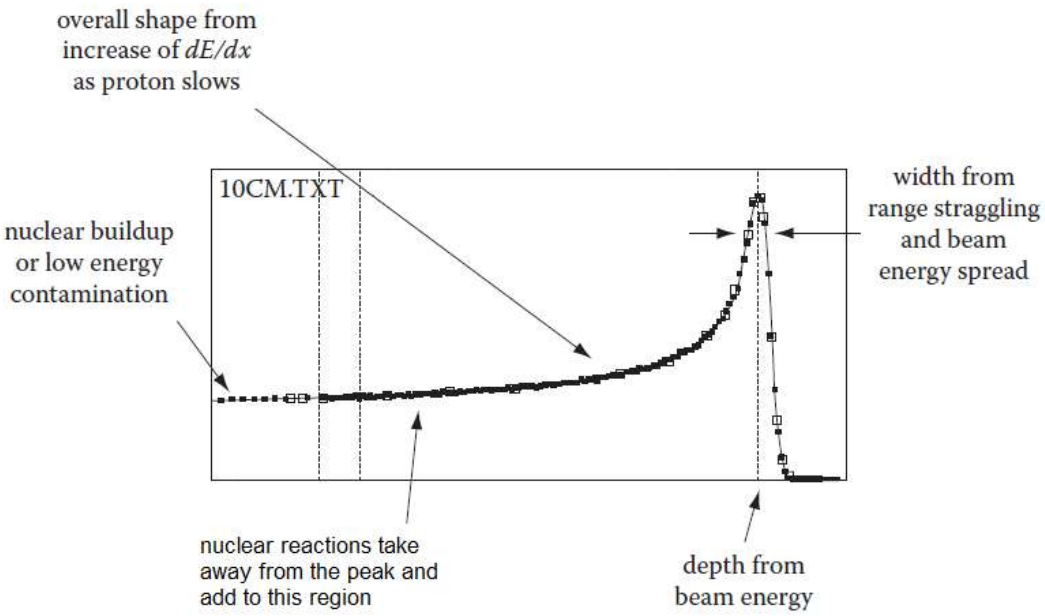

Figure 2.4: Ingredients for a Bragg Peak [2].

The Bragg Peak is such a crucial part of proton therapy because of its characteristic abrupt curve, as seen in figure 2.4. After the proton beam's peak, the dose transferred at that point can be considered negligible due to the drop of the ionisation events. Therefore, the healthy tissue behind the tumour area is not majorly affected by the proton beam [2]. However, this statement is not entirely correct because of the presence of nuclear interactions. Each nonelastic reaction

removes a proton from the electromagnetic (EM) peak and, the secondary proton emitted will deposit their energy further upstream (range straggling). The latter process will be of most relevance for the deposited dose on the healthy tissue surrounding the target, as depicted in figure 2.5.

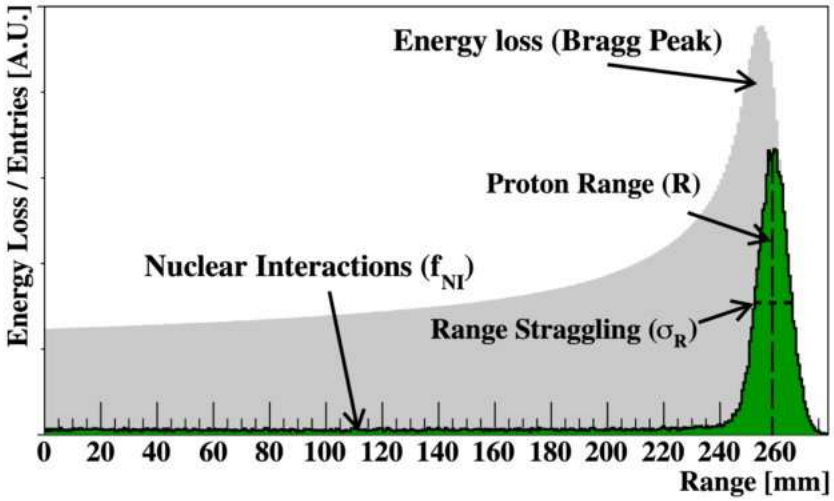

Figure 2.5: The relationship between the proton beam's energy loss (light gray), and the protons' final stopping position R (green). The light gray represents the ionisation process while the green represents the nuclear interactions contribution. Shown is also the range straggling σ_R and protons undergoing nuclear interactions. MC simulation results from a 200 MeV beam in water, MC simulated using GATE [36].

2.2.3 Energy Straggling

In many clinical calculations, it is valid to assume that the energy loss rate results from a steady slowing down of particles, which in turn neglects any variations in the energy loss of individual rates. As a result, the energy loss rate is calculated through its mean value only.

However, the energy loss due to ionisation events is a statistical phenomenon [32, 37] where the range of a proton beam carries a certain amount of uncertainty that can be expressed similarly but from two different points of view. If the protons with the same starting and ending position, meaning the same path length, have different ending energies, then the accumulation of several variations in energy loss is commonly known as energy straggling. If protons with the same starting and ending energies have different path lengths, then the accumulation of the different variations in-depth value is usually known as range straggling. Both of these explanations are analogous to each other.

Energy or range straggling is one of the physical processes that strongly affects the shape of a proton Bragg curve, causing a broadening of the peak area. Hence it is the key to understanding the characteristics of proton dose distributions.

As treatment plannings keep on evolving, there is a high demand for an even bigger accuracy in every parameter of the planning. The energy straggling [37] is greatly affected by three issues where the proton range is concerned:

- Tissue interfaces, due to the different densities of the organs;
- Organ motion, which means the tumour will likely move as well;

- Ongoing treatment, where the reduction of the tumour needs to be taken into account.

Energy straggling can also affect the resolution of the diagnostic therapies, such as computed tomography (CT) scans, which are needed for better preparation of the patient's treatment planning

2.3 Proton Therapy

The equipment needed to perform a treatment for PT is illustrated in figure 2.6. The first step is to extract protons from hydrogen atoms, proceeding to the acceleration of the particles to two-thirds of the speed of light using a superconducting cyclotron. Although a synchrotron can also be a choice, it has some disadvantages compared to a cyclotron, such as varying electric and magnetic fields and large dimensions. In addition, linear accelerators are too expensive and require large infrastructures like synchrotrons [38, 39].

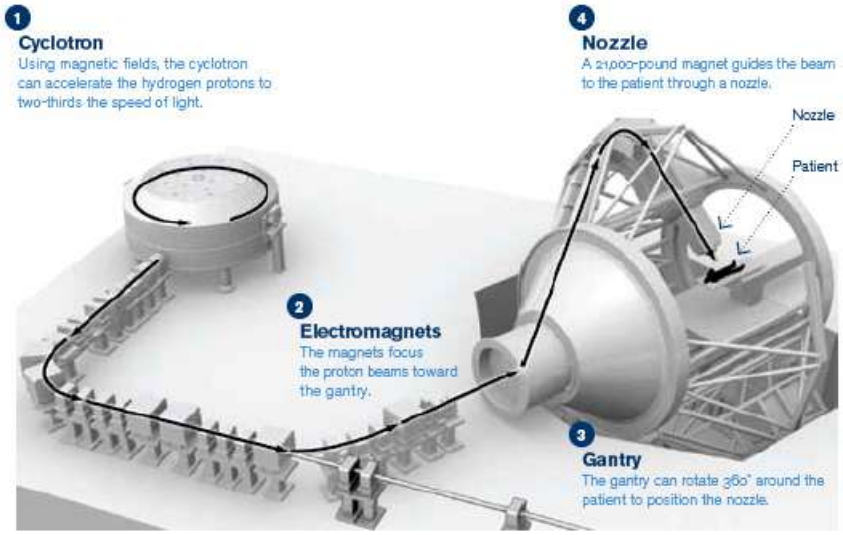

Figure 2.6: Diagram of the equipment needed for proton therapy [40].

The next step is the beam transport system, using electromagnets to focus and shape the proton beam towards the treatment room. The main goal of this process is to obtain the small beam sizes necessary for clinical uses. The gantry is the equipment used to administer the protons to the patient. With a large, sphere-shaped structure, the gantry rotates 180° to each side, covering a total area of 360°, therefore allowing treatments at any angle and minimising the need to reposition the patient during the treatment. In the end, a nozzle, a recently introduced feature, is attached to the gantry to have higher precision dose delivery.

2.3.1 Proton Relative Biological Effectiveness

In most proton treatments, a single proton beam is not enough to cover the total size of a tumour. For this reason, a combination of different energy proton beams are used, thus having different depths values, the sum of which creates a curve called Spread Out Bragg Peak (SOBP), in figure 2.7. Additionally, these proton beams have associated to them an appropriate weighting to produce a flat plateau SOBP, which should deliver an even dose-value to the entirety of the targeted tumour.

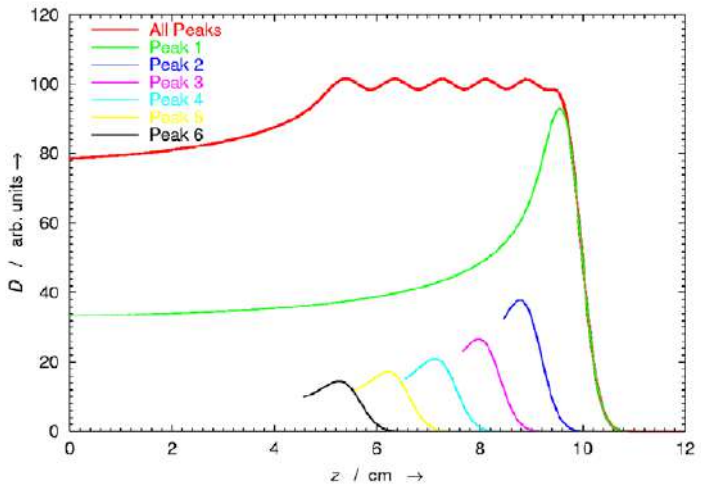

Figure 2.7: Absorbed dose D as a function of depth z in water from a SOBP (red curve) and its solo Bragg peaks [32].

One of the biggest influences on the SOBP's behaviour is the proton relative biological effectiveness (RBE). To solve this problem, as a pragmatic clinical standard the RBE value is fixed at 1.1 for the proton dosimetric calculations. This value comes from the mean obtained in *in vivo* studies for body cells deriving out of figure 2.8.

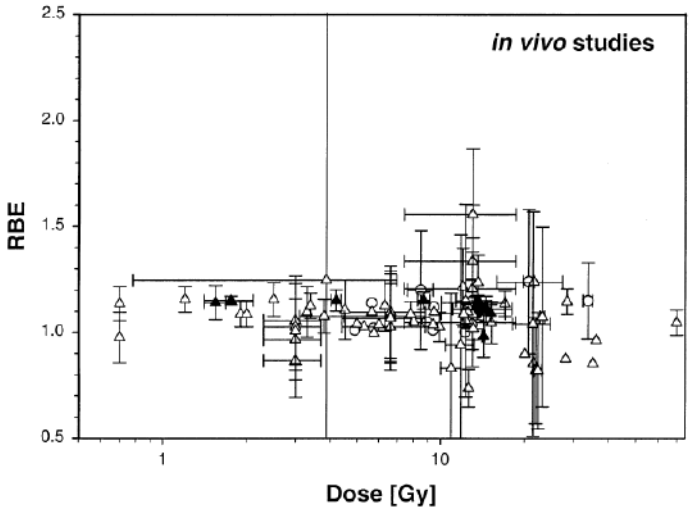

Figure 2.8: Experimental proton RBE values as a function of dose/fraction measured *in vivo* in the center of a SOBP [41]. Closed symbols show RBE values for jejunal crypt cells, open symbols stand for RBEs for all other tissues.

However, this value does not represent correctly the behaviour of RBE [42], especially at end-of-range elevations, as seen inside the red circle in figure 2.9. One of the explanations for this phenomenon is how much the energy deposited varies at different path lengths (LET parameter) due to different densities present in the human body, from different organs and bones. This represents one of the challenges that radiobiologists are faced with nowadays that require an answer in order to improve this type of therapy.

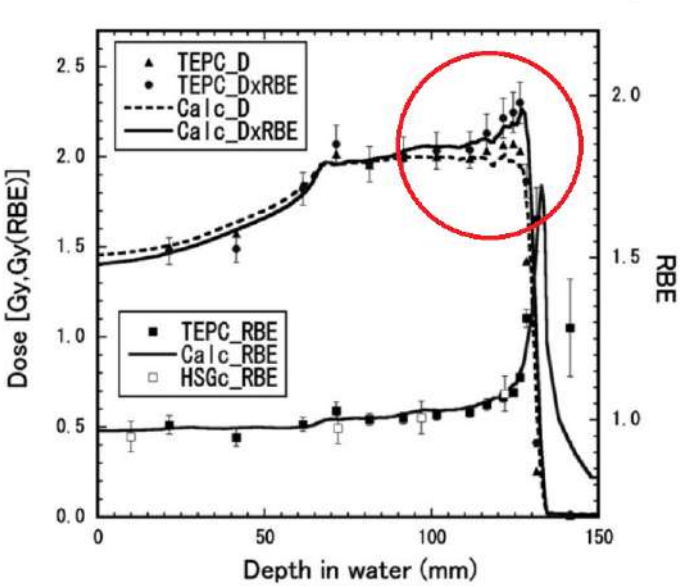

Figure 2.9: Dose dependence of the depth in water of a 155 MeV proton beam with the 6 cm nominal SOBP width [43].

2.3.2 Various Types of Proton Therapy

The first and oldest method of PT used was the passive scattering beam delivery [44], where the proton beam is spread out by scattering devices, and then shaped by placing items such as collimators and compensators into the path of the protons, as seen in figure 2.10. Since this method provides a homogeneous dose to the target, it deteriorates the control over the dose distribution closer to the target, also visible in figure 2.10, exposing healthy tissues around the tumour to radiation. These types of machines, although still in operation, are no longer being produced.

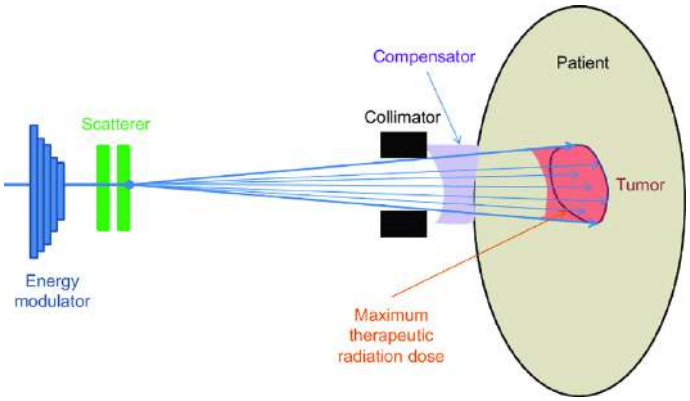

Figure 2.10: Schematic of the Passive Scattering Beam Delivery method [45].

The new method of PT is the pencil beam scanning [44], where the dose is delivered by sweeping a proton beam laterally over the target, thus delivering the required dose while closely conforming to the shape of the targeted tumour, as seen in figure 2.11. This conformal delivery is achieved through magnetic scanning of thin small beams of protons instead of apertures and compensators. This allows greater flexibility and control over the dose distribution.

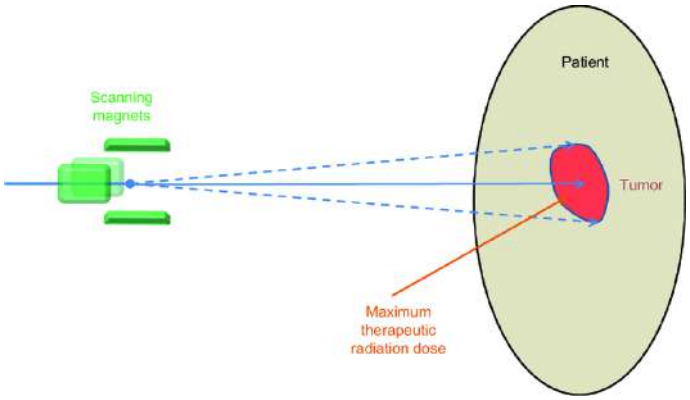

Figure 2.11: Schematic of the Pencil Beam Scanning method [45].

2.3.3 Why the Study for Skin?

Skin [46]] is the biggest organ of the human body, serving as a protective barrier between the organism and the environment. Obviously, it is a parameter to be taken into consideration when preparing for a session of proton therapy. First and foremost, the skin [47] is always the entrance organ and its exposure to the radiation must be as low as possible in order to avoid damage, especially considering that the Bragg Peak has an initial build-up region.

Another problem arises due to the pencil beam scanning method since in recent studies [48, 49, 50] it has been noticed that damage to the skin has risen significantly in comparison to the passive scattering beam delivery. Thus, there is a growing demand for a better understanding of the impact of PT on the skin. However, the body has many different and diverse cells. Even though the skin is a major factor to be considered, it is still unsure how accurate a skin model can be used to explain the behaviour of other body cells more interesting for radiobiology studies.

2.3.4 Limitations to PT

There have been several discussions regarding whether the proton beam therapy has reached its dosimetric limitation due to its lateral penumbra, also known as spot size, range uncertainties and deliver efficiency [51]. Another downside of radiotherapy, in general, is that some organs should not be exposed to the proton beam, therefore careful attention while planning the treatment is called for. Inevitably, more studies are needed in this area in order to optimise and develop this field of study.

Furthermore, there are other options in the study, such as carbon ions [52]. Like protons, the carbon ions also have a Bragg Peak, but they have a thinner shape, where distal tissues receive little energy. However, this Bragg Peak reaches greater depths. Moreover, carbon ions have a higher LET, thus having higher RBE values than protons.

2.4 Dosimetry with Scintillators

It is important to comprehend the bridge between dosimetry and the scintillation process when we aim to use scintillating optical fibres as sensors for particle detection and energy measurement in order to produce dose maps at a micrometric scale.

2.4.1 Scintillation and Scintillators

Scintillation [53] is a process of luminescence where radiation is absorbed, followed by the emission of light of a characteristic spectrum with lesser energy. For dosimetric applications, the luminescence originating from excitation by ionising radiation is called radioluminescence. A scintillator is a material (organic or inorganic) that exhibits scintillation when excited by ionising radiation.

Organic scintillators [27, 54] are aromatic hydrocarbon compounds that contain benzene ring structures connected in many ways. The fluorescence process in organics emerges from transitions in the energy level structure of a single molecule. Inorganic scintillators consist of transparent single crystals. Besides lacking tissue equivalence, they are too expensive.

When constructing organic scintillators, a large category of them will be based on organic molecules that possess certain properties, formed by the π-electron structure (illustrated in the figure 2.12).

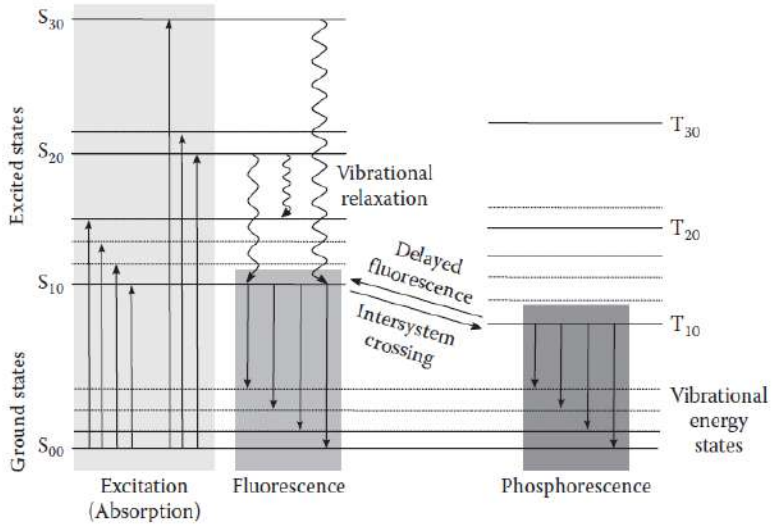

Figure 2.12: Jablonski diagram presenting the π-electronic atomic levels of organic molecules [27].

The main characteristics to take into account for scintillating are:

- Light yield, N (photons/MeV): Number of emitted photons per absorbed energy;
- Attenuation factor (cm^{-1}): Since radiation is known to cause damage to the equipment, the detector needs to be at a safe distance, which in turn will create an attenuation of scintillating light;
- Energy resolution (%): Ability of a material to set apart between two radiations with different energies;
- Decay time (s): Kinetics of the light response I(t) characterised by τ, that is given by the equation 2.5.

$$n(t) = \frac{N}{\tau} e^{-t/\tau} \tag{2.5}$$

where n is the rate of emission photons, N is light yield, t the period of time in study and τ is the decay time.

- Afterglow: Residual light output occurring after the primary decay time of the main luminescent centres;
- Stopping power: Attenuation coefficient of the absorbed radiation, for a given thickness of a material.

2.4.2 Birks' Law

Birks' Law describes the scintillation process of organic scintillators [27], relating the produced luminosity (or scintillation) with the deposited energy. Birks' formula relates the light yield per unit path length $\frac{dL}{dx}$ to the differential energy deposition of a charged particle $\frac{dE}{dx}$, using the scintillation efficiency S (%) and the quenching parameter kB (gMeV^{-1}cm^{-2}):

$$\frac{dL}{dx} = \frac{S\frac{dE}{dx}}{1 + kB\frac{dE}{dx}} \tag{2.6}$$

On a scintillator conversion [27], only a small fraction of the energy originally deposited in a material is used to produce the scintillation light.

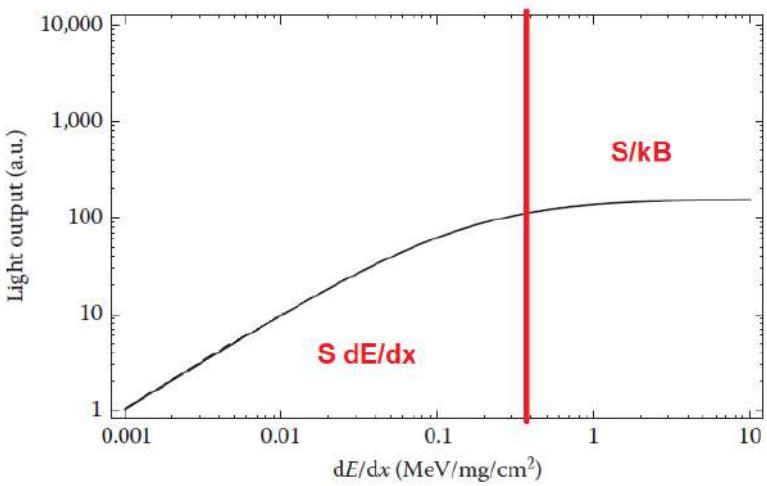

Figure 2.13: Light output as a function of specific energy loss dE/dx [27].

In figure 2.13, the behaviour of light output is depicted. If $\frac{dE}{dx} << 1$, $\frac{dL}{dx} \approx \frac{SdE}{dx}$ is the desirable range for study. However, if $\frac{dE}{dx} >> 1$, $\frac{dL}{dx} \approx \frac{S}{kB}$, meaning the light output will be independent from the energy loss, causing a phenomenon named quenching.

2.4.3 Quenching

The response of organic scintillators varies with the ionisation density of the incident radiation, which is usually quantified as the linear energy transfer (LET), mentioned in section 2.1. In therapeutic photon beams, the ionisation density is uniform throughout the beam and the rate of scintillation light emission is proportional to the radiation dose at any given location. However, in proton and heavy-ion beams, the ionisation density is characterised by a maximum peak at a maximum penetration depth. In the context of proton or heavy ion beam measurements,

quenching is manifested by a decrease in the height of a Bragg peak measured with a scintillator [27], as seen in figure 2.14.

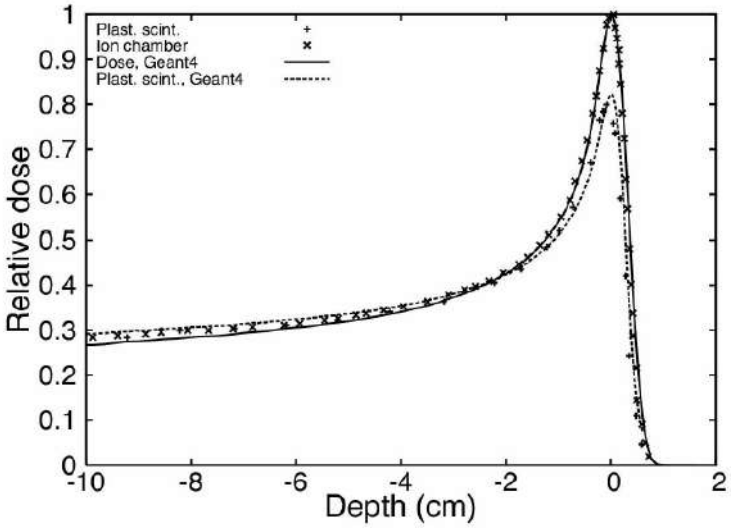

Figure 2.14: Relative dose depending of the depth describing the impact of scintillation quenching on a 155-MeV Bragg peak [55].

Even though there have been many studies concerning this particular subject, there is not a comprehensive description of the physical mechanism underlying ionisation quenching. There are two main proposed explanations for the quenching appearance:

- The saturation of the scintillator resulting that an increase in energy deposition will not lead to an increase in the light output (scintillation);
- The loss of scintillation efficiency with the increase of the ionisation density.

Experimentally, quenching is associated with the saturation of the signal. Due to this phenomenon, after a certain value of energy, even if the energy increases, the light output will not follow suit.

With the theoretical concepts needed for the development of this master thesis completed, in the following chapter, the methods and procedures for the laboratory work are discussed as well as the study of the detection chain's elements for the microdosimeter development.

Chapter 3

Methods

3.1 Experimental Setup

The experimental setup will reproduce the basic readout scheme of the microdosimeter. The scintillating materials, namely the optical fibres, absorb energy from the ionising radiation and emit several photons, with characteristic wavelength spectra proportional to the deposited energy. The resulting scintillating photons produced are first carried through the optical fibres until they reach the photomultiplier, where the photons are absorbed and transformed into an electrical signal readout by a data acquisition system, as seen in figure 3.1. The high voltage (HV) is the power supply to the photomultiplier.

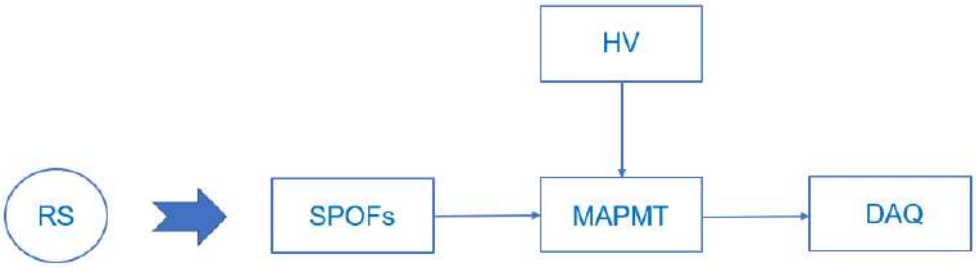

Figure 3.1: Block diagram with essential structures for scintillation dosimetry. RS - Radiation Source, SPOFs - Scintillating Plastic Optics fibres, MAPMT - Multi-Anode Photomultiplier Tube, HV - High voltage, DAQ - Data Acquisition System.

Before the full integration of the detector, each part will be independently validated with different instrumental setups, which are described in this chapter. On the final validation test, the scintillating plastic optical fibres (SPOF) ribbons are exposed to a radioactive source, and the signal is read by the multi-anode photomultiplier (MAPMT) and interpreted by the DAQ board.

3.2 Radiation Sources Characterisation

3.2.1 LED

A light-emitting diode (LED) [56] comprises a p-type and n-type semiconductor. With no tension applied, due to an internal electrical field, the electrons and holes are separated, drifting

to opposing sides. This, in combination with a built-in potential, creates a gap between the two semiconductors. However, by introducing a difference in potential on its terminals, that disturbs the balance of the electrons and holes and the diode starts conducting current. The electrons inside the semiconductor recombine with holes through a process of annihilation, resulting in the production of photons. The produced photons wavelength is determined by the energy required for electrons to cross the bandgap of the semiconductor used. One of the principal characteristics of LEDs is their current-voltage exponential curve, seen in figure 3.2(a). In figure 3.2(b), the different responses from various types of LEDs are shown.

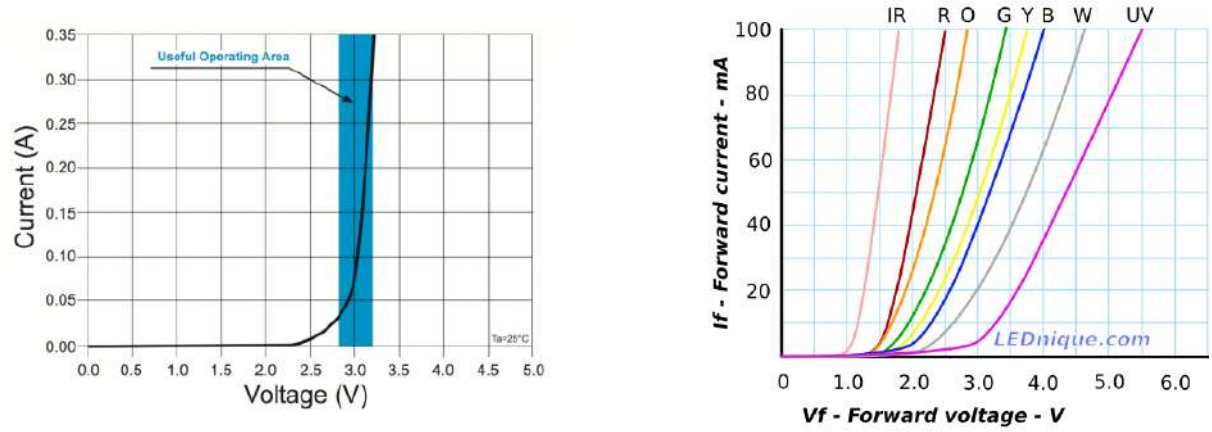

(a) (b)

Figure 3.2: (a) Useful operating area in more detail for a LED [57]. (b) Typical IV curves for various colours of LEDs [58].

The LEDs chosen were UV LED Roithner, more specifically the RLS-UV385 model. RLS-UV385 is an InGaN based ultraviolet LED, emitting at a peak wavelength of typically 385 nm. In this work, LEDs were used to characterise the whole readout system. To characterise the response of LED's emission spectrum a mini-spectrometer was used, seen in figure 3.3(a). A spectrometer [59] is an instrument used to measure light as a function of its portion of the electromagnetic spectrum.

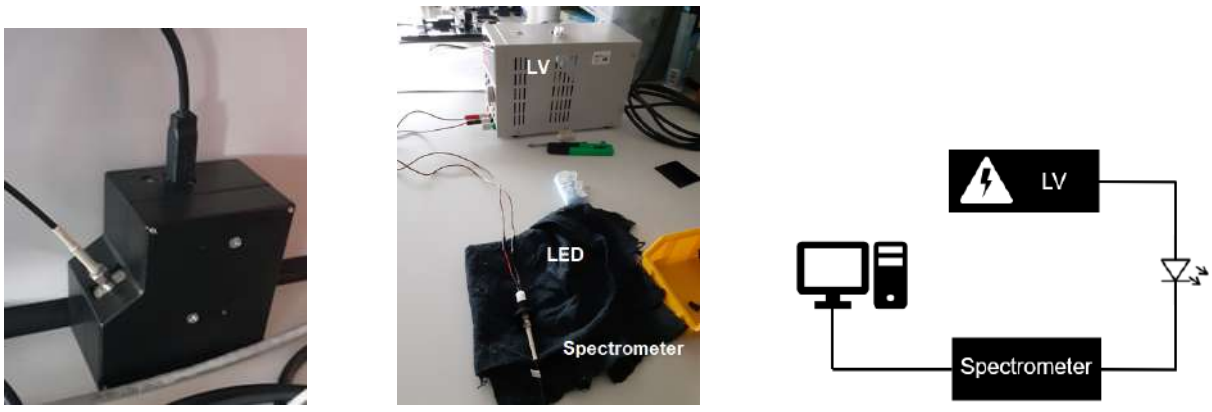

(a) (b) (c)

Figure 3.3: (a) Photograph of the mini-spectrometer, (b) the LED characterisation setup, (c) diagram of the circuit used for the characterisation setup.

In figure 3.3(b) the photograph of the LED characterisation setup can be seen and in 3.3(c)

is the diagram of said setup. A resistor is not placed at the terminals of the LED because the current values are maintained low since the low voltage (LV) instrument used allows the user to control the current values. The spectrometer used was a Hamamatsu C10082MD mini-spectrometer. The most important characteristics of these mini-spectrometer are presented in table 3.1 and figures 3.4.

Table 3.1: Some of the most important characteristics of the mini-spectrometer.

Parameter	
Spectral response range	200-800 nm
Spectral resolution	4 nm
ADC conversion	16 bit

The first graph (figure 3.4(a)) represents the spectral response from the mini-spectrometer, where the relative sensitivity is higher for the range of wavelength between 300 and 550 nm, including the wavelength in which the chosen LEDs operate. The next graph (figure 3.4(b)) shows the relation between spectral resolution and wavelength and by analysing the curve corresponding to the model C10082MD, at approximately 385 nm the spectral resolution will be slightly above 3 nm. The final graph (figure 3.4(c)) depicts how the ADC output depends linearly on the integration time.

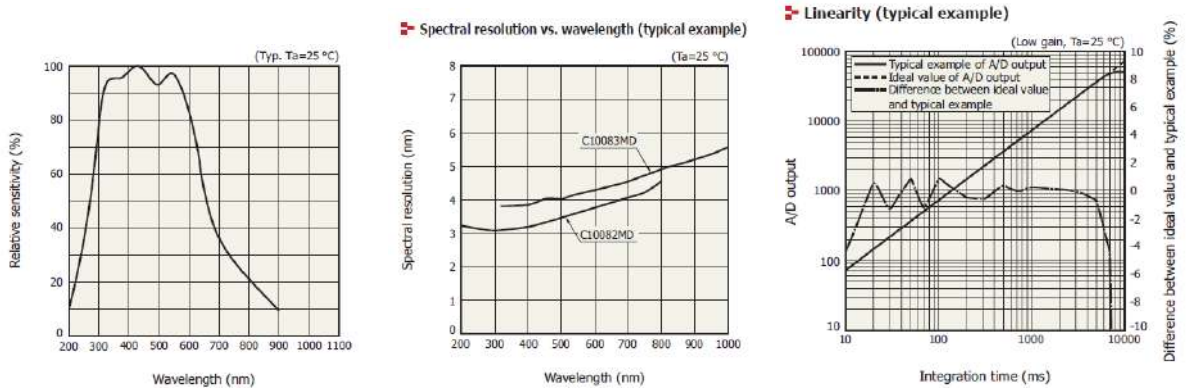

(a) (b) (c)

Figure 3.4: Spectrometer's characteristics curves that represent (a) the spectral response, (b) the relation between spectral resolution and (c) wavelength and the linearity.

The first step of the LED characterisation was to study the spectral response from different types of LEDs to choose which ones were more adequate to use in the validation tests.

3.2.2 Radioactive Sources

A radioactive source contains a known quantity of a radionuclide, which releases ionising radiation. Radioactive sources can have more than one type of decay, such as gamma, beta or alpha decay. One of their main applications is as calibration tools in experimental setups. In order to test the optical fibre's response, the following radioactive sources were selected:

- ^{137}Cs [in figure 3.5(a)];
- ^{60}Co [in figure 3.5(b)];

- ^{204}Tl [in figure 3.5(c)];
- ^{241}Am [in figure 3.5(d)].

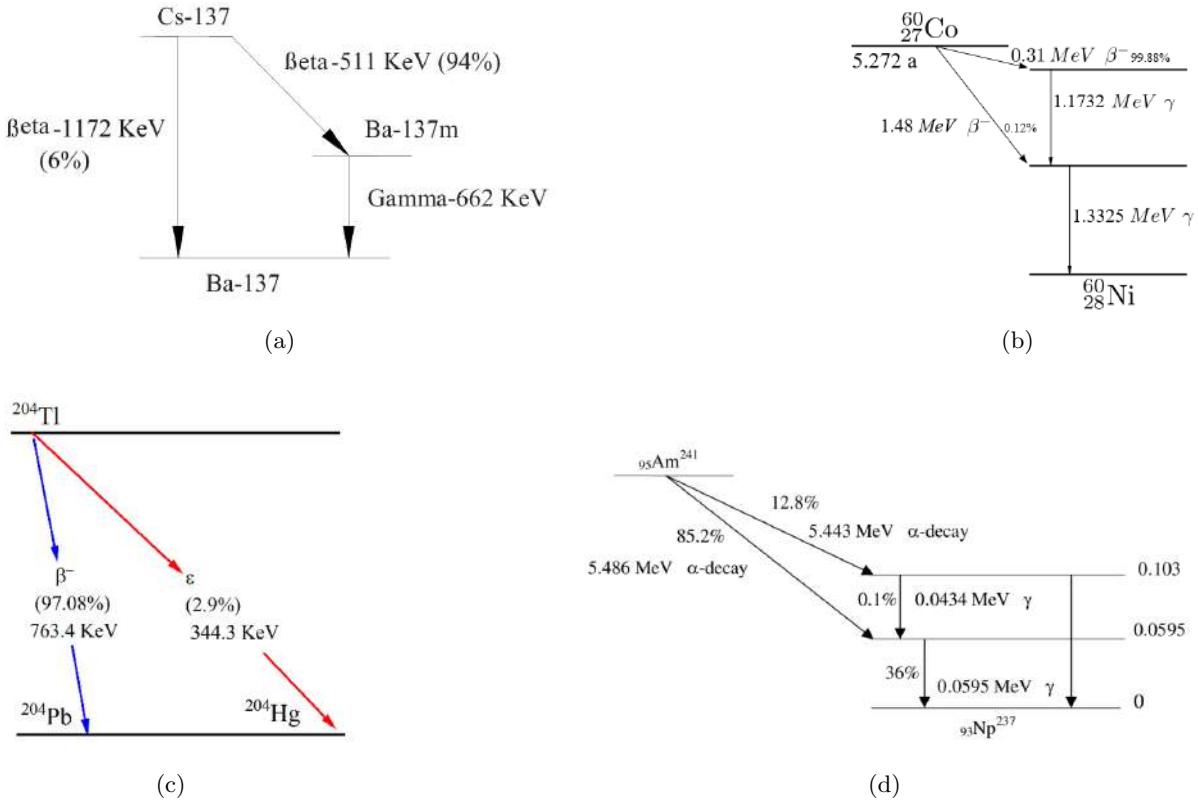

Figure 3.5: (a) ^{137}Cs decay scheme [60]. (b) ^{60}Co decay scheme [61]. (c) ^{204}Tl decay scheme [62]. (d) ^{241}Am decay scheme [63].

While both cesium and cobalt are radioactive sources with beta minus and gamma decays, thallium has both electronic capture and beta minus decays and Americium has alpha and gamma decay. These radiation sources were chosen due to their variety in energies and types of decay, allowing for an extensive study.

Table 3.2: Stopping Power and Range Tables for Electrons for the optical fibres material (Polystyrene) taken from NIST using the ESTAR program.

β Particles Characteristics		
Energies (MeV)	Stopping Power (MeV cm^2/g)	CSDA (g/cm^2)
0.3	2.309	0.08598
0.35	2.192	0.1082
0.5	1.989	0.1805
0.7	1.871	0.2846
0.8	1.84	0.3385
1	1.804	0.4484
1.5	1.781	0.7281

In the table (3.2) are the values of stopping power and range calculated for polystyrene, one of the most common materials of optical fibres for several energies, using the program Stopping

Powers and Ranges for Electrons (ESTAR) from National Institute of Standards and Technology (NIST). These energies are close to energies in the decay seen in figures 3.5.

An alpha particle is identical to the nucleus of a ^{4}He atom, which has two protons and two neutrons. For this reason, the alpha particles resemble most of the behaviour of protons, thus being the crucial decay for this study. Another table was drawn for the stopping power and range values for α particles as seen in table 3.3. These values were also calculated for the material polystyrene, using the same program as used for β particles.

Table 3.3: Stopping Power and Range Tables for α particles for the optical fibres material (Polystyrene) taken from NIST using the ESTAR program.

α Particles Characteristics		
Energies (MeV)	Stopping Power (MeV cm^2/g)	CSDA (g/cm^2)
5	875	0.003695
5.5	818.4	0.004286

However, since all the radioactive sources used have two types of decay and different energies, there is the challenge to distinguish the many decays when studying their response.

3.3 Scintillating Plastic Optical Fibres

3.3.1 Main Characteristics of Optical Fibres

Optical fibres are composed of two coaxial layers: core and cladding. The core is the inner part of the fibre, which guides the light, whereas the cladding surrounds it. As dielectric waveguides, the optical fibres transmit light by total internal reflection. They act as a connection between a light source and a light-measuring device.

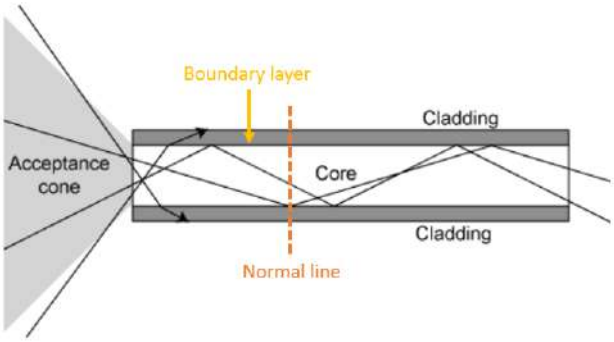

Figure 3.6: Diagram showing how light is guided through an optical fibre [64].

In figure 3.6, when light is incident at the boundary, it can either be reflected or refracted, depending on the incident angle. To better comprehend its behaviour, Snell's law is required, in equation 3.1:

$$n_1 \sin(\theta_1) = n_2 \sin(\theta_2) \tag{3.1}$$

where θ_i as the incident angle measured from the normal of the boundary (see figure 3.7) and n_i is the refractive index of the respective medium. To obtain total internal reflection (figure 3.7(c)) instead of refraction, some conditions must be met. First, for the light to be internally

reflected, the refractive index of the boundary layer must be higher than the refractive index of the medium where the light is transmitted, meaning, $n_1 > n_2$. Second, at a particular angle called critical angle (figure 3.7(b)), θ_c,the photons, rather than refracting into a boundary layer, will travel along the surface between the two media. Any angle above the critical angle creates the phenomena of total internal reflection. For calculation of the critical angle, the refractive angle, θ_2, must be 90° and, hence Snell's law can be rewritten in the following manner:

$$\theta_c = \arcsin(\frac{n_2}{n_1}) \tag{3.2}$$

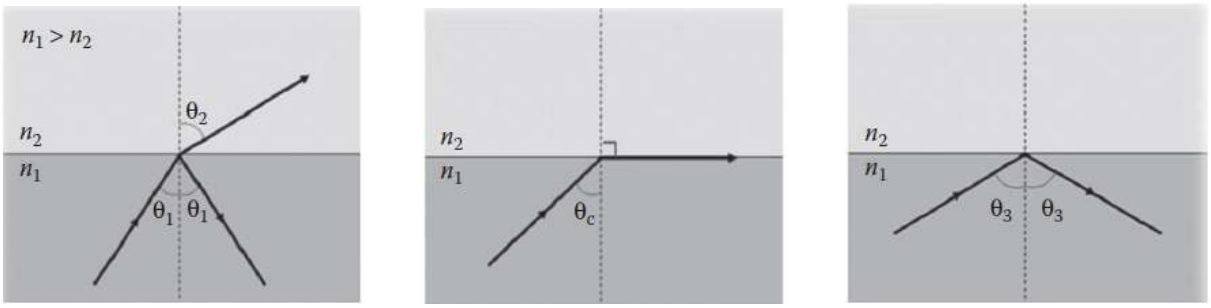

(a) (b) (c)

Figure 3.7: (a) Refraction and reflection at the boundary between two media with different refractive indices, (b) critical angle, and (c) total internal reflection [27].

3.3.2 The SPOF Kuraray SCSF-78

The optical fibres used were the Kuraray SCSF-78, which are distinguished by their three transparent regions: one core and two claddings. The plastic scintillator core is made of doped polystyrene (PS), the internal cladding is made of polymethyl methacrylate (PMMA) and the external one of a fluorinated polymer (FP), schematised in figure 3.8(a).

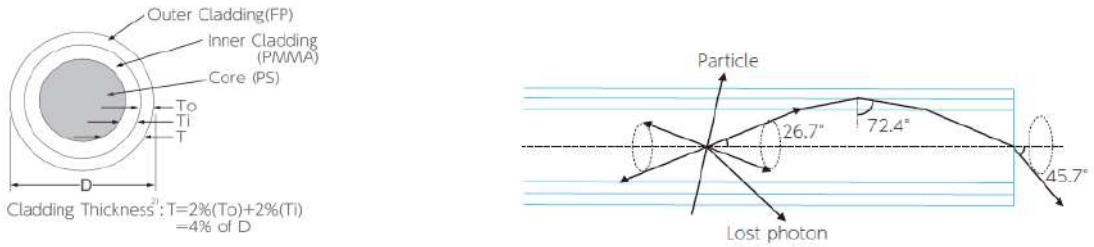

(a) (b)

Figure 3.8: (a) Cross section of a double cladding optical fibre as the Kuraray SCSF-78 and (b) light propagation diagram inside the Kuraray SCSF-78 [65].

Table 3.4: Refractive Index at the various parts that belong to the optical fibres.

	Refractive Index, n_D
Core	1.59
Inner Cladding	1.49
Outer Cladding	1.42

In figure 3.8(b), there is also a detailed diagram of the light propagation, including the critical angle, θ_c, which is 72.5°. In the following table (3.4) there are the various refractive index with corresponding region of these specific optical fibres.

SPOFs are the light sensor part of the proposed detector where its function is to create a distribution mapping of the ionizing energy, that gives a dose value.

3.3.3 Fibrometer

A fibrometer is a X-Y table with two motors with 100 μm precision covering an area of 3000x600 mm^2, as depicted in figures 3.9. This is a test bench of Laboratório de Instrumentação e Física Experimental de Partículas (LIP) part of the LOMaC laboratory, which is located in Faculdade de Ciências da Universidade de Lisboa (FCUL).

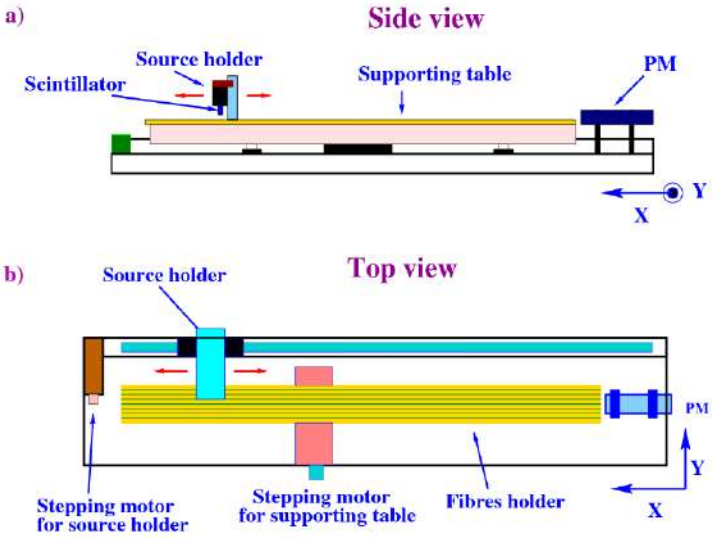

Figure 3.9: Schematic representation of the fibrometer from (a) a side view and (b) a top view.

Along the X direction, a light source is transported, whereas along the Y direction the table itself moves the test samples or setups arranged over the table. A photodetector (PMT EMI9813KB) is set up at a distance of 1 mm from the table. The PMT is placed inside a metallic shielding with a DuPont^{TM} lucite light guide with 15 mm length that is enveloped in Tyvek^{TM} paper distributing the light all over the photocathode surface. A set of collimators with rectangular slits are placed in front of the light guide to minimize any light coming from nearby fibres or other light sources; in fact, the noise level of the fibrometer is affected by the change of these collimators as it opens and closes the geometrical aperture of the photodetector.

In figure 3.10(a), there is an image of the inside of the fibrometer, showcasing what was just described. Using this configuration, some basic properties of the optical fibres are measured, such as attenuation lengths, relative light yields and light collection efficiencies; all these quantities are known to be dependent on the combination of the material, geometry, wavelength and/or type of excitation source.

The working plaque for these preliminary tests is already available at the laboratory, shown in figure 3.10(b), where the SPOFs used were positioned in the individual grooves with an empty groove between them. From this point on, the working table will be referred to as X-Y plaque.

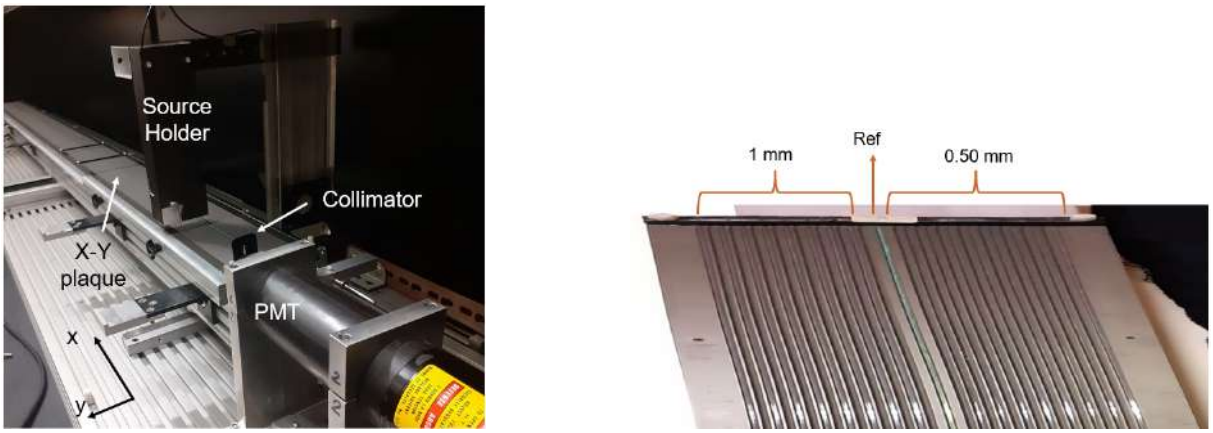

(a) (b)

Figure 3.10: (a) Photograph of the inside of the fibrometer and (b) photograph of the X-Y plaque with detailed explanation of how each section was divided with each SPOF's size.

In the middle of the plaque, there is a green WLS optical fibre and it acts as one of the reference optical fibres during these measurements (placed in spot 9 in X-Y plaque). The other green WLS reference optical fibre is placed on the X-Y table of the fibrometer acting as a fixed reference, a universal baseline to all fibrometer measurements.

XT-Plaque

In order to study the optical crosstalk present in juxtaposed optical fibres, another working plaque, the XT-Plaque, was used, which was developed at [66], seen in full view in figure 3.11. The plaque is 1050 cm long, 130 cm wide and has a height of 10 cm. This setup allows the study between optical fibres diameters of 1, 0.5 and 0.25 mm, simultaneously.

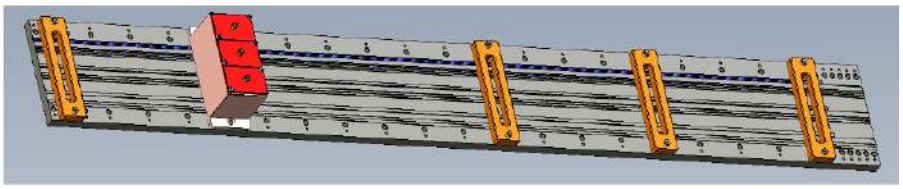

Figure 3.11: Schematic of XT-plaque designed at [66].

With a zoomed view seen in figure 3.12, it is clearly divided into three sections.

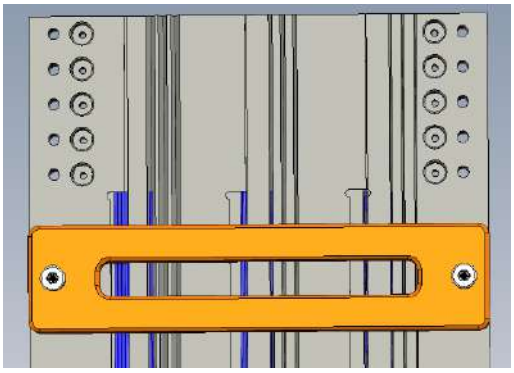

Figure 3.12: Zoomed in view of the plaque [66].

Each section has one groove with a width of 5 mm, and next to it, there are 3 separate grooves with the fibre-specific diameter, acting as a baseline for the measurements. In figure 3.12, it is important to highlight that there is a possibility to have only one optical fibre being illuminated without having any neighbouring optical fibres. In both figures 3.11 and 3.12, there are orange pieces placed on the table, which serve the purpose of tightly holding the fibres in position during measurements.

The light sources used are held in three individual boxes, each one holding two LEDs used as excitation sources for the optical fibres, as seen in figure 3.13, and integrated into a designed support. A tower, in red in figure 3.11, holds three individual boxes. In figure 3.13, the tower with the three boxes mounted and the inside of the box are shown.

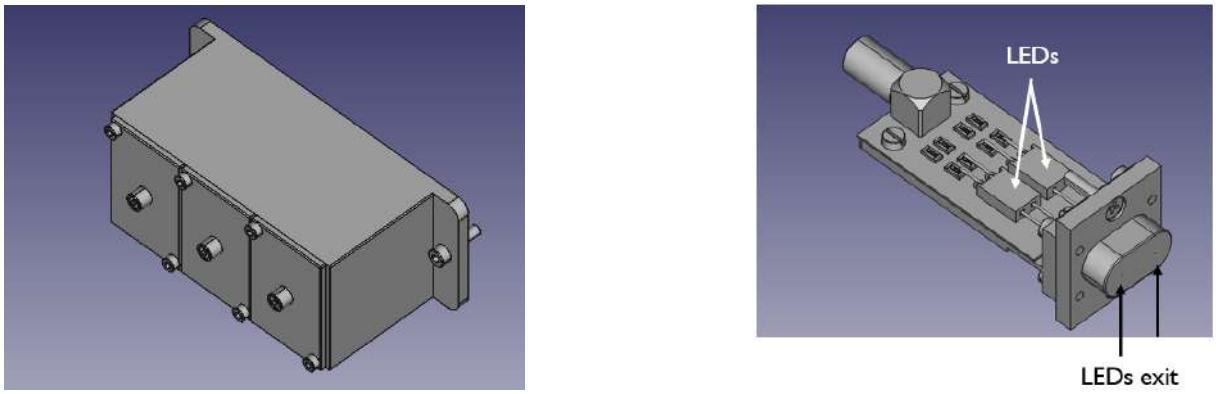

(a) (b)

Figure 3.13: Schematic of (a) LED support box and (b) LED box designed at [66].

The only difference between the boxes is the size of the pin-hole's aperture facing the optical fibres. The size of these pin-holes is half of the diameter of the optical fibre and are aligned with the corresponding fibre axis.

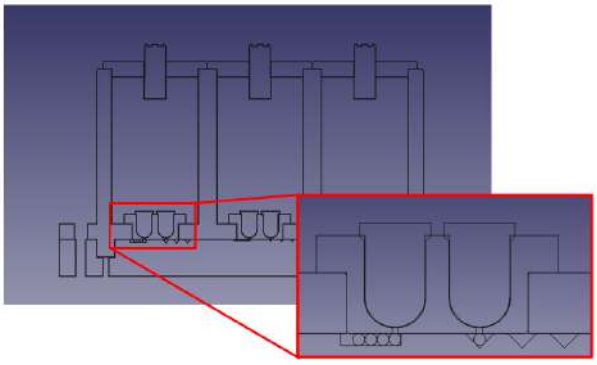

Figure 3.14: Schematic of the cross section of the tower positioned over the plaque showcasing how the LEDs illuminate the SPOFs.

One of the LEDs illuminates the single optical fibre and the other illuminates the first optical fibre in the ribbon, see figure 3.14. Due to the fact that two LEDs are needed for the experimental setup, even if the LEDs have the same reference, there are going to be differences in current-voltage responses.

In figure 3.15(a), there is a photograph of the XT-plaque integrated inside the fibrometer, with important objects carefully labelled. Next to it (3.15(b)) there is a photograph of the

SPOFs being illuminated by the LEDs, simulating the crosstalk study. Besides showcasing how what is seen in figure 3.14 and mentioned before, it also shows how the light behaves in the Ribbon SPOFs, visibly transferring light between each other, excluding that the phenomenon occurs due to optical aberrations. However, this image was taken with the LEDs having a higher voltage then the one which will take the crosstalk measurements.

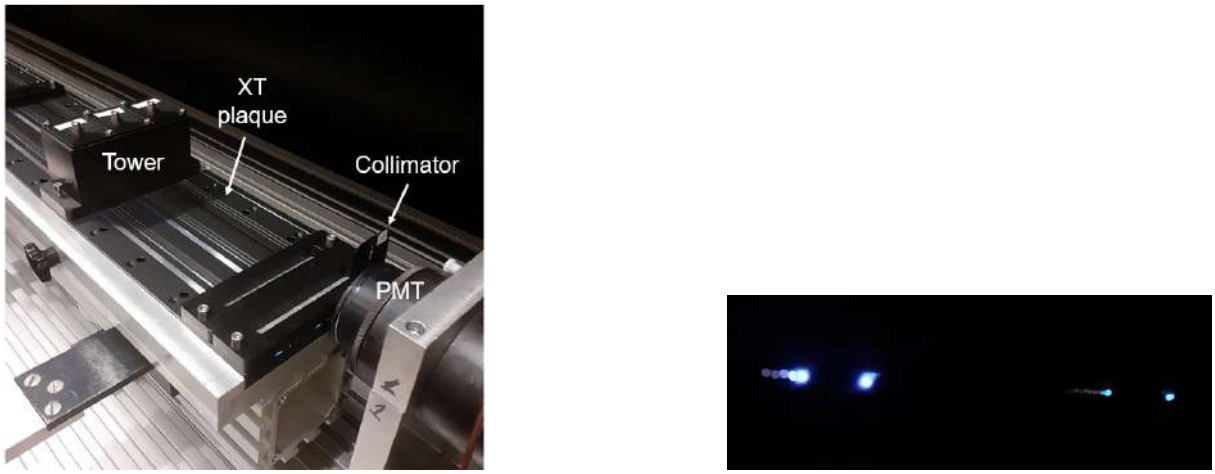

(a) (b)

Figure 3.15: Photograph of (a) the experimental setup for the crosstalk measurements and (b) how the SPOFs are illuminated by the LED inside the tower. Only the Isolated SPOF and the first Ribbon optical fibre are illuminated by the LED, but light is reaching the neighbouring optical fibres, since their outlines are visible.

3.4 Photomultiplier

3.4.1 Properties of Photomultipliers

A photomultiplier tube (PMT), see figure 3.16(a), is a vacuum tube consisting of an input window, a photocathode, focusing electrodes, an electron multiplier and an anode.

In figure 3.16(a), the structure of a photomultiplier with its parts labelled is shown. The light reaching the faceplate of a PMT is detected and produces an output signal through the following processes [67]:

1. Light passes through the input window;
2. Light excites the electrons in the photocathode so that photoelectrons are emitted into the vacuum (external photoelectric effect);
3. Photoelectrons are accelerated and shaped by the focusing electrode onto the first dynode where they are multiplied by means of secondary electron emission. This secondary emission is repeated at each of the successive dynodes;
4. Secondary electrons are collected at the anode.

In this study, the intention is to read several signals from the optical fibres at the same time, which means several anodes. A PMT only has one anode, thus a multi-anode photomultiplier (MAPMT) is used, its structure illustrated in figure 3.16(b).

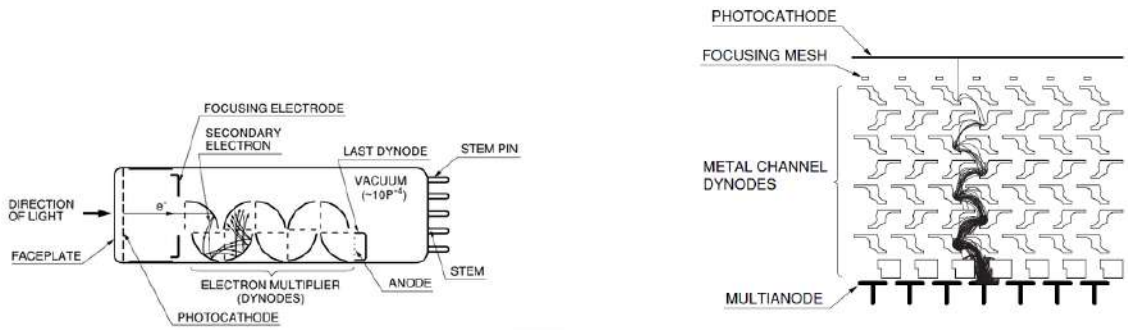

(a) (b)

Figure 3.16: Structure of (a) a single photomultiplier and (b) multi-anode photomultiplier [67].

Photoelectron Emission

Photoelectric conversion is broadly classified into:

- External photoelectric effects by which photoelectrons are emitted into the vacuum from a material;
- Internal photoelectric effects by which photoelectrons are excited into the conduction band of a material.

The photocathode has the first effect while the second is used in other physics applications, such as photoconductive or photovoltaic effect. Photocathodes can be classified by photoelectron emission process into a reflection mode, if the photoelectrons are emitted on the opposite direction of the incident light, and a transmission mode, if the direction is the same.

Electron Multiplier (Dynode Section)

Photoelectrons emitted from the photocathode are multiplied by the first dynode through the last dynode. When a primary electron with initial energy strikes the surface of a dynode, σ secondary electrons are emitted. This σ is the number of secondary electrons per primary electron and it is called the secondary emission ratio.

Electron Trajectory

In order to collect photoelectrons and secondary electrons efficiently on a dynode and also to minimize the electron transit time spread, electrode design must be optimized through an analysis of the electron trajectory. Electron movement in a photomultiplier tube is influenced by the electric field which is dominated by the electrode configuration, arrangement, and also the voltage applied to the electrode. This parameter is extremely crucial, because the photoelectrons emitted from the photocathode must be efficiently focused onto the first dynode.

Anode

The anode of a photomultiplier tube is an electrode that collects secondary electrons multiplied in the cascade process through multi-stage dynodes and outputs the electron current to an external circuit.

3.4.2 The MAPMT Used

Used for this project was an MAPMT model H8500 8x8 64-anode from Hamamatsu, allowing the continuous readout of multiple input signals as foreseen for the multiple scintillating optical fibres of the microdosimeter. The graphics in figure 3.17 describe typical responses from the MAPMT used. In figure 3.17(b), it is shown how the gain depends linearly on the supply voltage values, the gain rising with the increase of voltage.

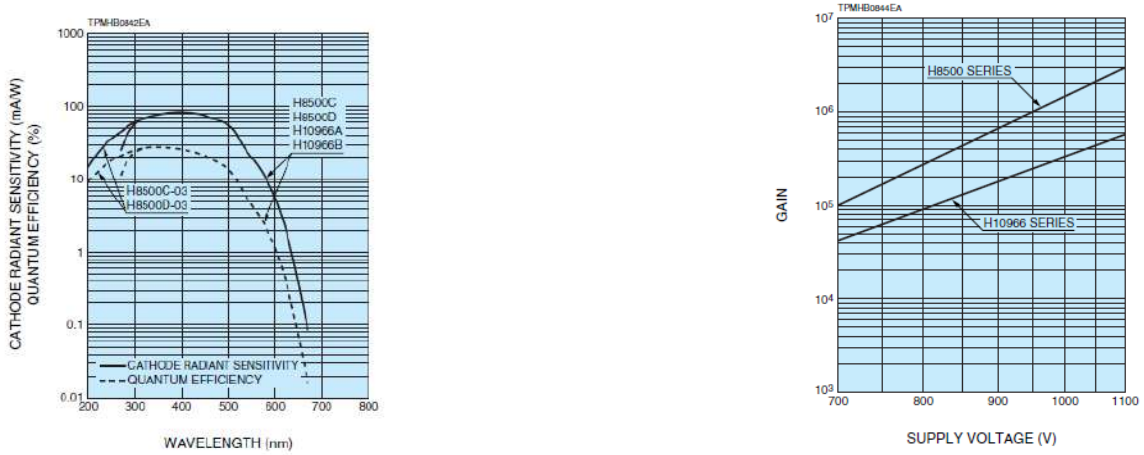

(a) (b)

Figure 3.17: (a) Typical spectral response for the MAPMT (H8500D) used and (b) typical gain [68].

This MAPMT has as relevant characteristics:

- Large Effective Area: 49 mm x 49 mm;
- Quantum Efficiency is the number of photoelectrons emitted from the photocathode divided by the number of incident photons. This model of MAPMT has a Quantum Efficiency of 25% for a wavelength of 400 nm, as seen in figure 3.17(a);
- Spectral Response with a range between 300 nm to 650 nm, with a peak at 400 nm.

3.4.3 MAPMT's Characterisation

In order to carry out the MAPMT characterization, an adequate experimental setup was assembled at LIP, shown in figure 3.18, which included a UV LED Roithner peaking at 385 nm, scintillating optical fibres SCSF-78 (scintillation peak at 437 nm (blue)) coupled to the Hamamatsu H8500 photodetector, power supplied using an ORTEC 556 high voltage source.
For the LED power supply a TENMA 72-4820 low voltage source was used and MAPMT anode currents values were measured using an Keithley 6487 picoammeter. These current values were firstly analysed using a Tektronix AFG3000 osciloscope to check on the anode current impulse characteristics. A black box was used not only to prevent exterior light interference with the experimental measurements but also the colour black protects any secondary light reflection inside the box. Moreover, the MAPMT when connected to high voltage, cannot handle being exposed to ambient light, because it can get permanently damaged and ruined. Inside the

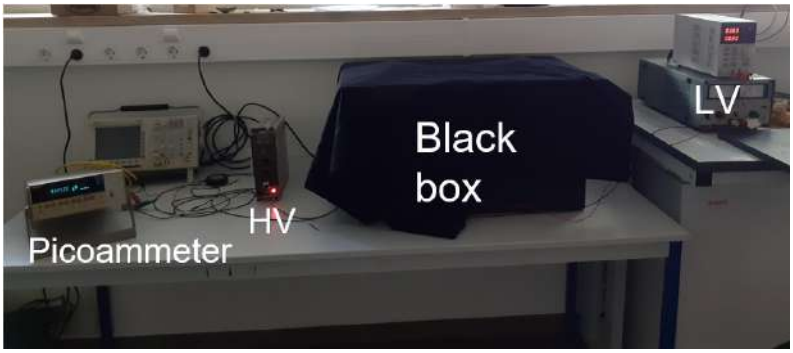

Figure 3.18: A black box ensures that no light interacts with the setup. The HV ranges from −700 V to −1000 V to power the MAPMT and the LED is powered using a LV source (2.6 V – 2.82 V). The annode current are measured using a picoammeter.

black box, the MAPMT, the LED and the optical fibres are placed to make the characterisation measurements.

A small irradiation box was prepared, visible in figures 3.19, with an input for the LED and two holes for optical fibres, where they can pass through the box, keeping the optical fibres and the LED in place during the measurements.

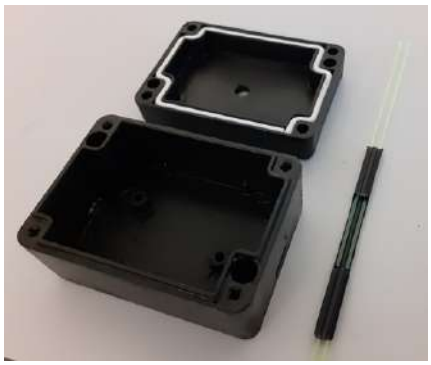

(a)

(b)

Figure 3.19: (a) Photograph of the inside of the irradiation box with its elements disassembled with the guide used to keep the optical fibres in the due location and (b) the interior of the irradiation box with the its elements assembled.

A customised connector allows the correct positioning of the optical fibres in relation to the MAPMT cells. Using the software SOLIDWORKS®, the connector was designed with 64 holes, pointing to the center of the 64 MAPMT cells. As can be depicted in figure 3.20, the holes are shaped like two cones with the vertices together. One of the cones has an outer face of 1.2 mm in diameter to facilitate the entry of optical fibres in the connector then it gets progressively thinner until the internal face has a 1 mm diameter, which locks the optical fibre and avoids unwanted movements during measurements. The other cone has a reverse shape, having a bigger outer diameter (3 mm), making it easier for the optical fibres to light the whole photocathode cell. The connector was manufactured with a filament 3D printer[1].

[1]Acknowledgements to Professor Daniel Galaviz for printing the connector.

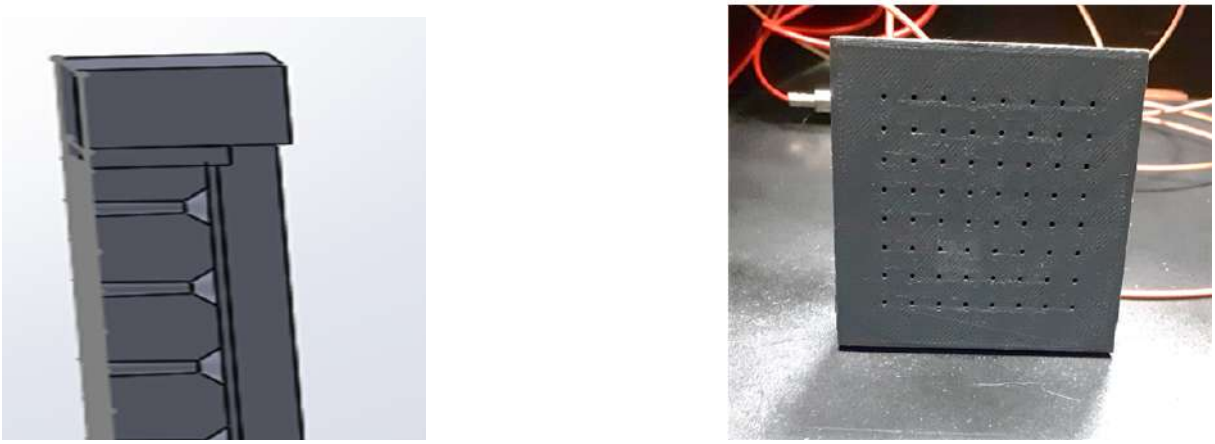

(a) (b)

Figure 3.20: Connector used for the communication between the optical fibres and the PMT. (a) The CAD design and (b) the connector manufactured with the 3D printer.

3.4.4 Data Acquisition

Picoammeter

For the characterisation of the MAPMT, the current was measured using a Keithley Model 6497 picoammeter. This instrument allowed a predetermined number of counts to be acquired and statistical parameters, such as average, standard deviation, peak-peak values, minimum and maximum peak value to be printed. An important factor to take into consideration is the integration time, which is normally defined as the interval of time that the detector collects input signal before passing the accumulated charge to the AD converter for processing. During the use of the picoammeter, a slow rate key was selected which had an integration time of 5 power line cycles (PLC) that is 100 msec [69].

DAQ Board

The data acquisition system (DAQ) [70] used for this experimental setup was developed for the Muon Array with Resistive Plate Chambers for Tagging Air showers (MARTA) project developed at Laboratório de Instrumentação e Física Experimental de Partículas (LIP). The MARTA concept was studied and consists of four Resistive Plate Chamber (RPC) units installed under a WCD (water Cherenkov detector). A MARTA unit consists of a segmented RPC with 64 pads, a data acquisition (DAQ) system, in figure 3.21, high voltage and a monitoring system inside a sealed aluminium case. For this master thesis work, the focus will only be on the DAQ board functions, in particular, validating the energy measurements using this DAQ board combined with a MAPMT. In the MARTA project the goal was obtaining measurements concerning cosmic muons positions and rates, disregarding the energy measurements functionality. The possibility of extracting an energy measurement, the read-out of 64 channels and the relative low-cost necessary to adapt this readout board to the MAPMT motivated the interest in studying the performance of this DAQ board for the measurement of energy.

The DAQ board main components are a 64 channel ASIC (MAROC3), which digitizes the RPC signals, and a low power field-programmable gate array (FPGA) that reads the 64 digital outputs, stores them and sends them to a PC. The ASIC [71] designed for the readout of

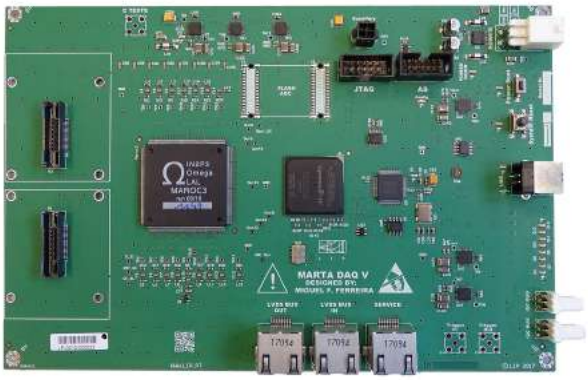

Figure 3.21: MARTA DAQ board picture.

64 channels MAPMT, already includes the shaping and pre-amplification for each individual channel and allows channels signal equalization. The DAQ user interface is made through shell-based commands from Linux using a USB communication port. Data is saved in standard format for analysis with the rate of events per second as function of the ADC Counts in the ROOT/CERN framework. The used ADC is a Wilkinson ramp type ADC which measures the number of clocks between a specific reference and the held peak value, with a frequency of 25 nsec [70].

3.4.5 Definition of DAQ Parameters

Name	Bit number	.txt line	.txt input	MARTA configuration	Comment
DacOnOff	0	1	0 or 1	1	-
OtagOnOff	1	2	0 or 1	1	-
SmallDac	2	3	0 or 1	0	Smaller DAC1 slope
DAC1	13 - 22	4	0 to 1023	210 - 300	D1 threshold value
DAC2	3 - 12	5	0 to 1023	0	D2 threshold value
EnOutAdc	23	6	0 or 1	0	Enables ADC output ('0' for enable)
InvStartCmptGray	24	7	0 or 1	0	Inverts the start ADC polarity ('0' for enable)
Ramp8bit	25	8	0 or 1	0	8 bits ADC
Ramp10bit	26	9	0 or 1	0	10 bits ADC
Mask1_ch0 - 63	27 - 154	10 - 73	0 or 1	0	Enables D1 outputs (channel 0 to 63,'0' for enable)
Mask2_ch0 - 63		74 - 137	0 or 1	1	Enables D2 outputs (channel 0 to 63, '0' for enable)
CmdCKMux	155	138	0 or 1	0	-

Figure 3.22: Extract from the ASIC configuration table and its configuration in bits. The table includes the signal name, the bit order, line, and possible input in the .txt file, the default MARTA configuration, and comments on each parameter. '1' is 'enable' unless stated [70].

When defining the DAQ parameters, the most important part is to understand what parameters of the ASIC are configurable and which of them are needed for this study.

In figure 3.22, there is a selection of the parameters that were changed during the testing of the DAQ. The two most important are the threshold and inputs comparators, D1 or D2. The threshold is the boundary in which the signal is distinguished from background noise. This value is set on the comparator's input and, if the input signal is inferior to the set value, the input is not acquired.

In the following chapter, the results from the various tests are shown and discussed in greater detail.

Chapter 4

Results Analysis And Discussion

4.1 Optical Fibres Characterisation

The end goal of the scintillating plastic optical fibre's (SPOF) characterisation is to understand how the SPOF behave when placed in a ribbon. From measuring the light yields diameter dependence, light attenuation factors and crosstalk between fibres placed in a ribbon will guides us on defining the construction parameters of the microdosimeter mentioned in 1.3.

4.1.1 Identification of an Adequate Light Source (LED)

As referred on the section 3.3.3, the fibrometer is used to carry out this characterisation. The first step is to study the basic properties of the SPOFs using X-Y fibre holder plaque (X-Y plaque, which configuration is mentioned in section 3.3.3). This particular plaque has two types of optical fibres: SPOF (SCSF-78) and WLS green (Y-11) optical fibres. The latter are reference optical fibres used during these measurements. With the intent of having a similar response between the two types of optical fibres, an adequate LED must be selected and it is where this characterisation starts.

In order to choose an adequate LED for the SPOF's studies, four different types of LEDs were tested (table 4.1) on SCSF-78 and Y-11 optical fibres. Since the setup inside the fibrometer system has these two types of optical fibres, the LED must create a similar response in both, to not exclude any signal when making the future measurements. The LED's intensity values comes in ADC counts, a value between 0 and $2^N - 1$ where N is the ADC resolution[1]. Each count representsan increment of $\frac{V_{REF}}{2^N - 1}$, voltage of the least significant bit, $V_{REF} = 5$ V.

Table 4.1: Comparison of LED's response to different coloured optical fibres measured by a spectrometer.

LED's Intensity ± Standard Deviation (ADC Counts)					
Excitation Sources		RLS-UV385	NS 370L	NS 360L	RLS-UV380
Optical Fibres	Y-11 (G)	328.1 ± 2.3	315.9 ± 2.6	761.5 ± 2.4	314.5 ± 2.2
	SCSF-78 (B)	324.9 ± 2.3	494.9 ± 2.5	82.4 ± 2.0	1707.8 ± 2.2
B/G		1.01	0.64	9.24	0.18

Based on the ratio between the SCSF-78 and Y-11 optical fibres (B/G), the LED chosen was

[1]The mini-spectrometer C10082MD used has an ADC with resolution of 16 bits.

the UV Roitner LED, model RLS-UV385, because the response displayed on the SCSF-78 is the closest to the Y-11. However, due to unforeseen events, the initial setup for the measurements with the X-Y plaque had to be slightly altered, by changing the LED and introducing a light mixer inside the excitation source holder. The light mixer (figure 4.1(a)) is a PMMA slab with a purposefully dimness surface, which creates a more uniform light field. The LED used for these measurements was the NS 370L.

(a)

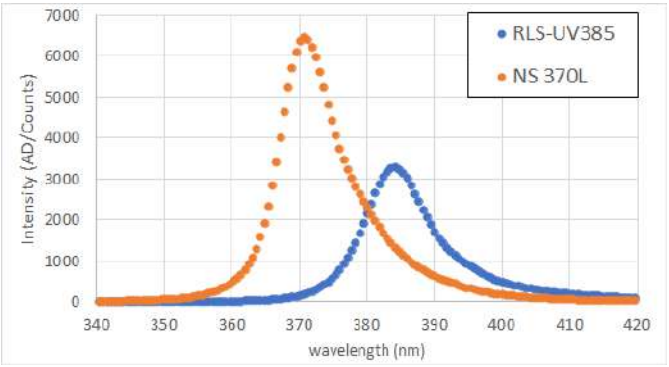

(b)

Figure 4.1: (a) Photograph of a light mixer produced by the physics department mechanical workshop. Its surface is dimness to diffuse the light in order to obtain a uniform light field and (b) intensity measured on each LED using the mini spectrometer C10082MD as a function of wavelength.

In figure 4.1(b), it is represented the intensity of the two LEDs (RLS-UV385 and NS 370L) measured by the spectrometer. The LED RLS-UV385 has signal in a range between $370 - 415$ nm, with a peak at 385 nm, while the LED NS 370L has a range of $355 - 405$ nm with a peak at 370 nm.

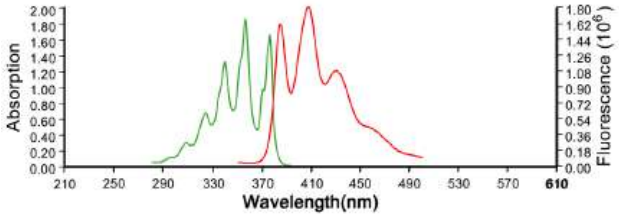

(a)

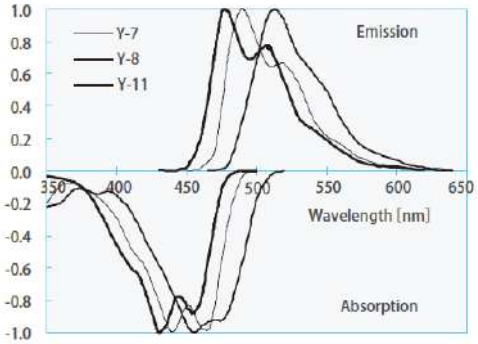

(b)

Figure 4.2: (a) Absorption (green) and emission (red) spectra of POPOP [72] and (b) absorption and emission spectra of WLS Y-11 [65].

In figure 4.2(a), the absorption spectra for the POPOP dopant (commonly used in scintilators) shows a close match to both of these LEDs which by itself would be enough to select them for the characterisation of scintillators. In terms of values, the absorption spectra is between 290 to 390 nm, which does include both wavelength values of the two LEDs. In figure 4.2(b), there is the absorption spectra of the optical fibres WLS Y-11, going from 370 to 470 nm, also including both LEDs emission spectrum.

4.1.2 Characterisation of Isolated Optical Fibres

In this section, the main operating steps of the fibrometer test bench and the characterisation of individual SPOFs are discussed. The fibrometer system is described in section 3.3.3. The chosen LED (NS 370L) was mounted into the source holder, seen in figure 3.9. Also, for these studies the X-Y plaque with the configuration described in the same section (3.3.3) was used.

To simplify the analysis of these initial measurements with the optical fibres, they will be referred by their positions in the X-Y plaque, as SX with X = 1, ..., 17. From optical fibres S1 to S8, they are 1 mm SPOFs and the first six SPOFs are new optical fibres, whereas S7 and S8 are old SPOFs. In this study, both types of 1 mm optical fibres are used, because while the proposed detector is going to have new SPOFs the old ones are currently largely available at LOMaC, useful for comparison tests and are going to be used to build the first detector's prototypes.

On S9, there will be the reference optical fibre, the WLS Y-11, and from S10 to S17 there are the 0.5 mm SPOFs. The other reference optical fibre, which is located outside of the X-Y plaque, is named S0. During the following scans, the programme starts by taking the response from S0 across its length and, at end of the scan, the process is repeated. The results are crosscheck and then the two results are ratio at the same distance (in this case 30 cm) to ensure that no significant uncertainties interfere on the measurements. For all the scans, this ratio value is below 3%.

Stability

Before any measurement with any instrument, there is a period of stabilisation that needs to be accounted for and the fibrometer system is no different. In figure 4.3, a typical fibrometer system response with time is shown after turning on the PMT high voltage and the LED.

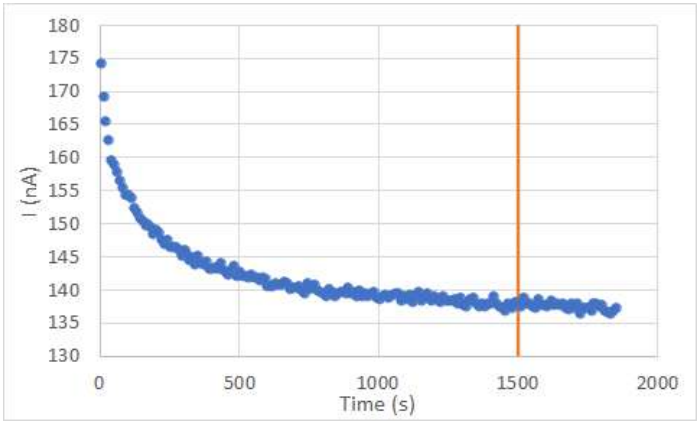

Figure 4.3: Fibrometer system response as function of time in seconds.

As seen in the figure 4.3, the fibrometer system response shows the tendency towards a value after 1500 s (25 minutes) time. To further analyse this graph, it was calculated the average and the standard deviation for an equal intervals of time, the results seen in table 4.2.

With the passage of time, the variation in values greatly decreases as it is stated in the table 4.2, implying a waiting period for a more accurate measurement. Thus, in the following measurements, a waiting time of 30 minutes was implemented. This waiting time is only applied

Table 4.2: Average and standard deviation values depending on the time.

Average ± Standard Deviation (nA) for Δt	
s	nA
t > 500 s	149.3 ± 7.2
500 s < t < 1000 s	140.4 ± 1.0
1000 s < t< 1500 s	138.47 ± 0.64
t ≥ 1500 s	137.59 ± 0.53

when the high voltage is turned off or is in stand-by mode, in which residual current keeps the PMT at a temperature close to the operational value, during long periods of time.

Transverse Scan

This scan is taken by fixing the position on the X-axis and scanning the response along the Y-axis of the fibrometer's table with the different optical fibres in study carefully labelled. In this scan the LED moves along the width of the table holding the fibres.

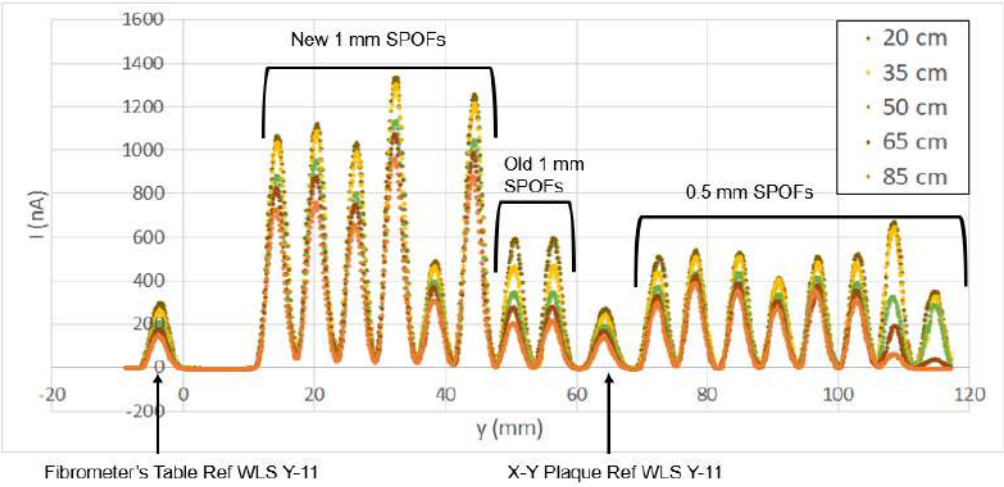

Figure 4.4: SPOF response measured on the fibrometer as a function of the Y-axis of the X-Y plaque.

In figure 4.4, the colourful curves are obtained with the excitation source, chosen in 4.1.1 (NS 370L), at different distances on the X-axis of the X-Y table, $x = [20, 35, 50, 65, 85]$ cm.

From figure 4.4, not all SPOFs have the same intensity. The SPOFs in the position S7 and S8, the signal is significantly inferior to the others, because, as referred in 4.1.2, both are old SPOFs. The last two peaks, positioned the furthest to the right, have the different behaviour in comparison to the other optical fibres. The last SPOF (S17) was shorter then the rest, measuring around 75 cm, therefore having a minor peak at 65 cm and non-existing peak at 85 cm distance. The second from the last (S16) appears to be broken around the 40 cm, thus its response is so inferior following the 50 cm position. Also, S5 has visibly lower intensity when compared to other responses from 1 mm SPOFs. This can be explained by other imperfections present in these SPOFs, such as bad polish of their tips. For these reasons, these three optical fibres will be disregarded during the analysis.

In table 4.3, there are the comparison between light yield values for all the optical fibres in

Table 4.3: Comparison between light yield values for different SPOFs.

Light Yield	
Ratio	Δ LY (%)
(0.5/1) mm	31 – 53%
(old/new) 1 mm	44 – 57%
1 mm new	77 – 97%
0.5 mm (S10-S15)	62 – 100%
1 mm (S1-S3)	92 – 97%
1 mm (S4 & S6)	94%
1 mm (S7-S8)	99%
0.5 mm (S10-S12 & S14)	94 – 100%

study and it is important to notice how the light yields range for different situations. For 1 mm new SPOFs, their values range between 77 – 97%. This difference comes from the difference in signal between the S1-S3 and S4 & S6 responses, which responses are also compared in the table, and their variation is visibly much lower. Comparing the response from the old and new SPOFs, old ones a lower light yields of about 31 – 53% is measured. In 0.5 mm SPOFs, S13 appears to have a lower signal, which makes the range of light yield bigger, from 62 – 100%. When taking this particular SPOF from the values, the light yield is between 94 – 100%.

From figure 4.4, overall, as the excitation source moves away from the PMT, meaning along the X-axis, the intensity given by the fibrometer system decreases with this distance.

From this measurements, besides measuring the light yields from optical fibres, it is also important to study if the fibrometer is in ideal conditions for the following measurements. In order to see if the fibrometer's table is aligned and well-positioned, each peak was normalised to its maximum value for the first and last X-axis position. Due to the large amount of peaks, it is difficult to accurately analyse this data and state if the peaks are aligned and overlapping each other. For this reason, it was zoomed in on a single peak, S4, as seen in figure 4.5.

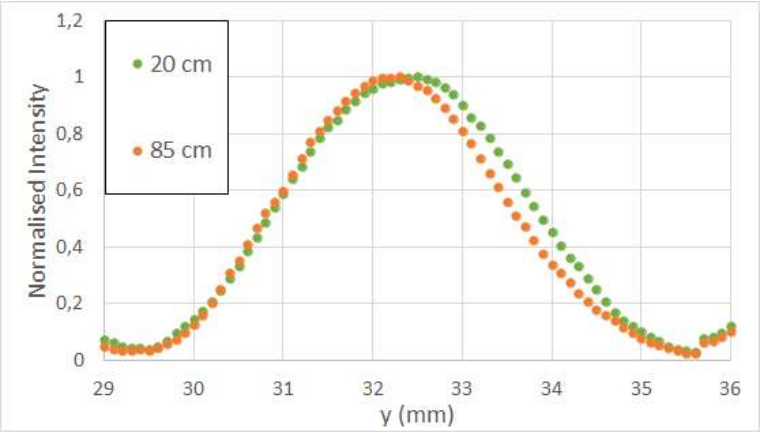

Figure 4.5: Normalised S4 response measured on the fibrometer system as a function of the y-axis of the X-Y plaque.

From figure 4.5, visibly, the peaks at 20 and 85 cm are mismatched, thus to see how the maximum (Y_{max}) varies in each X-axis position, the charts in figure 4.6 are drawn. The data were divided into three charts, as described in the caption of figure 4.6, and the values normalised

to their average for a clearer reading.

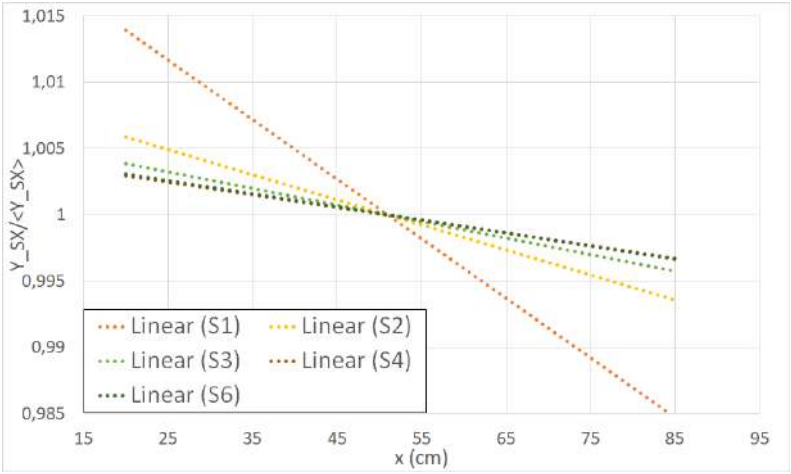

(a)

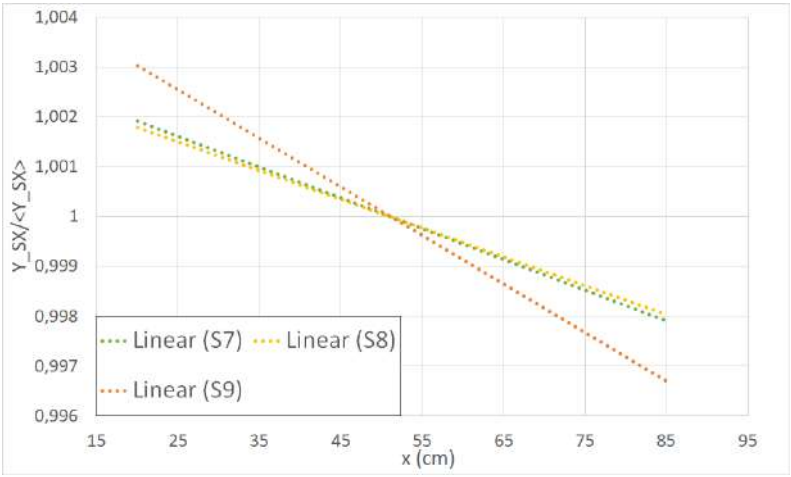

(b)

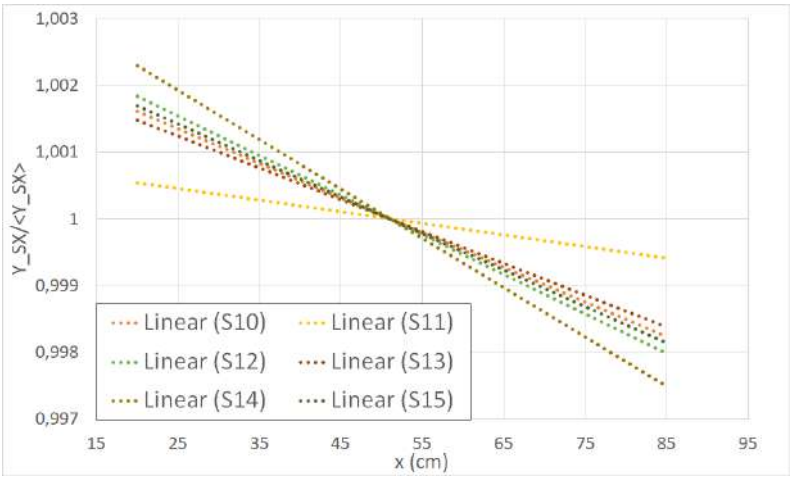

(c)

Figure 4.6: Deviation of measured Y_{max} from each fibre as function of the excitation source distance to the PMT for (a) S1 to S6 (b) S7 and S8 and WLS Y-11 and (c) S10 to S15.

Instead of the values, the tendency linear line for each optical fibre is plotted, because it better showcases the variation of the position maximum as function of the distance. In the

appendix A, there will be the same charts but with the normalised values for every optical fibre in study.

Table 4.4: Highest and lowest maximum's position for the optical fibres with the highest and lowest standard deviation.

Range (mm) of the Maximum Y-axis Position				
S1	S4	S9	S11	S14
14.5 – 14.0 mm	32.5 – 32.3 mm	64.5 – 64.1 mm	78.3 – 78.1 mm	97.0 – 96.4 mm

From table 4.4 there are highest and lowest best and worst standard deviation values, calculated by the variation of the maximum positions on the Y-axis.

To quantify a possible deviation angle (θ) in the fibrometer's table, we will take into consideration the deviation suffered by the reference optical fibre (WLS Y-11) is used, as seen in figure 4.7.

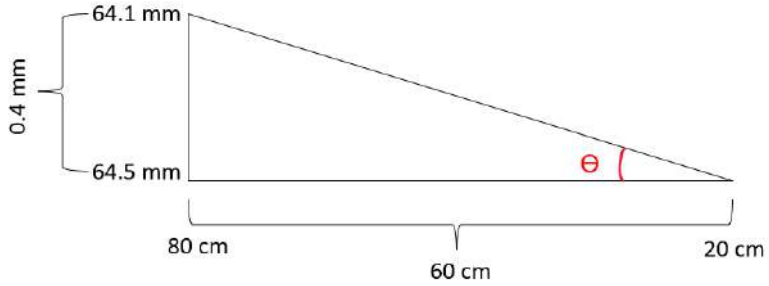

Figure 4.7: Visual representation of the study scheme.

Based on the known distances from the table 4.4, we will use the trigonometry function of tangent that correlates the opposite side (OS) to the adjacent side (AS) as observable in the next equation:

$$\tan(\theta) = \frac{\text{OS}}{\text{AS}} \iff \theta = \arctan\left(\frac{0.4}{600}\right) \iff \theta = 0.00067^{\circ} \tag{4.1}$$

The tilt present in the WLS Y-11 is 0.00067°, indicating that the fibrometer's table can have one side slightly forward than the other side. Due to the small angle's dimension, it is expected that there is no significant impact on the measurements. It should be noted that these differences are in accordance with the metrology measurements previously done on the fibrometer's table.

Longitudinal Scan

The longitudinal scan (LS), along the X-axis, gives the attenuation lengths and relative light yields of the individual fibres. During this scan, each optical fibre's response is analysed individually along their entire length. Various scans were made with different size steps between the distance of 20 to 80 cm. Each value acquired by the fibrometer system is an average of 10 consecutive measurements , and each measurement is the integration of the PMT's anode current during 330 ms (3 rd/s).

As mentioned in the section 3.3.3, the WLS Y-11 optical fibre is used as a reference optical fibre during these measurements. The typical response from this optical fibre is illustrated in

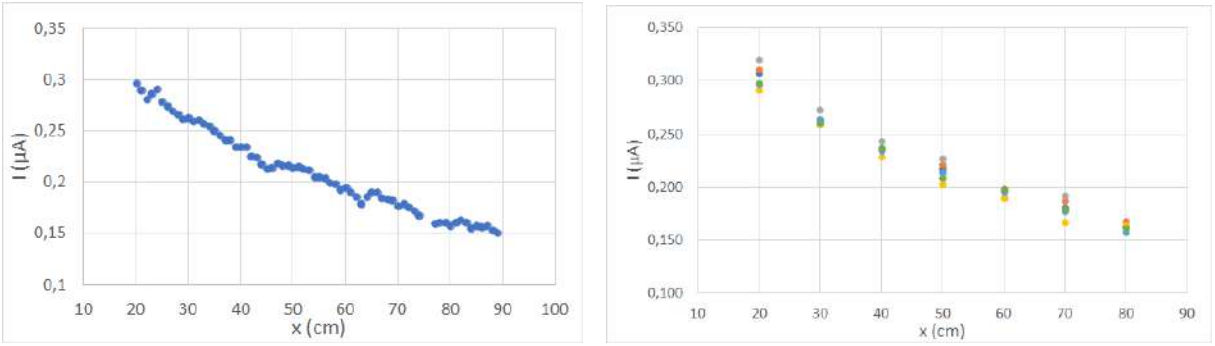

(a) (b)

Figure 4.8: (a) Measurement of the WLS Y-11 reference optical fibre as function of the distance of the excitation source (LED) to the PMT using a step of 10 mm between data measurements. The gap around $x = 75$ cm is the result from a cotton wire used to hold the fibres in position and (b) Sets of measurements of the WLS Y-11 response measured with the fibrometer system as a function of the distance.

figure 4.8(a). From this very thin measurement, there are visible fluctuations, which represent the limit of the current setup and result from the transport of the light source along the optical fibre length. For scintillating fibres which are slightly bend and difficult to place over the plaque, this effect is even larger. For the following measurements larger steps $d_x = 10$ cm were used as seen in figure 4.8(b), in which several set of measurements are overlapped. From these set of measurements three positions show larger dispersion $x = 20, 50, 80$ cm, but for reference is seen here that a higher standard deviation is at $x = 20$ cm, the values varying from 0.292 to 0.319 μA and the lower absolute deviation is at $x = 80$ cm, the values varying from 0.158 to 0.167 μA.

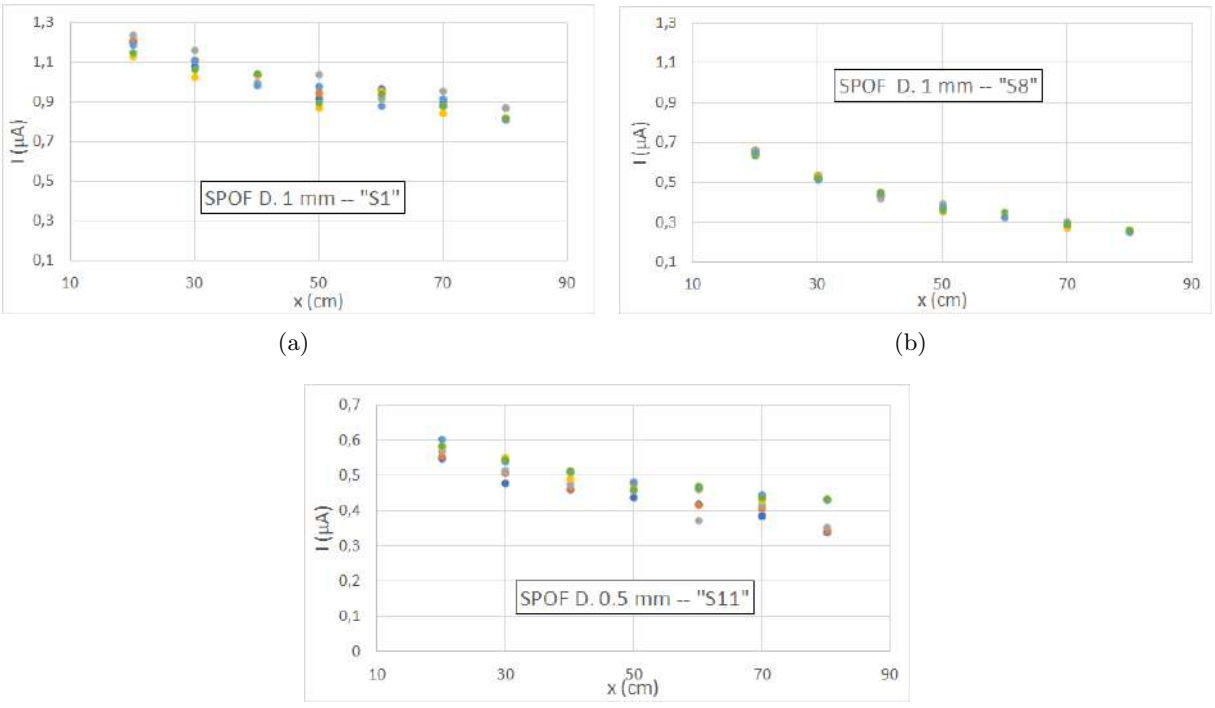

(a) (b)

(c)

Figure 4.9: Set of measurements of the SPOF response measured with the fibrometer as a function of the distance to the PMT using a 10 cm step.

Figures in 4.9 shows three examples of different optical fibres in study. The optical fibres were measured within the same run and each fibre was measured several times, these values are superimposed for each case. By analysing the results of the figures in 4.9, the SPOFs response depends on the distance, as the signal slowly decreases with the distance of the excitation source to the photodetector, along the length of the optical fibers. For 1 mm SPOFs (figures 4.9(a), 4.9(b) and 4.9(c)), there is a consistently larger variation around the position 50 cm, which indicates a systematic error throughout the measurements. For 0.5 mm SPOFs (figures 4.9(d), 4.9(e) and 4.9(f)), some positions have higher variation than others, like 20 cm and 50 cm. The systematic errors can have two sources: the experimental setup or the SPOFs itself, such as imperfections, bad polished tips or even the optical fibres being slightly curved. For the experimental setup issues can be originated from the motor's bearings, uncertainties in the measurement readings from the PMT or not correctly placed holders on the X-Y plaque. The experimental setup contributions identified at the moment are: motor's bearings (X-axis) ageing, light source distance to the plaque, point to point fluctuations due to the light source transport, uncertainty on the excitation light amplitude, uniformity and stability, PMT readout stability, fibres alignment over the X-Y plaque and the reported tilt on the fibrometer's table. The investigation on the origin of these errors, that may be a combination of all of the above mentioned, will not be covered but it is placed here for future reference.

For the 0.5 (and analogously for 0.25 mm in the future) diameter optical fibres there are additional aspects to be considered. Besides being difficult to handle and work with, the X-Y plaque design is made for 1 mm SPOFs only, making it difficult to use for 0.5 mm. As mentioned above, over the X-Y plaque there are holders to hold the SPOFs in place, but these holders are also made for 1 mm fibres.

For this scan, one of the main goals is to calculate the attenuation length values and it is used the following equation:

$$I = I_0 e^{-\frac{x-x_0}{L_{at}}} \iff \ln I = \ln I_0 - \frac{x-x_0}{L_{at}} \iff \ln I_0 - \ln I = \frac{x-x_0}{L_{at}} \iff L_{at} = \frac{x-x_0}{\ln\left(I_0/I\right)} \quad (4.2)$$

where x is the distance, x_0 is the initial distance, I/I_0 is the variation of the intensity and L_{at} is the attenuation length. With the aid of a spreadsheet and the functions of Microsoft Excel, to each intensity value it will be applied the natural logarithm and then using the function SLOPE as $-\frac{1}{SLOPE(I_x;x)}$ the L_{at} is calculated. In the table 4.5 are the obtained results.

Table 4.5: Attenuation length values for the several optical fibres on the X-Y plaque.

Attenuation Length		
SPOFs		L_{at} (cm)
old 1 mm	S7 and S8	60
new 1 mm	S3	150
	S5	160
	S1, S2 and S6	190
	S4	225
0.5 mm	S10	100
	S12, S13 and S15	150
	S11 and S14	160

From the table 4.5, the new 1 mm fibres show a variation in attenuation length from 150 to 225 cm. Also, it is important that the attenuation length is notably smaller for the older 1 mm fibres, being around 60 cm. For 0.5 mm SPOFs, their attenuation length ranges between 100 to 160 cm. These results were compared with the exponential fit from the spreadsheet, having a 5% difference, which is not a significant difference, thus the spreadsheet method will be used in future calculations. For cross validation the attenuation length was also calculated using the Y_{max} from the transverse scans at different X positions, as seen in figure 4.10 and an agreement of 6% was obtained.

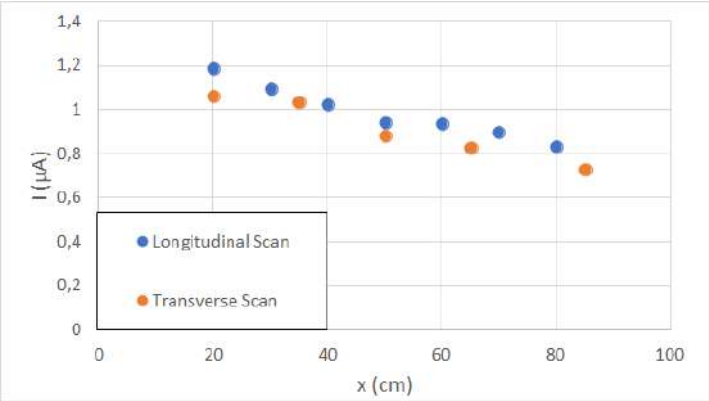

Figure 4.10: Comparison between the results obtained by the longitudinal scan and transverse scan.

4.1.3 Crosstalk Study

LED's Characterisation

The study of the crosstalk is done with a XT-plaque, as was mentioned in section 3.3.3. In figure 3.14(a) shows the excitation source holder and in figure 3.14(b) shows a detailed view of how each box has the LEDs positioned. For the crosstalk measurement a set of LEDs with the same reference RLS-UV385 were used. The LED holder has three boxes and, as seen in figure 3.11, each one pointing to the corresponding group of optical fibres (1, 0.5 and 0.25 mm as mentioned in 3.3.3). Due to their fragility and small dimensions, the diameter of 0.25 mm were deemed too hard to manipulate and characterise and, therefore, will not be included in this study.

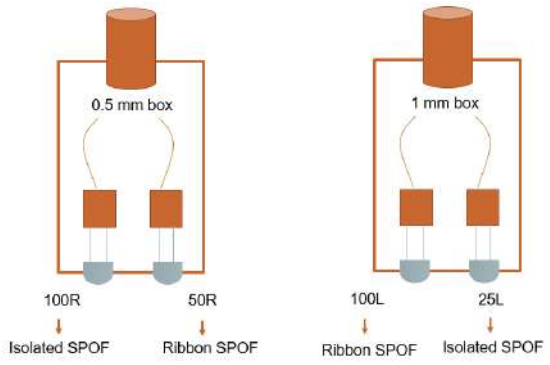

Figure 4.11: Distributions of the LED pair in the boxes of 1 and 0.5 mm inside the tower seen in the figure 3.13.

The label names are preserved for a backward crosscheck with preliminary studies done during LIP Summer Internship Programme [73] in which they have two identifiers: a number (100, 50 or 25) depending in each LED box they were positioned and a letter (R or L).

To each LED, 10 measurements were made using a spectrometer (Hamamatsu C10082MD), in which the first measurement was done 5 minutes after turning on the LV source, and the remaining ones followed up in sequence. Once more a waiting time is required for setup output signal stabilisation. The results are presented on table 4.6. It was chosen for the box made for 1 mm the LEDs label 100L and 25L and, for the box made for 0.5 mm, 100R and 50R, seen in figure 4.11.

Table 4.6: Comparison of the LED's intensities measured by the spectrometer.

LED's Intensity ± Standard Deviation (ADC Counts)				
Excitation Sources	100R	50R	100L	25L
Intensities	915.18 ± 4.76	960.16 ± 3.45	1150.9 ± 10.2	1212.3 ± 11.7

From the measurements with a spectrometer it was shown that the used LEDs have different intensities for the same applied voltage. The LED voltage used with the spectrometer was 3.0 V while at the fibrometer the used LEDs voltage is 2.7 V. This difference in voltages comes from the difference in gains of the two instruments: the spectrometer has a lower gain, then a higher LED voltage is needed than to the power the LED's inside the fibrometer, since higher LED intensities can damage the PMT inside.

A more detailed study was performed in order to determine a calibration factor for luminescence equalizations. The voltage-current characteristic curves are drawn for each chosen LED using a LV power supply and a Keithley 6487 picoammeter to read current values. The results are shown in figure 4.12, and for a close up in the values are in the table 4.7.

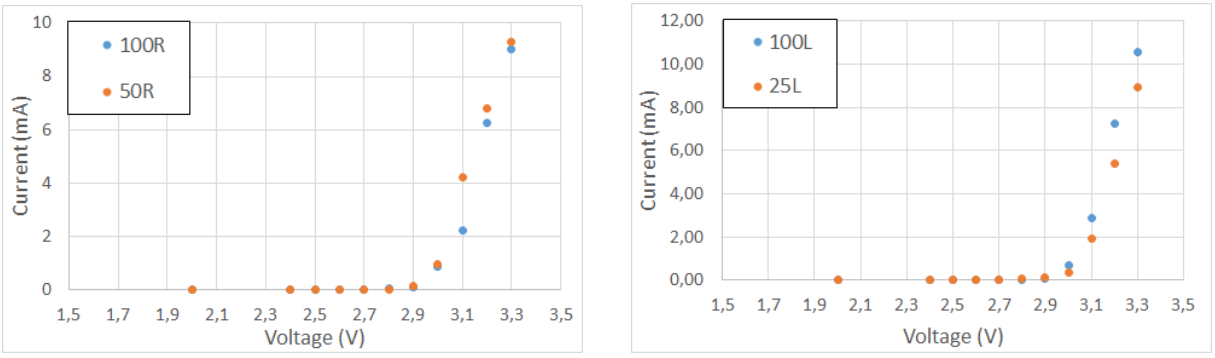

(a) (b)

Figure 4.12: Voltage-current characteristic curves of the LED pair inside the (a) 0.5 mm box and (b) the 1 mm.

It is expected that the number of photons is proportional to the current value ($N_{ph}^{LED} \propto I$), meaning the amplitude of the signal is not entirely related to its current. However, from the values in table 4.7, this basic principle does not happen, the differences between the LED's intensities when measuring with a spectrometer are not observable when using a picoammeter. From this study, we reach the conclusion that there is no clear requirement to apply a calibration factor.

Table 4.7: Voltage-current values for each pair chosen for voltage values in the region of interest.

Voltage-Current ± Standard Deviation				
V_{LED} (V)	I (μA)			
	0.5 mm LED box		1 mm LED box	
	100R	50R	100L	25L
2.6	1.48 ± 0.03	2.31 ± 0.01	17.8 ± 0.04	3.57 ± 0.07
2.7	11.58 ± 0.04	7.73 ± 0.01	27.5 ± 0.5	12.51 ± 0.04
2.8	48.8 ± 0.1	18.71 ± 0.04	40.2 ± 0.6	58.66 ± 0.07
2.9	118.1 ± 0.2	143.3 ± 0.4	89 ± 1	129.8 ± 0.4
3.0	850.5 ± 0.2	976 ± 2	704 ± 3	362 ± 1

Measurements of Juxtaposed SPOFs

The crosstalk can be originated from two independent situations: scintillating photon transmigrating from one SPOF to another or the creation of new scintillation photons in the neighbouring fibres coming from the same light source, due to the superposition of the absorption and emission spectrum (figure 4.2(a)).

During this part, only SPOFs with diameter of 1 mm and 0.5 mm were used. In order to study the SPOF's crosstalk, the parameters of study are:

- Different SPOF's diameter;
- Positioned of the LED Tower in the XT-plaque (see figure 4.13);
- Different collimator's sizes (2.8 mm, 1.8 mm and 0.8 mm).

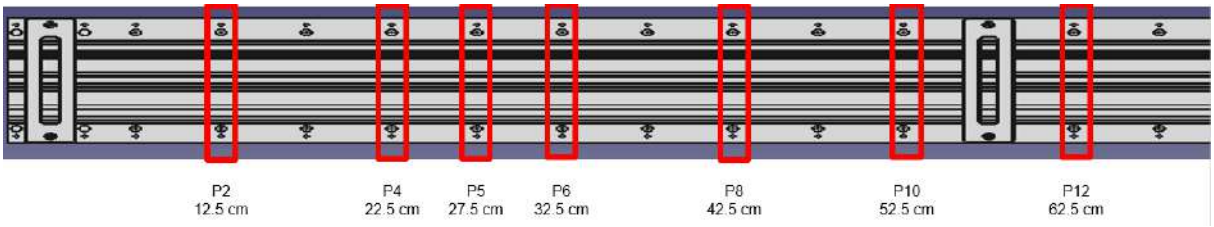

Figure 4.13: Positions studied for the crosstalk.

Figure 4.13 has highlighted in red the tower positions for the crosstalk measurements, including a reference label for the position Pi, being i the position index $i = 1, .., 12$, and the matching distance to the PMT. It is not possible to measure positions after P12, because the cables used to power the LED tower were too short.

In figure 4.14(a), there are four curves overlapped, which illustrates the 1 mm optical fibres response at four different positions for a collimator of 2.8 mm. With the LED Tower moving to each position along the XT-plaque, the signal measured for each SPOF decreases, which was also verified on the longitudinal scans.

Figure 4.14(b) shows how the collimator's size influences the fibrometer system response, as the peaks the peak's width and amplitude gradually shortens with the decreasing size of the collimators. Also, for the results seen in figure 4.14(b), the resulting peaks are shifted due to the way the collimators are made.

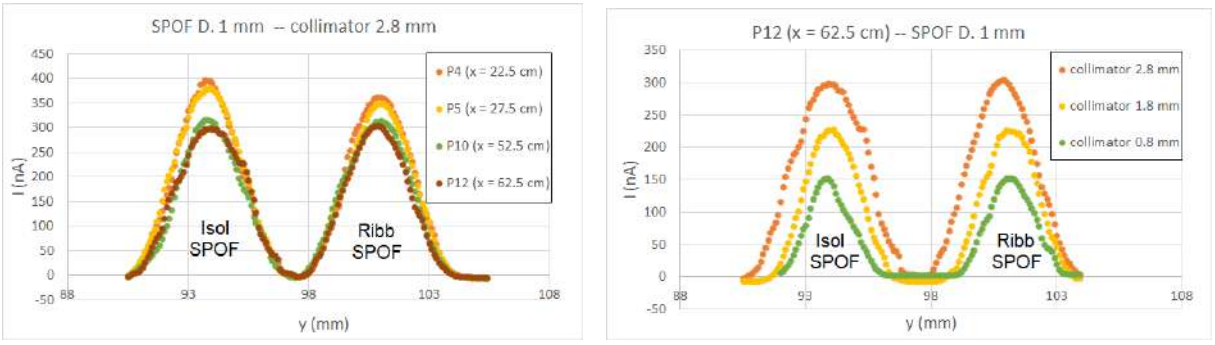

(a) (b)

Figure 4.14: XT-plaque measurements showing for each figure the scan of the isolated fibre and the ribbon for (a) both curves moving at the same pace for different LED tower positions and (b) for different collimators while the LED Tower was fixed on P12.

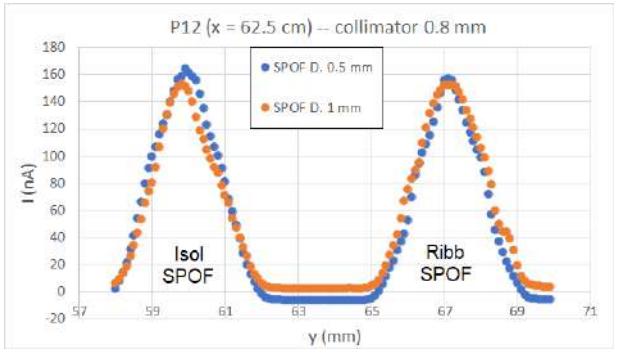

Figure 4.15: XT-plaque measurements showing for each figure the scan of the isolated fibre (on the left) and the ribbon (on the right) for 0.5 mm SPOFs and 1 mm SPOFs, position P12 on the XT-plaque (figure 4.13) and collimator 0.8 mm.

Figure 4.15 shows the fibrometer system response for the 0.5 mm and 1 mm optical fibres for the same collimator.

Prior to any results analysis, a brief discussion over the setup uncertainties is useful, in order to identify their sources and understand the correct procedure for the analysis.

Setup Considerations

Not all uncertainties are related to the conditions of the SPOFs. There is also other factors in question, such as:

- XT-plaque manufacture;
- Dimensions of the collimators;
- Collimator's position;
- Uniformity and intensity of the different light sources (LEDs) used in the comparisons.

Measurements are made in several positions along X-axis of the XT-plaque, as seen in figure 4.13, thus, studying if the plaque manufacture affects the measurements take into account. Figure 4.16 shows the difference between the centre of the Isolated and Ribbon SPOF, which

means the peak's difference. This distance was measured in three different situations: directly from the technical drawing using the FreeCAD software, at the top and end of the XT-plaque and physically using a calliper.

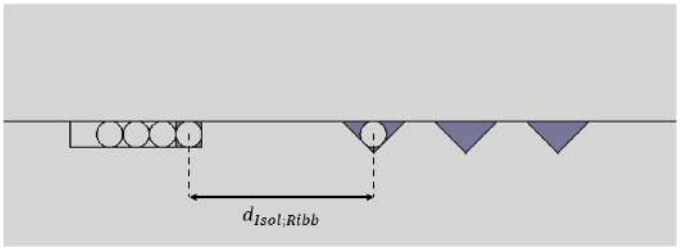

Figure 4.16: Zoomed in the top view end of the XT-plaque with the distance between the centre of the Isolated SPOF to the centre of the Ribbon Isolated.

Table 4.8: Measurements of distance between the SPOF's peaks when positioned in the XT-plaque.

$d_{Isol;Ribb}$ (mm) values for different Measurements Methods	
Measurement Method	$d_{Isol;Ribb}$ (mm)
FreeCAD	7.37
Top	7.11 ±0.02
End	7.30 ±0.02

As seen in table 4.8, the value measure at the end of the XT-plaque is the closest obtained in FreeCAD, but the value between the top and end has a 0.2 mm difference.

Another parameter that might influence the signal is the groove's format. The SPOFs in Ribbon are in u-shape groove while the Isolated SPOF is in a v-shape groove.

The dimension of the collimator's slit can also affect the fibrometer system response. For these measurements, the tower was placed in the same position and several consecutive measurements were made.

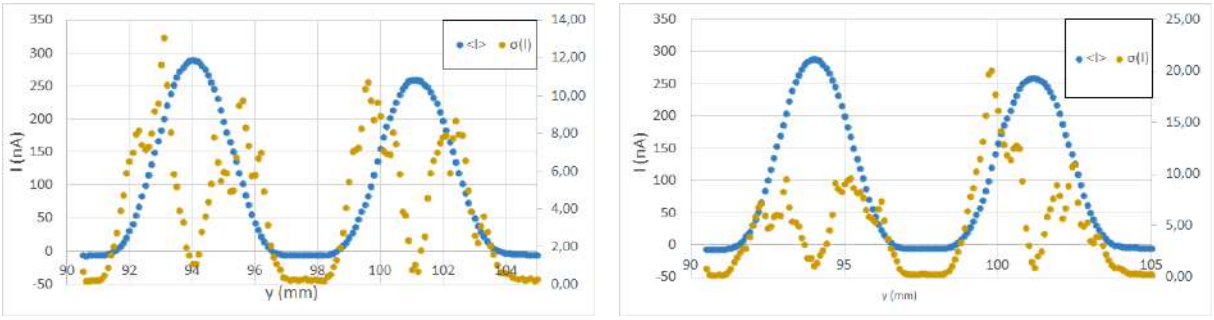

(a) (b)

Figure 4.17: (a)Average output from the fibrometer system of ten measurements on (a) a row and (b) interrupted as function of Y-axis (transverse), the plaque position P4 for the SPOFs diameter of 1 mm, collimator 1.8 mm and powered by a LV source at V_{LED} = 2.685 V with standard deviation and average divided by standard deviation.

In figure 4.17(a), ten consecutive measurements were made. On the second case, it was two sets of five measurements on a row, but between the fifth and six measurement there was an interval of time of approximately 80 minutes, seen in figure 4.17(b). When comparing the

two figures, figures 4.17(a) and 4.17(b), the standard deviation is higher on figure 4.17(b), thus, when doing these measurements, its preferable to make them consecutive. However, both figures display high standard deviation values in the ridges of the curves. It can lead us to believe that those values suffer a higher variation than the values around the peak, which can be correlated to the collimator's dimension and/or the X-Y fibrometer's table motor. Also, concerning the collimator, it might be slightly tilted when put in front of the PMT as well as the position of the slits might vary on the collimators, creating levels of uncertainty on the experimental setup.

Inside the LED's Tower, as seen in figures 3.13, the LEDs are placed in parallel. The LED's were characterised one by one and not mounted on the supports shown in the previously mentioned. In principle it is not expected a difference in the current going across both of the LEDs. However several differences, can indeed produce some difference between the two currents and so the two intensities. In a future study, calibration process with the LEDs mounted on the LED Tower and simultaneously measuring the current on the LEDs during the measurements.

Comparison Between The Crosstalk Results And The Longitudinal Scan Results

The crosstalk results are compared to the results from section 4.1.2. The charts drawn use the maximum values in each peak of the crosstalk study.

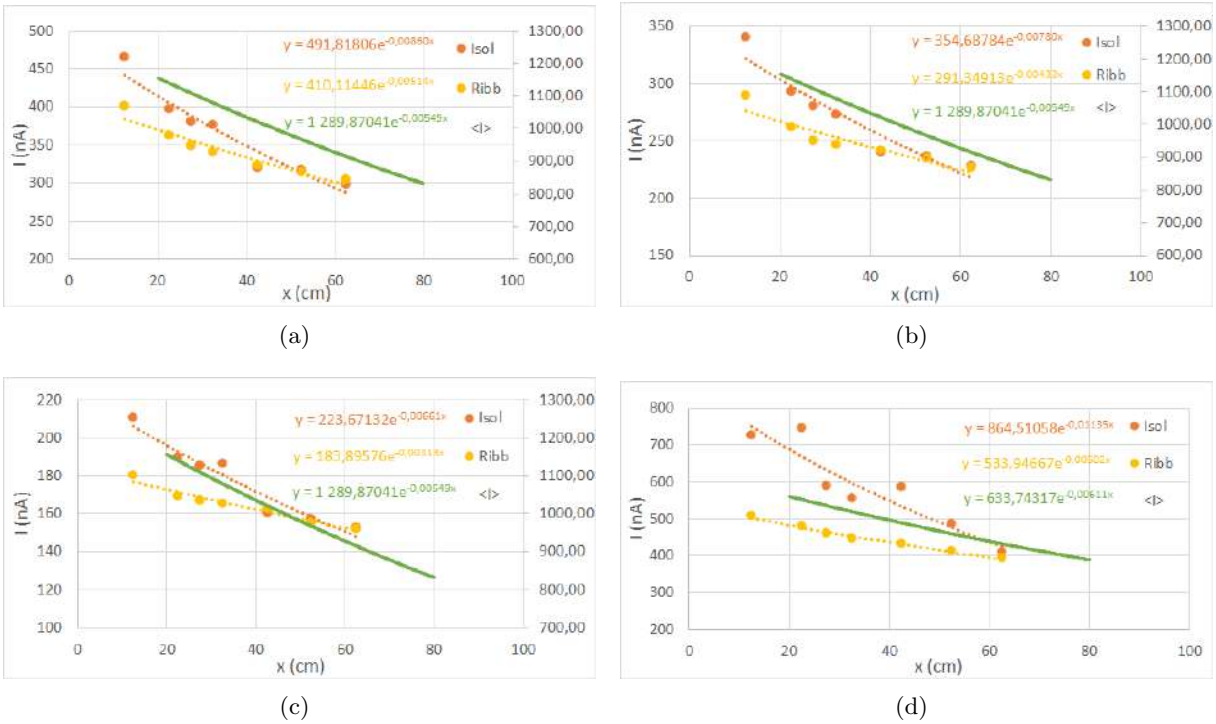

Figure 4.18: Comparison of the maximum results obtained during the transverse scans performed with XT-plaque in the crosstalk study (orange for Isolated SPOF and yellow for Ribbon SPOF) and the curves from the longitudinal scan (LS) for 1 mm SPOFs for (a) collimator 2.8 mm and (b) collimator 1.8 mm (c) collimator 0.8 and (d) for 0.5 mm SPOFs.

For this study, all cases mentioned were compared with all SPOFs in X-Y plaque, but here there only be shown comparisons done with S1 (1 mm) and S11 (0.5 mm) on the X-Y plaque, which were the examples chosen in the section 4.1.2. In charts 4.18, the curve from the longitudinal scan (green coloured on every image) was made with a collimator measuring 15×2.8 mm^2.

For 1 mm, the fibres response overlaps at around 40 cm, whereas for the 0.5 mm, it happens much farther, at about 60 cm distance from the PMT. To each curve there is the exponential tendency line with the equation, $y = a \times e^{-b \cdot x}$, where $b = \frac{1}{L_{at}}$. To dissect the behaviour of the curves on the charts 4.18, we will compare their $1/b$ values, in table 4.9.

Table 4.9: Comparison between exponential parameter $1/b$ for all SPOFs.

Comparison between exponential parameter, $1/b$, from $y = a \times e^{-b \cdot x}$									
For 1 mm SPOFs							For 0.5 mm SPOFs		
LS S1	collimator 0.8 mm		collimator 1.8 mm		collimator 2.8 mm		LS S11	collimator 0.8 mm	
	Isol	Ribb	Isol	Ribb	Isol	Ribb		Isol	Ribb
182.1	151.3	319.5	128.2	230.9	116.3	194.6	163.7	88.1	199.2

The results show that the signal from the longitudinal scan is closest to the Ribbon signal. The only case where this does not happen is for the collimator 0.8 mm, in figure 4.18(d). In order to guide us in the analysis of the data from fibres in a ribbon, and how to interpret the data, their response is compared with a curve which has a similar behaviour. A simple option is to use Gaussian distributions.

Simulation of SPOF Response and Crosstalk Effects Deformation

Gaussian distribution [74], the mathematical representation of a normal distribution, is a bell-shaped curve, which results from an experimental measurement, arrange themselves around a mean value with a characteristic standard deviation and particular amplitude, such as:

- Mean ± 1 Standard Deviation contain 68.2% of all values.
- Mean ± 2 Standard Deviation contain 95.4% of all values.
- Mean ± 3 Standard Deviation contain 99.7% of all values.

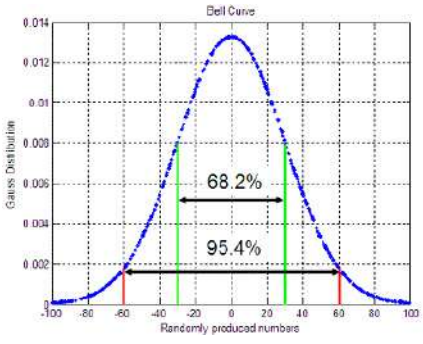

(a)

```
mean = 0; std = 1; variance = np.square(std)
x1 = np.arange(-5,5,0.01)
y1 = np.exp(-np.square(x1-mean)/2*variance)/(np.sqrt(2*np.pi*variance))
```

(b)

Figure 4.19: (a) A normal distribution showing percentage of values within a certain standard deviation from the mean [75] and (b) extract from the code used to create normal distributions.

A typical normal distribution is seen in figure 4.19(a). While placing the fibres in a ribbon if there is enough light being produced or transferred to the neighbouring fibres, a change in the response is expected. This effect could be reproduced by superimposing different normal

distributions, their mean values shifted by the fibre diameter and with diverse amplitudes. As a guide to the experimental data analysis, a numerical approach using the comparison between two curves in different situations are going to be used. Using the PYTHON programming language, with the library numpy, the code seen in figure 4.19(b) was produced. For the X-axis values, it is applied the numpy function of np.arrange(), which generates values within the half-open interval with the stated number of spacing steps in between. On Y-axis, it is applied the normal distribution equation:

$$f(x) = \frac{1}{\sigma\sqrt{2\pi}} e^{-\frac{1}{2}(\frac{x-\mu}{\sigma})^2} \tag{4.3}$$

where μ is the mean and σ is the standard deviation. Signal should be well separated from the background noise, therefore it was defined as region of interest (ROI) above $\frac{3}{4}$ of the maximum for each peak, or, as it will be mentioned from this point on this thesis, Y_{max}. For each situation, the process is the same and it follows the next steps:

1. Generate two normal distributions using the code in the figure 4.19(b);
2. Normalisation to its maximum for each curve;
3. Analysis of the ROI for each curve;
4. Calculation the difference between the two graphs.

Initially it was studied simple situations, using only two curves:

- Case One: equal overlapping normal curves;
- Case Two: equal normal curves, but distanced;
- Case Three: different σ.

In figures 4.20 and 4.21, there will be two curves: c1 (blue line) and c2 (orange line). The curve c1 remains the same for the three cases.

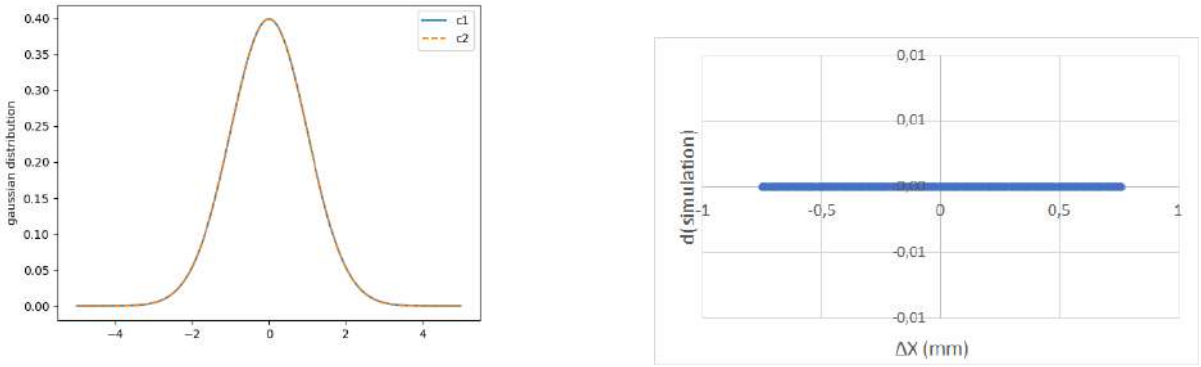

(a) (b)

Figure 4.20: (a) Overlapping normal distributions and the (b) respective difference curve between the curves for each case.

The figures 4.20(a) and 4.20(b) represent the baseline for the crosstalk study. Since the curves are equal, it is expected the difference between curves to be zero, as seen in figure 4.20(b).

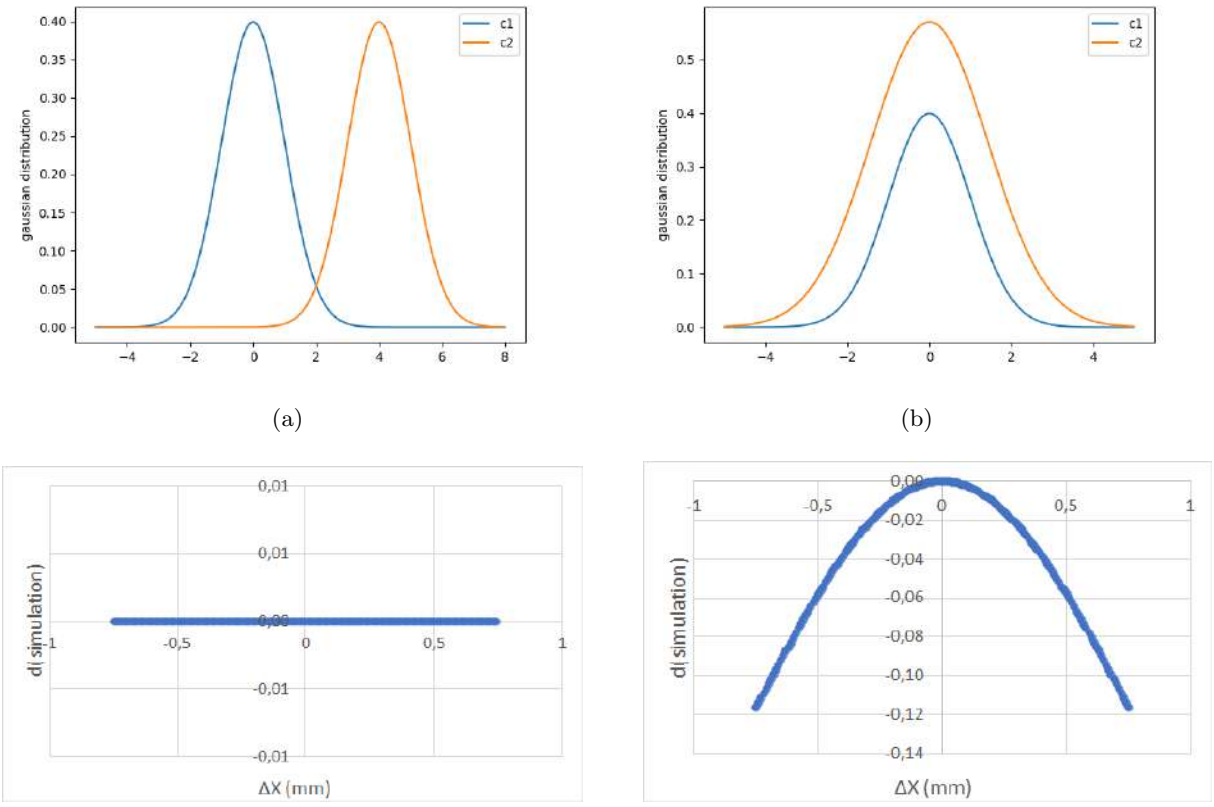

Figure 4.21: (a) Phased normal distributions and (b) Different curves and the (c) and (d) respective difference curve between the curves for each case.

The case two, the figures 4.21(a) and 4.21(c), simulates a similar situation as seen in figures 4.14. To analyse these curves, it was developed the following process to guarantee that we are comparing the same ROI and the same behaviour. This process is drawn in the image 4.22 for a clearer reading and the steps described in its caption.

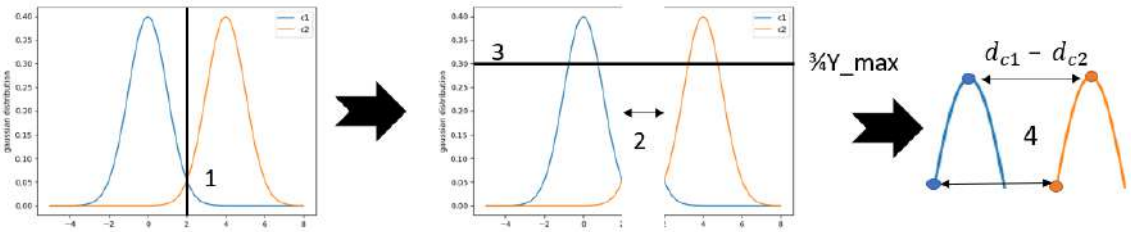

Figure 4.22: Visual representation of the process to analyse the phased curves. First the two curves are separated by their minimum and then, after normalisation to each maximum, it is only focused on the ROI (3/4 of the y_{max}). Next it is matched each crown as it is shown in (4) and then the difference between the two points is calculated.

Resembling the behaviour seen 4.20(b), the difference between the two phased curves will also be zero. The last case, it was generated two different curves (figure 4.21(b)) and the difference between the curves acts as a parabola or X : $Y > 3/4Y_{max}$ (figure 4.21(d)).

In case there is crosstalk present, it can be described as the appearance of a new light source close to the neighbouring source. To simulate this effect, it will be done:

1. Generate c1 and c2, like the case two above (phased normal distributions);
2. Introduction of a third curve, c3, phased a 1 mm from the curve c2, with its amplitude a fraction from c2 (5%, 10% and 25%);
3. Sum c2 with c3 (creating a fourth curve, c2+c3);
4. Compare c1 and c2+c3 by subtracting c1 to c2+c3.

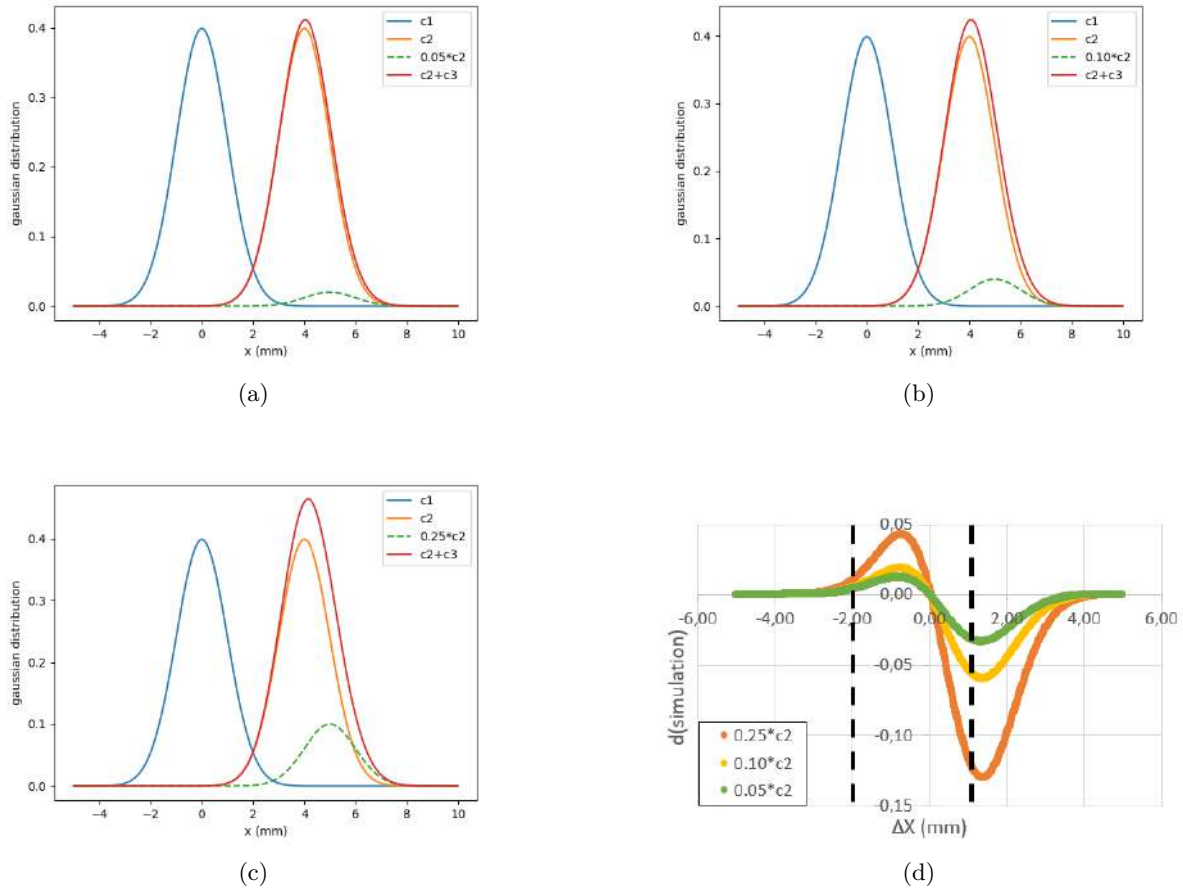

Figure 4.23: Introduction of a third peak phased 1 mm with a amplitude a (a) 0.05 (b) 0.10 (c) 0.25 fraction of the amplitude on the second curve and (d) respective difference curve between the curves for each case as labelled in the legend and the black dashed lines represent the ROI.

Besides increasing the amplitude of the curve (c2), the presence of the third curve (c3) also tilts the maximum of the total of the curve (in red in figures 4.23(a), 4.23(b) and 4.23(c)). This tilting creates an expansion of the right ridge of the curve, therefore the difference between c1 and the fourth curve is expected to have a growing slope on these values. In figure 4.23(d), there is the difference between the curves c1 and c2+c3 throughout their values, with the ROI highlighted between the two dashed black lines. The origin of the chart corresponds to their maximums position. As the multiplying factor increases, so does the difference between the curves, as shown in figure 4.23(d), the right tail has an exponential decline.

These images will be a helpful guide when navigating the following analysis.

4.1.4 Crosstalk Analysis

In the following section, several methods devised to analysed the XT-plaque data from the knowledge acquired on studying the normal distributions comparisons are discussed and explained. These methods aim is to determine if there is crosstalk when the SPOFs are juxtaposed. For this section, we will only focus on the following data: 1 mm SPOFs in P12 for collimators 2.8 mm, 1.8 mm and 0.8 mm and 0.5 mm SPOFs in P12 for collimators 0.8 mm. The position P12 was chosen, because it is where the signal between Ribbon SPOF and Isolated SPOF overlaps as seen in figures 4.18. As it is unsure the reason why, it was decided to analyse only the regions where they overlap.

Approximation Method

This method is the simplest method and it is done using a spreadsheet, following steps:

1. Finding the minimum between curves to separate the Isolated from the Ribbon curve;
2. Select the data in each curve which are considerably far from the background noise;
3. Match the values with a similar behaviour;
4. Calculate the ratios: $r_{Ribb/Isol} = \frac{I_{Ribb}}{I_{Isol}}$;

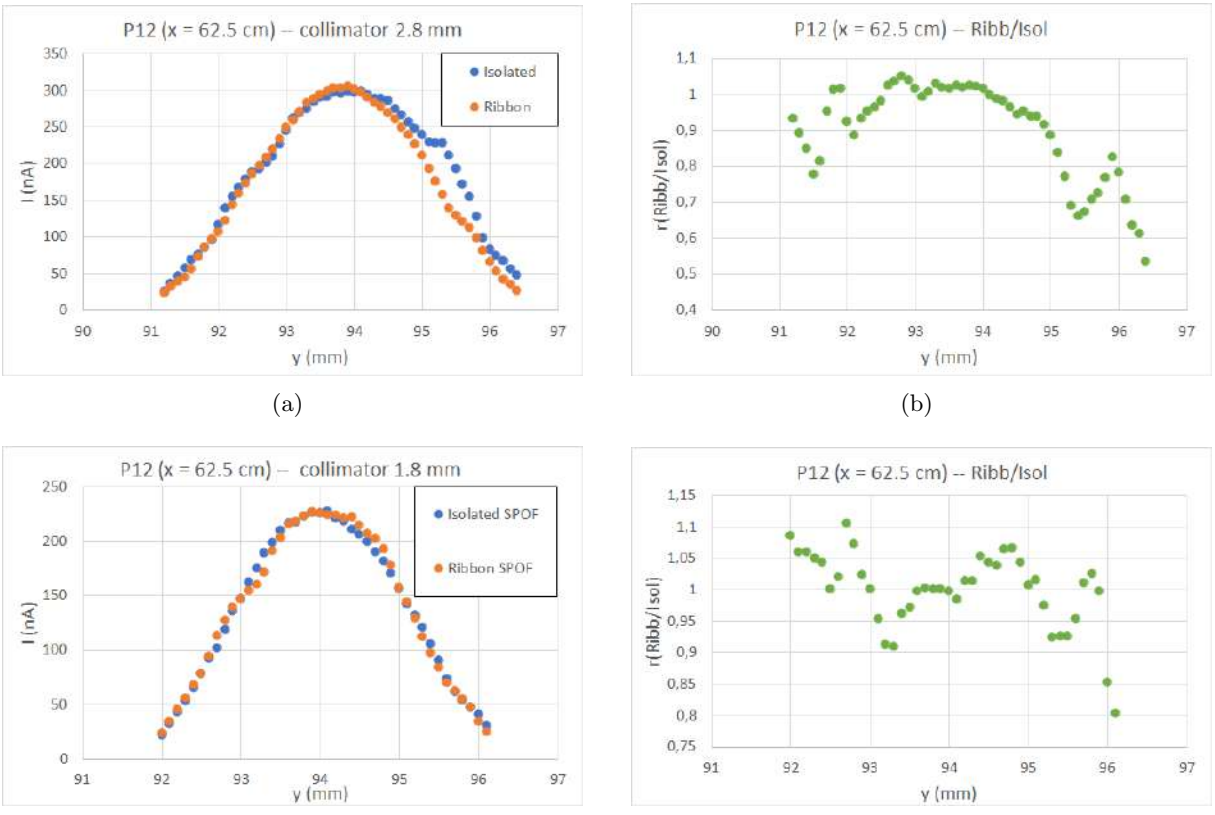

Figure 4.24: Overlap of SPOFs in the position P12 for the collimator (a) 2.8 mm (c) 1.8 mm and (b) and (d) ratio between the signals Ribbon and Isolated SPOFs for each case.

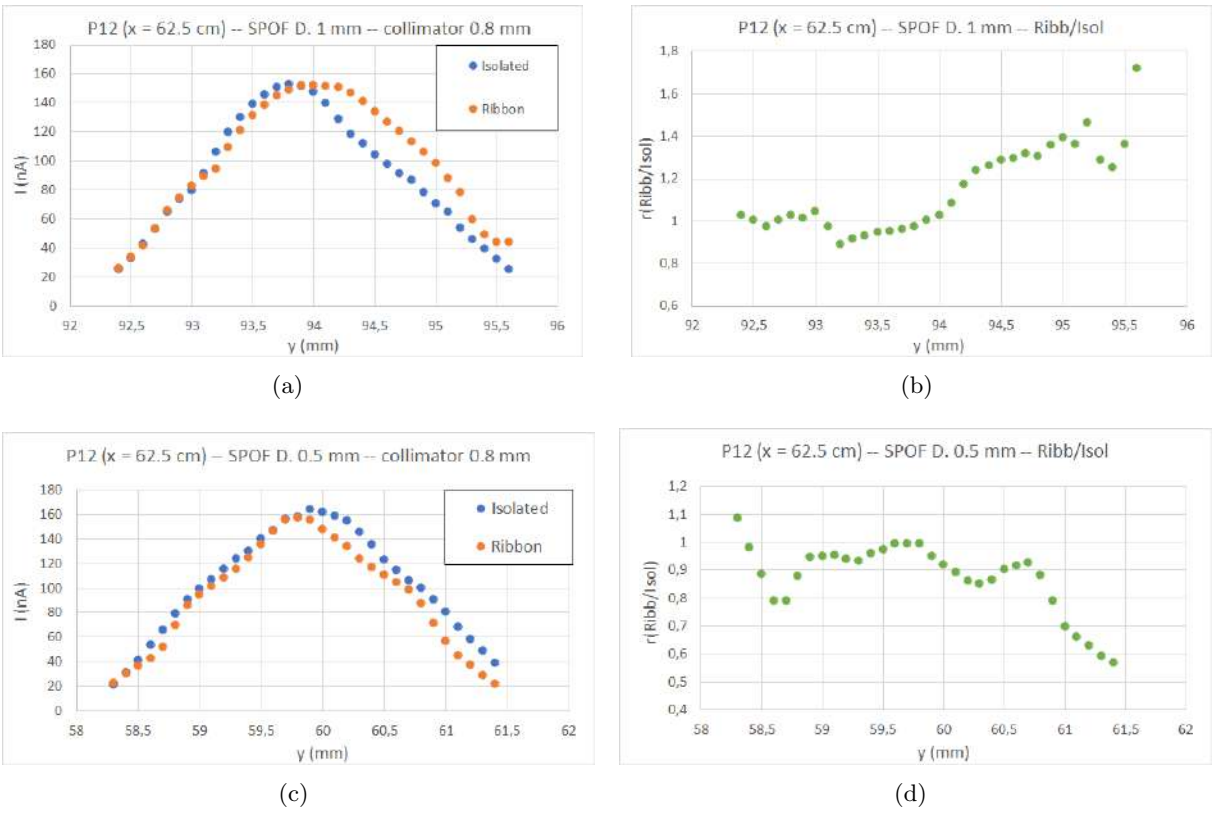

Figure 4.25: Overlap of SPOFs in the position P12 for the collimator (a) 0.8 mm and (c) 0.5 SPOFs and (b) and (d) ratio between the signals Ribbon and Isolated SPOFs for each case.

In figures 4.24 and 4.25, there are the overlapping Isolated and Ribbon curves for the position P12 for all the collimators used and their respective ratios. The visible variation on the curves ridges have already been highlighted before. The curves in figures 4.24(a) and 4.24(c) seem to overlap around the crown region. This is also proved by the ratio graphs, between the positions 93 and 95 mm, i.e, the peak region, is about 1. Outside this region, the ratio value has a higher variation, specially on the chart 4.24(b), where the ratio value almost reaches 0.5. The figure 4.25(a) seems to have other problems, when compared 4.24(a) and 4.24(c). Their ratio is around 1 until the position 94 mm and, then just increases, reaching 1.4 at 95 mm.

Another important detail worth mentioning is that it is not clear why for 1 mm SPOF with 2.8 collimator, the Isolated has a bigger response than the Ribbon and the opposite happens to the 0.8 mm collimator. An explanation for this phenomenon is using a collimator size too big or too small for the SPOF's size in question.

For the case of the 0.5 mm round SPOFs, as seen in figures 4.25(c) and 4.25(d), the ratio shows that around the peak area, between 59 and 60.5 mm, is between 1 and 0.9, while on the ridges can take values between 1.1 and 0.5.

For the theoretical model done, this method should have been enough to quantify the presence of crosstalk. However, the results obtained show that is not true.

Normalised $3/4Y_{max}$ Method

To further analyse the curves, a second method is developed using that followed the next steps:

1. Divide the data into two curves corresponding to Isolated SPOF and Ribbon SPOF;

2. Isolating the data around the crown of each curve ($> 3/4Y_{max}$) to simulate the results obtained in section 4.1.3;

3. Data Normalisation, because the focus of the study is on the curve shape;

4. Generate a parabola to fit the parameters for each curve, using the function; *parabola* from the *curve fit* parameter of Scipy PYTHON library;

5. Calculate the χ^2 Test;

6. Calculate the difference between the Isolated and Ribbon curve ($y_{Isol} - y_{Ribb}$).

If we look at the SPOF curves in figures 4.14 and 4.15 as a whole, they have a behaviour similar to the curves produced by the normal distributions. However, the ROI is only the top crown, it resembles a parabola.

To present the results for this method in the most clear manner possible, the parabola generated using PYTHON (fit data) is represented with a black line, while the red points are the experimental data.

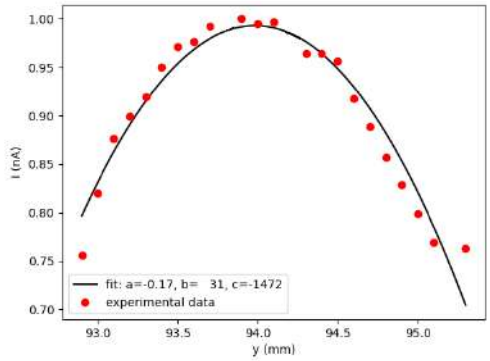

(a) Isolated 1 mm slit 2.8 mm

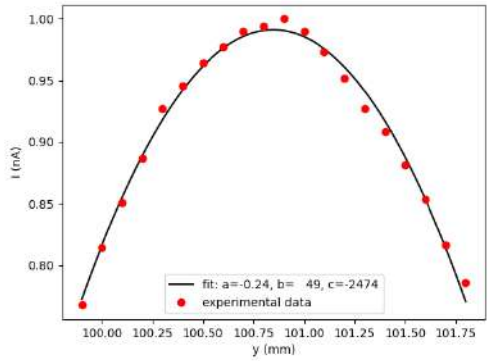

(b) Ribbon 1 mm slit 2.8 mm

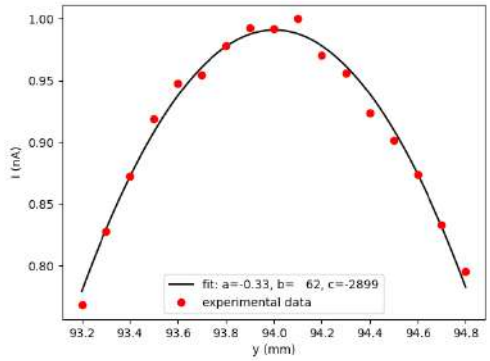

(c) Isolated 1 mm slit 1.8 mm

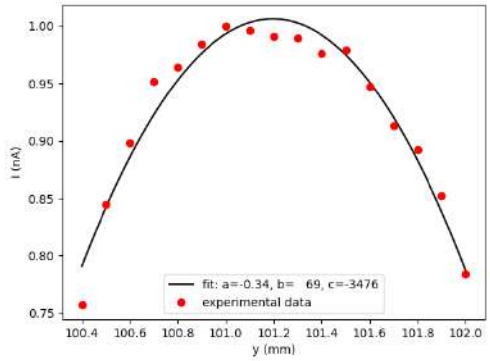

(d) Ribbon 1 mm slit 1.8 mm

Figure 4.26: Simulated parabola for P12 of Isolated SPOF data (a) collimator 2.8 mm and (c) collimator 1.8 mm ; for Ribbon SPOF (b) collimator 2.8 mm and (d) collimator 1.8 mm.

As it is visible in the figures 4.26 and 4.27, there are the charts for all SPOFs and for the three types of collimators used with the fit and experimental data..

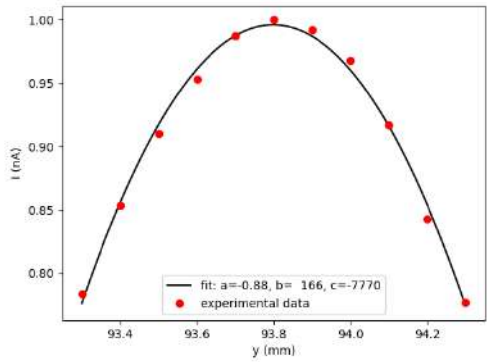

(a) Isolated 1 mm slit 0.8 mm

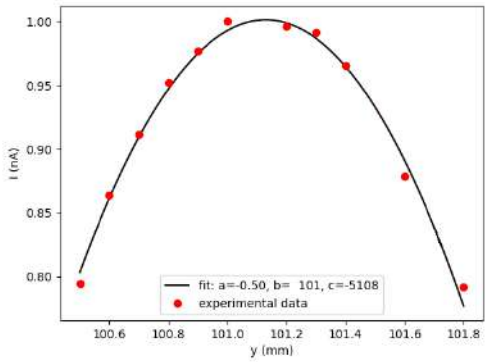

(b) Ribbon 1 mm slit 0.8 mm

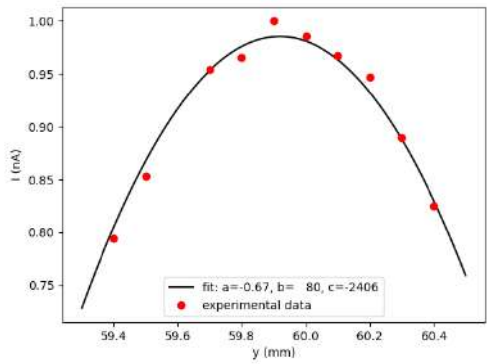

(c) Isolated 0.5 mm slit 0.8 mm

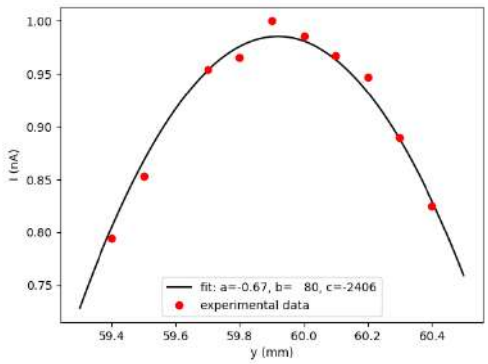

(d) Ribbon 0.5 mm slit 0.8 mm

Figure 4.27: Simulated parabola for P12 for Isolated SPOF data (a) with collimator 0.8 mm and (c) for 0.5 mm SPOFs; for Ribbon SPOF with collimator (b) 0.8 mm and (d) for 0.5 mm SPOFs

To evaluate the quality between the experimental data and the fit data in figures 4.27 and 4.26, it was used the Pearson's chi-squared test, in which the formula used in is:

$$\chi^2 = \sum_i \frac{(O_i - E_i)^2}{E_i} \tag{4.4}$$

where the O is your observed value and E is your expected value. This process was applied individually at each peak in this study (Isolated SPOF and Ribbon SPOF) as it is shown in figures 4.10 and 4.11.

Table 4.10: Results from applying the χ^2 Test to each case of 1 mm SPOF for collimator 1.8 mm and 2.8 mm.

χ^2 for 1 mm SPOFs (10^{-3})								
Positions	collimator 1.8 mm				collimator 2.8 mm			
	P4	P5	P10	P12	P4	P5	P10	P12
Isol	1.71	0.67	2.47	1.06	0.56	0.60	0.59	5.0
Ribb	1.45	2.7	1.01	4.0	4.2	2.7	3.4	0.76

To evaluate the values obtained, we will consult a Chi-Square Distribution Table. This is a

Table 4.11: Results from applying the χ^2 Test to each case of collimator 0.8 mm for SPOFs 1 mm and SPOFs 0.5 mm.

χ^2 for collimator 0.8 mm (10^{-3})								
Positions	1 mm SPOFs				0.5 mm SPOFs			
	P4	P5	P10	P12	P4	P5	P10	P12
Isol	0.68	0.81	0.85	0.44	1.7	0.48	1.7	2.3
Ribb	0.47	0.84	3.1	0.48	1.4	0.81	0.55	1.5

probability table of selected values of χ^2, as it is shown in table 4.12.

Table 4.12: Extract from the Chi-Square Distribution Table [76].

Percentage points of the χ^2 distribution									
Degrees of Freedom	Probability of a larger value of χ^2								
	0.99	0.95	0.9	0.75	0.50	0.25	0.10	0.05	0.01
1	0.000	0.004	0.016	0.102	0.455	1.32	2.71	3.84	6.63
2	0.020	0.103	0.211	0.575	1.386	2.77	4.61	5.99	9.21
3	0.115	0.352	0.584	1.212	2.366	4.11	6.25	7.81	11.34
4	0.297	0.711	1.064	1.923	3.357	5.39	7.78	9.49	13.28
5	0.554	1.145	1.61	2.675	4.351	6.63	9.24	11.07	15.09

The parabolas have three degrees of freedom, because they are defined by three parameters ($y = ax^2 + bx + c$). Then, if we compare the p-value to three degrees of freedom to our values, all of them are lower than the p-value, which means that this method is a good method to be applied with our data.

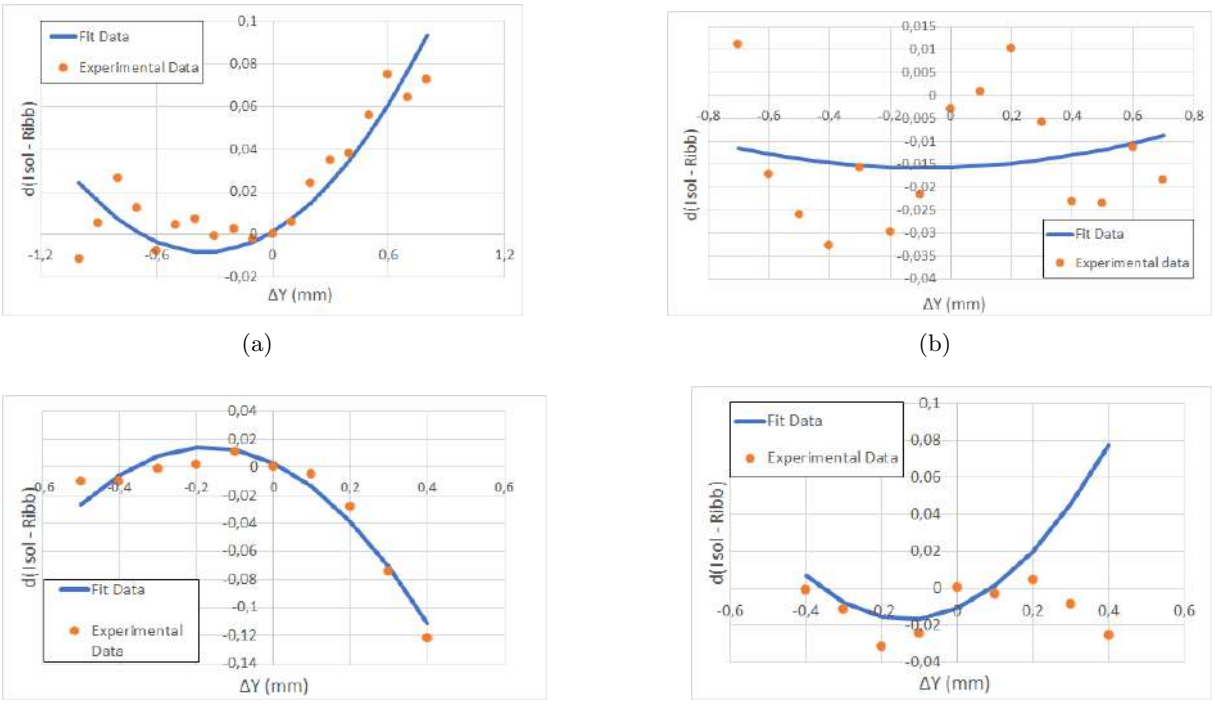

Figure 4.28: Difference calculated for 1 mm optical fibres with collimator (a) 2.8 mm (b) 1.8 mm and (c) 0.8 mm; (d) 5 mm SPOFs.

Now, the final step is the calculation of the difference between the Isolated SPOF and Ribbon SPOF for the experimental data and the fit data, as seen in figure 4.28. Like in the Approximation Method, these charts will be compared with simulations made. In figure 4.28(a), the curve has an increasing slope, because the Isolated Response is bigger than Ribbon Response. In figure 4.28(b), the difference curve does not seem to vary much around the value 0.015. In figure 4.28(c), the difference curve resembles the difference curve in figure 4.23, which could imply the presence of crosstalk. In figure 4.28(d), even though the fit data behaves similarly to the results in figure 4.28(a), the fit data does not match the experimental data like the other graphs show, which is a topic for further future revision.

The two analysis methods compliment each other, since they give two points: the ratio and the difference between the two curves. However, both of them do not give clear results about the presence of crosstalk.

4.2 MAPMT Characterisation

The MAPMT characterisation was made measuring:

- Setup stabilisation;
- Dark current;
- Crosstalk between the photocathode cells when one cell is illuminated;
- Current vs HV MAPMT characteristic;
- Linearity.

The experimental setup is described in detail in section 3.4.3, where it is going to use optical fibres to guide the signal to specific channels and a picoammeter for the measurements. The MAPMT had not been used before, so it is essential to characterise its signal.

4.2.1 Setup Stabilisation

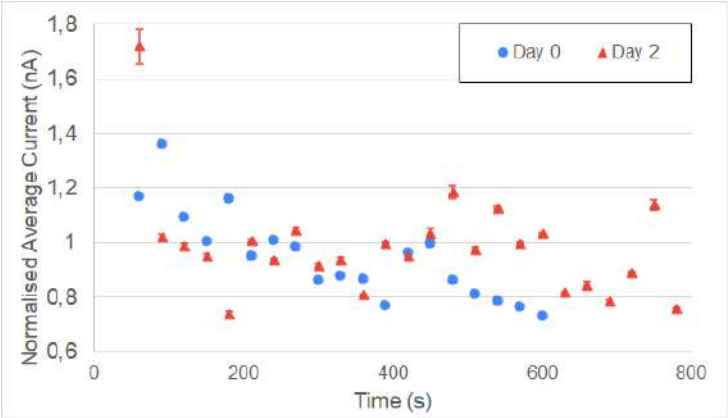

Figure 4.29: Analysis of MAPMT stabilisation for two different measurements. The error bars are, for each side, equal to the standard deviation value given by the picoammeter.

The stabilisation time of any setup is an important factor to take into account since it may affect the measurements carried out. It provides a startup parameter to the experimental setup. In these measurements, the stabilisation was determined with the LED turned off. It was measured the electrical signal produced by the MAPMT at defined intervals of 30 seconds. The MAPMT stabilisation values were measured on two different days, with a day between them. Between those two measures, the MAPMT was kept with the high voltage set to -500 V, which is a standby high voltage for the MAPMT. The values are normalised to their average for an easier reading of the data.

The figure 4.29 shows that during the Day 0 (blue points) with only 600 seconds (10 minutes), it is not enough to state that the system has reached stability. Therefore on Day 2 (red points), the data acquisition was longer and it is visible that after 600 seconds, the MAPMT can be used at any time without losing its stability. Even though the response is approximately constant, their variation is still too high. In figures 4.30, there is the stabilisation with the LED turned on during Day 2 (4.30(a)) and a later on measurement after several days of the MAPMT in use.

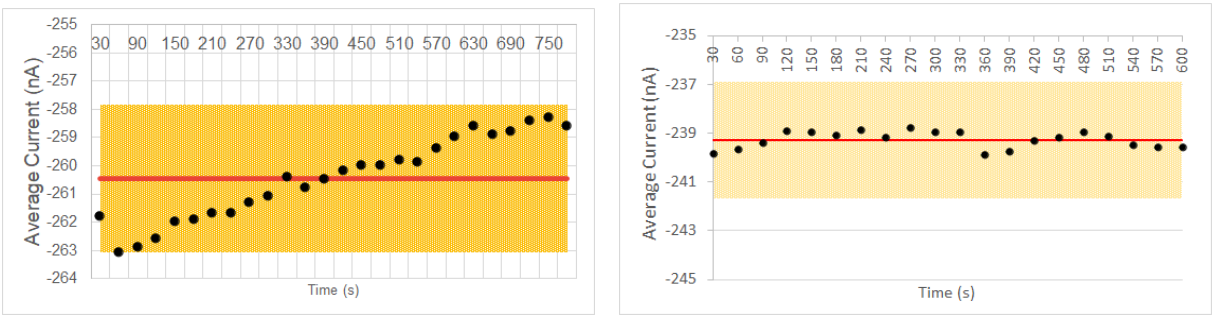

(a) (b)

Figure 4.30: Average current measured on the picoammeter as a function of time (a) as the system LED plus MAPMT stabilises (black points) during day two and (b) a later on measurement. The red line is the total average and the yellow bar show that all values a 1% error range.

By comparing the two charts, it is visible that the setup becomes more stable with time in usage. In order to guarantee that all the following MAPMT measurements, a waiting period of 600 seconds (10 minutes) is established to minimise any residual uncertainties present in the MAPMT.

4.2.2 Dark Current

The dark current is defined as the electric current produced by the charges inside the photodetector when no outside radiation is present. For this measurement, one of the anode channels is chosen and it is taken the value of the electric current produced, doing a series of 1000 measurements. The noise measured for typical operation high voltage values of -900 V and -1000 V is on the following table 4.13. From figure 3.17(b), it is visible that the supply voltages chosen, have higher gain, which is the reason why they were chosen.

4.2.3 Crosstalk Between the Photocathode Cells with One Cell Illuminated

Electrical crosstalk indicates how accurately the light (signal) incident on a certain position of the photocathode is detected while still retaining the position information. Although MAPMT also possesses optical crosstalk, this type of crosstalk is expected to be minimised by the setup

Table 4.13: Measurement of the MAPMT's dark current for different supply voltage.

I ± Standard Deviation (nA)	
HV = - 900 V	- 0.143 ± 0.002
HV = - 1000 V	- 0.682 ± 0.033

itself. Since the fibre (1mm diameter) is located at the centre of each channel (6x6 mm^2) and placed at a distance of about 1 mm of the photocathode face it is expected that the direct light reaching neighbouring channels is minimised.

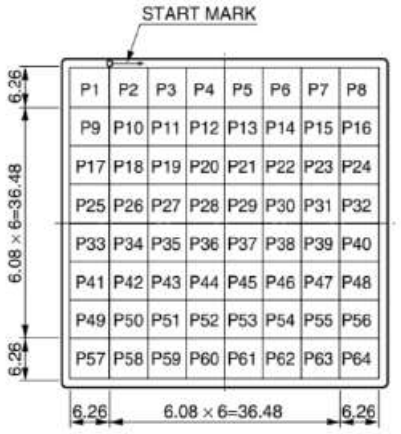

Figure 4.31: The layout of the MAPMT photocathode cells.

As shown in figure 4.31, not all cells have the same dimensions, the extreme ones are larger than the others. In order to verify if the different dimensions influence the electrical crosstalk measures, it was chosen a cell in the middle (cell 37) and another cell on the first row (cell 1). With the SPOF pointing solely to reference cells, it was then taken the signal from all their neighbours as it is schematised in figures 4.32.

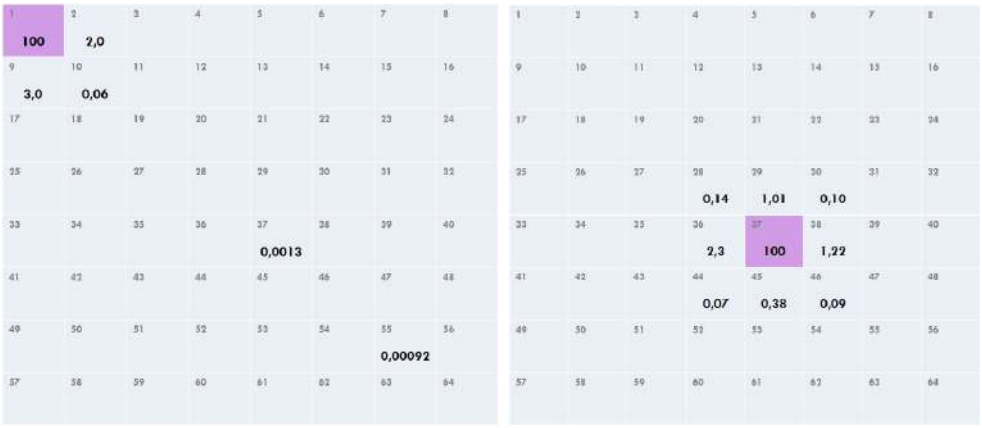

Figure 4.32: Crosstalk values of the MAPMT, the purple square represents the cell of the MAPMT that is being stimulated with an optical fibre, being its value considered 100 u.a.

Since the electrical crosstalk values are less than 3%, it will not be a influential factor on the signal measured nor will introduce a new source of uncertainty to the results. However, it is important to highlight that there is a possibility of these values depend on the intensity of the

light that stimulates the MAPMT as well as depend on the quality of design and manufacture of the connector (see figure 3.20). The design of the connector will influence the distance of the optical fibre to the photocathode cell, the centre of the optical fibre to the centre of the MAPMT pointing cell and minimise external lights, in order to guarantee that the only light that reaches the cells comes from the optical fibres. The quality of the connector's design and manufacture must be further analysed in future studies when the connector design is defined.

4.2.4 MAPMT Current vs High Voltage

The influence of the high voltage (HV) on the MAPMT response was also studied. A LED excited a single optical fiber pointing to MAPMT cell 37 and its response was measured using a picoammeter; the HV noise dependence was also measured for neighbouring cells 28 and 45.

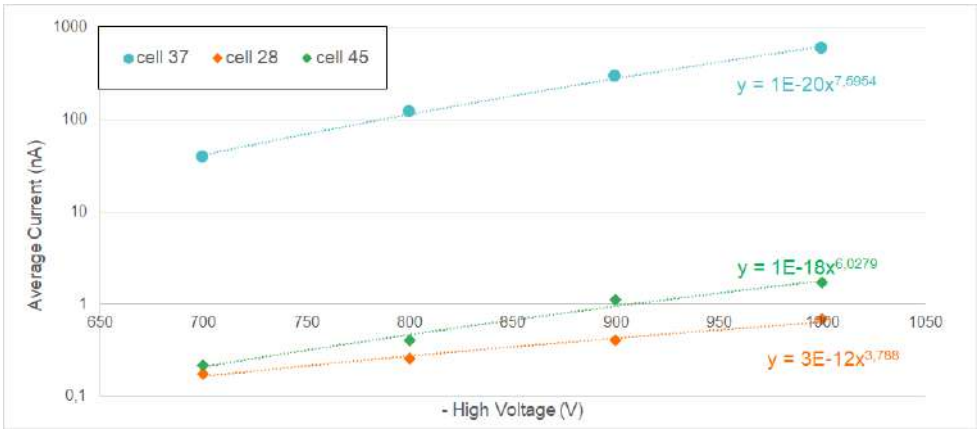

Figure 4.33: Picoammeter measured average and RMS for a cell with fibre (cell 37) and two channels without a fibre (cell 28 and cell 45).

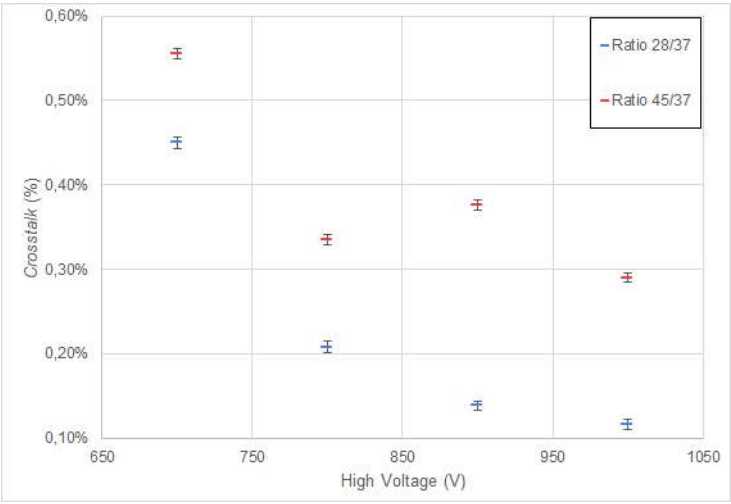

Figure 4.34: Crosstalk (%) measured for HV = [-700,-1000] V.

In the figure 4.33 it is shown the relation between the measured averaged current in relation to the variation of high voltage for the three distinctive photocathode cells already mentioned. Even though the three curves have different intensities, they all follow an expected power function behaviour. The cell 28 and cell 45 curves don't overlap themselves, which is in agreement with

values acquired of the electrical crosstalk (section 4.2.3).

In figure 4.34 are plotted the ratios between the response of the non-stimulated cells 28 and 45 with the response of channel 37. It is seen that both cells show the same decreasing ratio response (electronic crosstalk) with high voltage going from 0.5% (- 700V) to 0.1% (- 1000V).

4.2.5 Linearity

Linearity is measured as the linear dynamic range for different intensities and HV values using neutral density filters. The neutral density filter used were the Kodak Wratten 2 Neutral Density Filters [77] with a featured tolerances of ±10%.

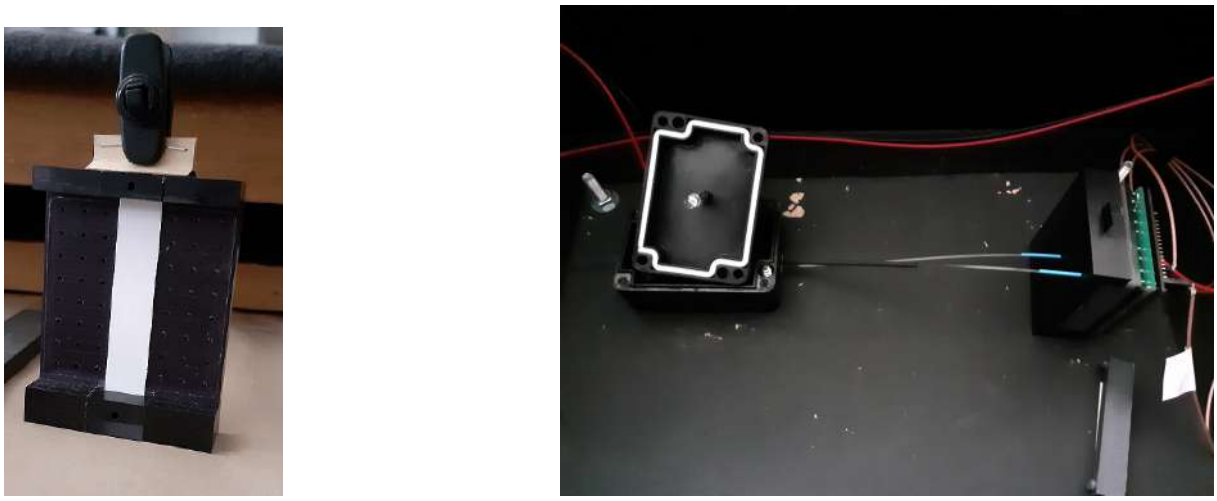

(a) (b)

Figure 4.35: (a) Photograph of the connector to hold the density filters and (b) photograph of the experimental setup for the linearity measurements.

To undergo this test, a new connector[2] was designed to be able cover only the section with the density filter. On the side, was made an hole to allow a neutral density filters to pass across a specific section and held it in a fixed position as seen in figure 4.35(a). The type of filters used reduces light transmission evenly across a specific section. They are described by their optical density (OD), which characterises their ability to stop the emission of light, as seen in the following equation:

$$T((\%)Transmission) = 10^{-OD} \times 100\% \tag{4.5}$$

The full setup for these measurements is seen in figure 4.35(b), where two optical fibres are used. One stays pointing at the MAPMT's cell 1, the baseline for the measurements, since the density filters would not affect this photocathode cell. The other is pointing at either cell 25, cell 28 and cell 32 (see figure 4.31). Between each measurement, the black box has to be open and the density filter changed, which is not an ideal situation. This process requires high precision when removing and putting the density filters, since the rest of the setup cannot move, in particular the SPOFs. If the optical fibres move, the luminosity signal received by the MAPMT would change, thus not being possible to proceed with the linearity measurements and the process

[2]Acknowledgements to Engineer João Martins for making the connector.

must be redone from the start. To prevent the optical fibres from moving, a thermo-retractile sleeve was put close to the tips.

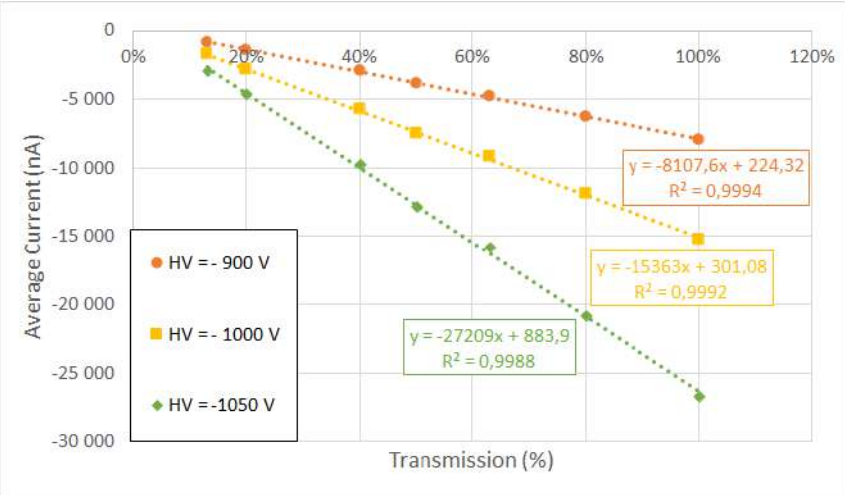

Figure 4.36: Average current measured on cell 25 of the MAPMT as a function of the transmission percentage present on the medium filters for HV = [- 900, - 1000, - 1050] V.

In figure 4.36, there are the results for the three different HV values tested. Although the MAPMT has a maximum of -1100 V, it was used to avoid any damage of the photodetector. To evaluate the data it is used the R^2. The R^2 is a statistical measure, representing how the variation of a dependent variable can be explained by a regression model made of a independent variable. The above linear fits R^2 results show that data agrees within 99% with an linear response for the three different HV analysed.

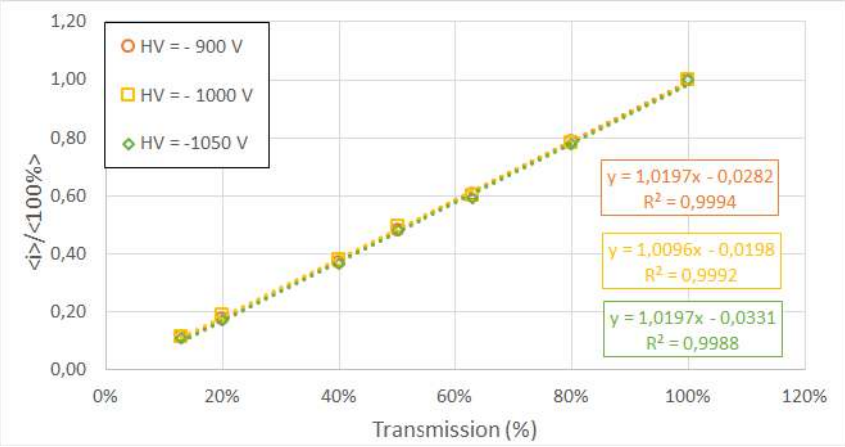

Figure 4.37: Normalised average current measured on cell 25 of the MAPMT as a function of the transmission percentage present on the medium filters for HV = [- 900, - 1000, -1050] V.

In order to compare the curves in figure 4.36, each value was normalised to the values obtained without the density filters. The results are in the following figure 4.37 where the three curves overlap confirming the MAPMT's linearity when varying the HV values.

Next, it was tested 3 different cells along the MAPMT width as it is seen in the figure 4.38. The values do not overlap each other as neatly as in 4.38, specially for cell 32. In the manner the experimental setup is set, cell 32 is in a low position, making it the most difficult position

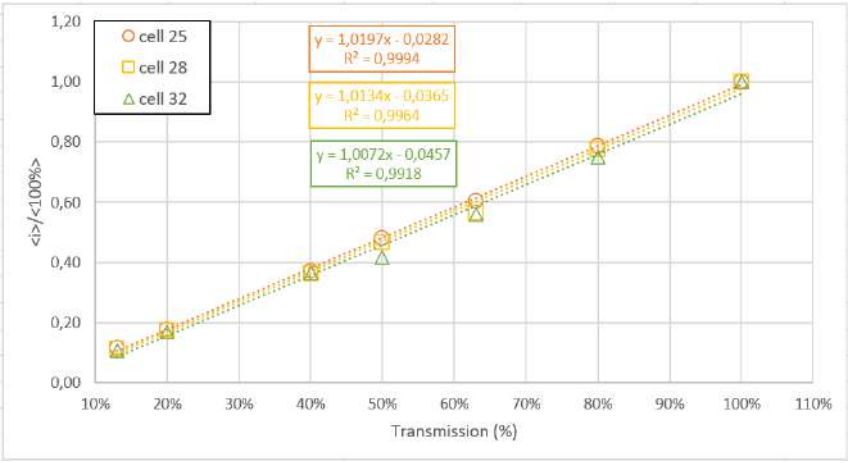

Figure 4.38: Normalised average current measured for HV of −900 V as a function of the transmission percentage present on the medium filters for P25, P28, P32 of the MAPMT.

when trading the density filters. The linearity of all the 3 tested channels are still in agreement above 99% to a linear response for different cells.

To further analyse this values, it was constructed a table with the standard deviation values to each HV value and cells in function of density filter. The absolute deviation from linearity is calculated between the difference of the value expected and the one obtained.

Table 4.14: Absolute deviation from linearity for different high voltages (4.36) and MAPMT's cells seen in figure 4.38

Absolute Deviation (%) for Linearity Measurements						
Transmission	MAPMT's HV values			MAPMT's cells		
	- 900 V	- 1000 V	-1050 V	cell 25	cell 28	cell 32
80%	1.2%	1.8%	2.0%	1.2%	2.5%	4.9%
63%	2.6%	2.8%	3.8%	2.6%	6.4%	7.0%
50%	1.9%	0.6%	1.9%	1.9%	3.4%	8.5%
40%	3.0%	2.1%	3.5%	3.0%	3.7%	3.4%
20%	2.3%	1.3%	2.7%	2.3%	2.7%	3.1%
13%	1.6%	1.8%	2.0%	1.6%	1.9%	2.4%

From the table 4.14 it is seen that the absolute deviation values are lower than 4%. For different cells, we can take that for cell 25, the absolute deviations are lower than 3%. For cell 28, the absolute deviation are lower than 7% and for cell 32 they are lower than 9%. The current understanding is that it cannot be ruled out that this effect does not come from the inadequacy of the setup for this measurements. Although with some outliers typically absolute deviations bellow 5% are observed for theses linearity measurements.

As mentioned before, all these measurements were undertaken using the MAPMT's cell 1 as a control parameter. In figure 4.39, it is shown the average current values normalised to their average throughout the different measurements and the values inside the yellow bar are within a ±5% window. It can be concluded that the linearity measurements are in a reasonable agreement with the errors expected for the typical variations of the setup response.

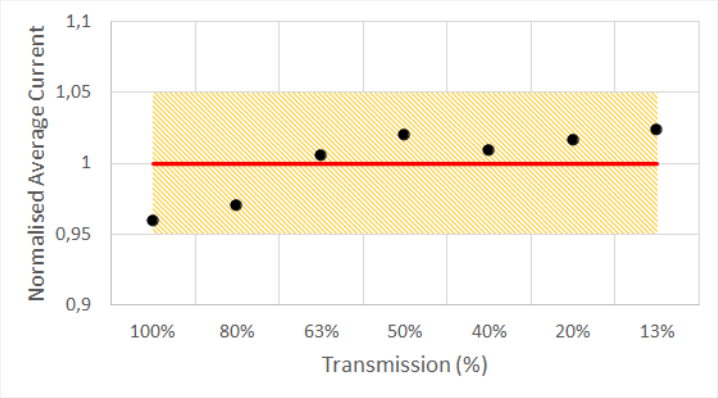

Figure 4.39: Normalised average current measured on cell 1 of the MAPMT as a function of the transmission percentage present on the medium filters for HV = - 900 V. The yellow bar represents a 5% error range.

4.2.6 Light-Tight

During the period these tests were made, the first drawing of the prototype was being made. The question arise whether MAPMT's photocathode cells receive light from other sources besides the fibres facing the MAPMT channels that may in fact result in the increase of the background noise amplitude. The MAPMT readout area is covered with an opaque lid and faces the bottom of the black box previously mentioned. Duct tape was used around the lid as second layer of protection, to evaluate if the external light sources reaching the MAPMT could be adequately concealed.

(a) (b)

Figure 4.40: Photograph of the experimental set up used to study the light-tight on the (a) lateral excitation, before using the duct tape and (b) above excitation, with LED on.

In figure 4.41, there are shown measurements for three situations: lateral excitation without and with duct tape and above excitation.

It is visible in the curves of the lateral excitation and above excitation still show the same response of a typical LED's response, meaning the exponential characteristic curve. The lateral excitation with the double protection of lid and duct tape the response is slightly less prominent, but still displays a curve.

The result of the signal obtained from the above excitation with the lid and duct tape is seen

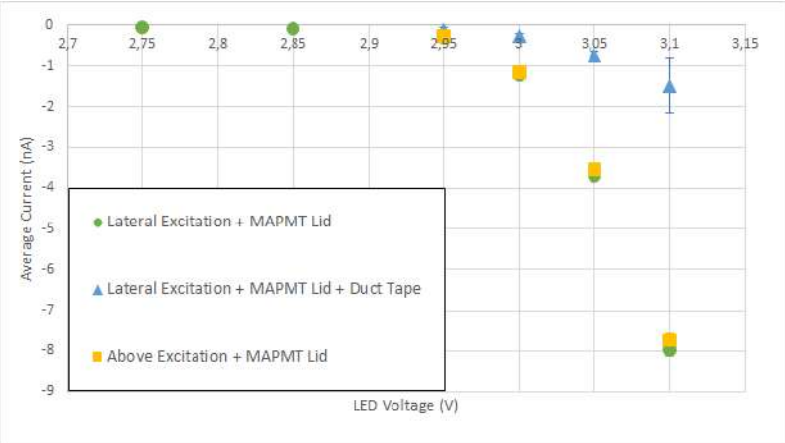

Figure 4.41: Average current measured on cell 1 of the MAPMT as a function of the powering LED value for HV = −1000 V for (a) three distinctive situations: green for lateral excitation plus lid, blue for lateral excitation plus lid and duct tape and yellow for above excitation plus lid.

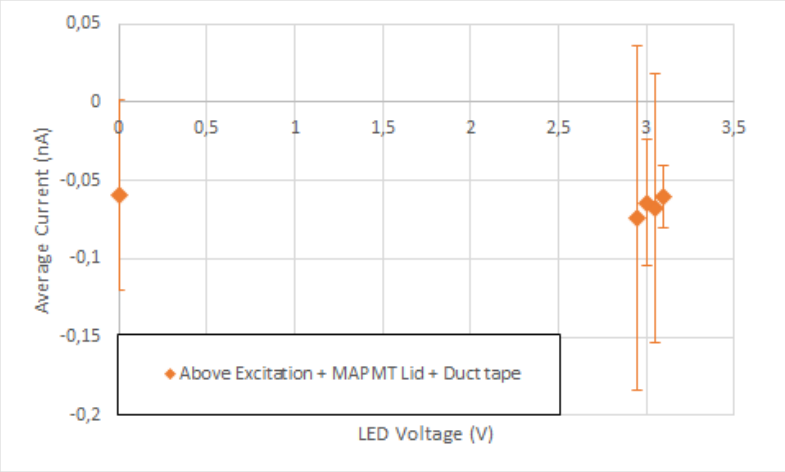

Figure 4.42: Average current measured on cell 1 of the MAPMT as a function of the powering LED value for HV = −1000 V a final situation for above excitation with the MAPMT covered with its lid plus duck tape.

in figures 4.40(b). With the increase of the LED voltage, there is little to none alteration on the MAPMT's response in comparison to the LV being off. Thus, it can be concluded that if the light paths to the readout face are correctly covered and the MAPMT adequately accommodated, the external light on the photocathode's cells doesn't affect with MAPMT's response.

4.3 Integration Tests of the DAQ Board

At this point, the SPOF and MAPMT characterisation is done and the only missing element of the chain is the DAQ Board. For these measurements, the picoammeter is discarded and in its place the DAQ Board is used. The DAQ board characterisation was made measuring the current using the DAQ board as function of:

- Threshold: boundary that separates the signal from background noise;

- Frequency;
- LED's Voltage;
- Number of Acquired Events;
- Types of Radioactive Sources.

During these tests only two channels (channel 44 and 47) could be connected at the DAQ board. Instead of the continuous signal, the LED needed to be powered by a pulse generator, because the DAQ board does not read continuous signal. It is important to first do preliminary tests with LEDs to get an initial understanding of the DAQ board performance, since it is possible to control more parameters. The radioactive sources are the next step since the main goal for the microdosimeter is to be irradiated in beam installations.

4.3.1 Characterisation with LEDs

Firstly, it was study how the threshold works by distinguishing the background ADC Counts from the ADC Counts due to a signal. In figure 4.43, there are two examples of the relation between the events from signal and background.

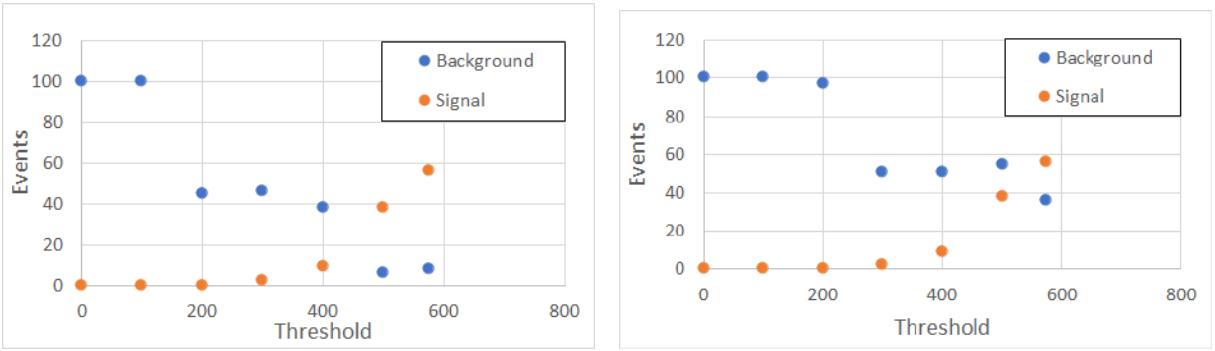

(a) (b)

Figure 4.43: (a) Events as function of threshold values for channel 44 with $V_{LED} = 1.50$ V and (b) Events as function of threshold values for channel 47 with $V_{LED} = 1.50$ V using a LED as light source for the DAQ board for two curves representing the background and signal events.

As expected with a threshold = 0 there is only background noise. However, as the values of threshold increases, the background events consistently decreases while the signal events increases. Eventually, the signal events surpasses the background events at the threshold value of 500 on channel 44. On channel 47, the surpassing occurs on a later stage, indicating more noise on this particular channel. This phenomenon can be explained by the geometry of the setup, by a difference of light yields between the SPOFs used or the SPOF in channel 47 might be slightly away from the photocathode cells. A recommendation results from this result, that all the channels should be calibrated and its thresholds measured.

In the future, this detector will undergo beam testing. From the beam itself, it is possible to study its fluence, type of particles and frequency. At this moment, fluence is not a possible parameter to study, but signal frequency is. In particular the goal is to determine if there or what is the frequency limitations for the DAQ board; again should be noted that small statistics

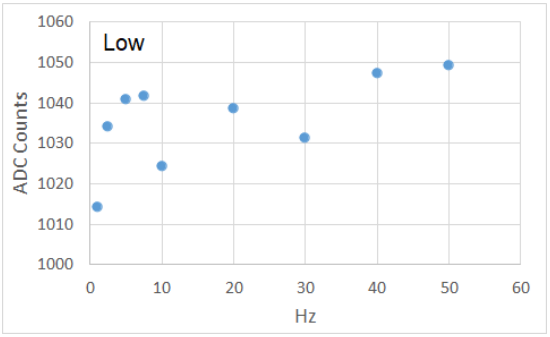

(a)

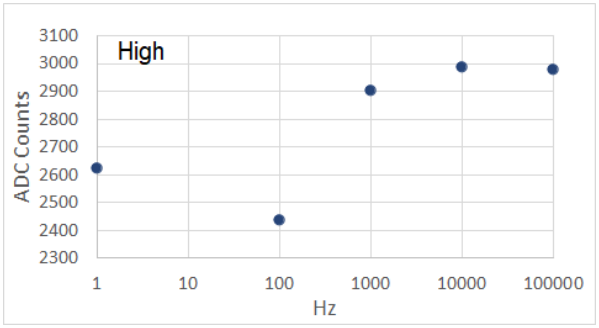

(b)

Figure 4.44: ADC Counts as function of the frequency (Hz) for the channel 44 using the same LED as light source for the DAQ board with a (a) $V_{LED} = 1.055$ V and (b) $V_{LED} = 1.1$ V.

are used. In figures 4.44, it shows how the ADC Counts are influenced in terms of the signal frequency.

In figure 4.44(a) an increasing tendency is seen in the low frequency regime bellow 50 Hz but a variation bellow 10 ADC counts is observed (1%). In figure 4.44(b) the LED voltage was set to 1.1 V. At the LED voltage at 1.1 V, with the increase of the signal frequency, the output signal reaches a saturation point that can have three explanations:

1. With the increase of voltage, the current also increases, which in turn creates more photons and scintillation photons. This leads to the light output becoming independent from the energy loss, the quenching effect mentioned in 2.13;

2. If the MAPMT receives a large intensity light, it can also saturate;

3. The input signal reaching the DAQ board when passing through its slow-shaper can saturate due to either the maximum boundary of the slow-shaper or Wilkinson ADC Counts itself.

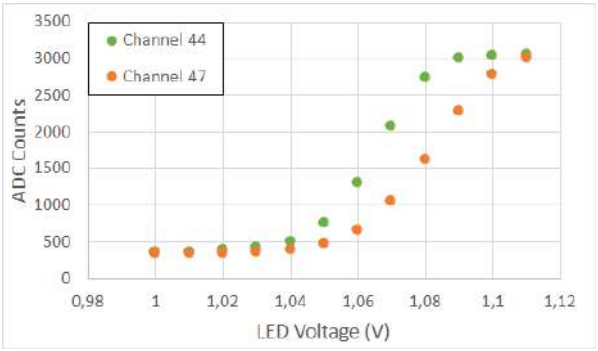

(a)

Figure 4.45: Charge (ADC Counts) as function of LED voltage channel 44 and channel 47 using a LED as light source for the DAQ board.

The final parameter is the dynamic range of the DAQ board using as input the variation of the LED voltage. In figures 4.45, it shows how the ADC Counts depend of the variation of the LED Voltage. Both have an almost exponential growth until it reaches again a saturation point.

4.3.2 Characterisation with Radioactive Sources

In order to conclude the setup evaluation test using radioactive sources were made. In this tests were used a set of radioactive source, which the purchase/production date or the activity was not available: ^{137}Cs, ^{60}Co, ^{204}Tl and ^{241}Am.

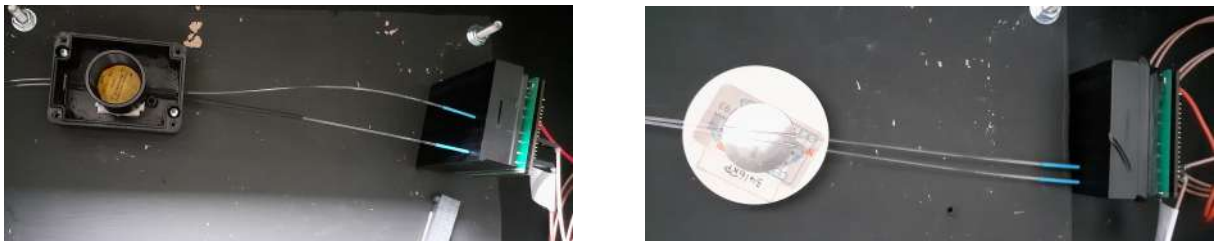

(a) ^{137}Cs (b) ^{241}Am

Figure 4.46: Photograph of the experimental set up used to take the data from (a) ^{137}Cs and (b) ^{241}Am.

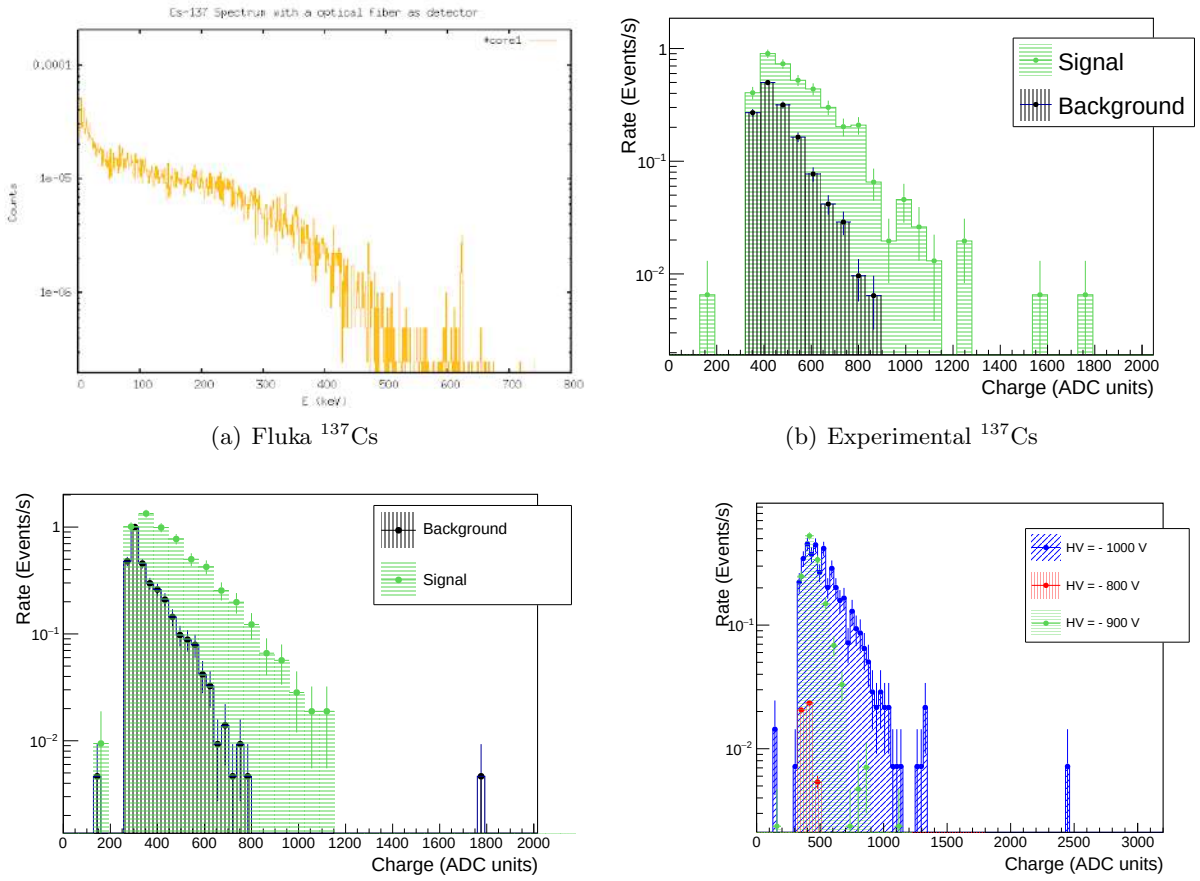

(a) Fluka ^{137}Cs (b) Experimental ^{137}Cs

(c) Experimental ^{137}Cs with D2 (d) Different HVs

Figure 4.47: (a) ^{137}Cs decay spectrum with the optical fibre detector [78]. Events rate as function of charge for a radioactive source ^{137}Cs (green shade) and then background noise (black shade) (b) for D1 HV = -1000 V (c) for the output D2 HV = -1000 V and (d) for D1 and different high voltage values.

In figure 4.46 there is a image with the experimental set up used to take the data from the radioactive sources. For these measurements, besides using different radioactive sources, another

parameters used were the threshold, the output comparator and the HV. It is important to highlight for reference that the activities of the sources are unknown for this study.

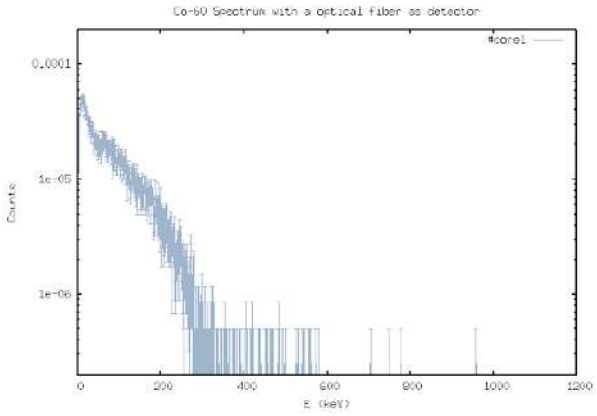

(a) Fluka ^{60}Co

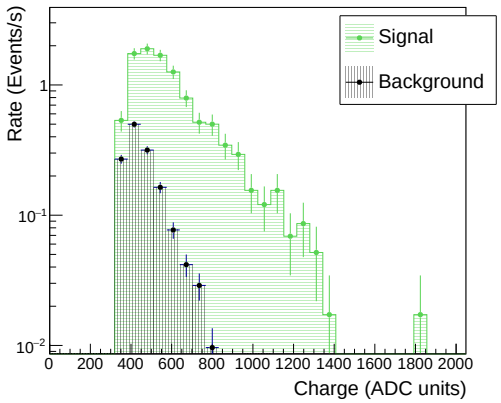

(b) Experimental ^{60}Co

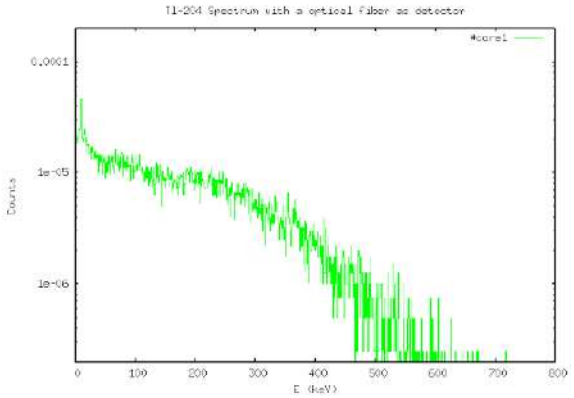

(c) Fluka ^{204}Tl

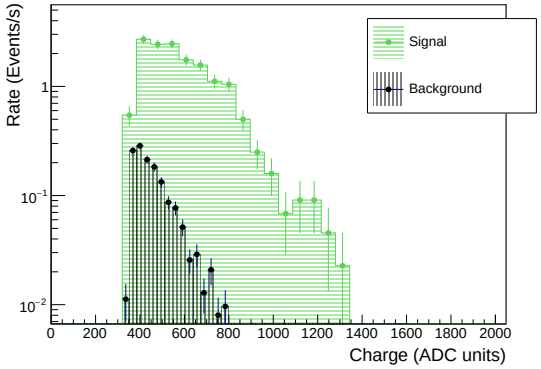

(d) Experimental ^{204}Tl

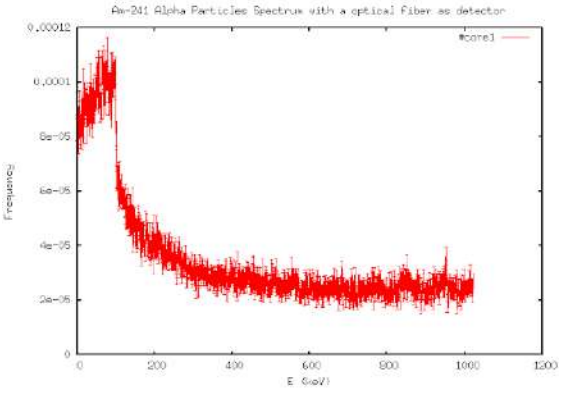

(e) Fluka ^{241}Am

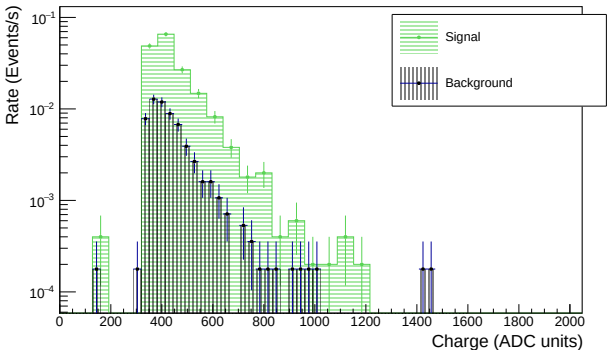

(f) Experimental ^{241}Am

Figure 4.48: (a) ^{60}Co (c) ^{204}Tl and (e) ^{241}Am decay spectrum with the optical fibre detector [78]. (b) Events rate as function of charge for a radioactive source (green shade) ^{60}Co and (d) ^{204}Tl and then background noise (black shade) for D1 HV $= -1000$ V. (f) Events rate as function of charge for a radioactive source Am-241 (green shade) and then background noise (black shade) $HV = -900$ V.

To obtain the background noise results, the tests are made without any radioactive source inside the black box or close in its vicinity. The results are in logarithm format and are compared to the simulations obtained at [78]. For the radioactive source ^{137}Cs was done several tests as

seen in figures 4.47.

The results obtained for the other radioactive sources (figures 4.48(b), 4.48(d) and 4.48(f)) appear to have similarities in their response, but it is difficult to distinguish between the different types of decay as well as the energies associated to them. In principle from the simulation results it should be possible to distinguish the radioactive sources by different end points, which is not observed in experimental data. For these reasons, there needs to be more understanding on the matter, especially validate the simulations, change new parameters of the DAQ board and verify the conditions of the setup. Also, the stopping power of the β and α particles from the tables 3.2 and 3.3 was calculated on different components of the Kuraray SCSF-78 optical fibres. From these calculations it was verified that the α particles do not reach the core of the optical fibres, meaning the signal we are seeing is only the gamma decays from the americium source. For the β particles, these particles at minimum reach the core of the optical fibres. The other three sources were overlapped to compare the different signals as seen in figures 4.49.

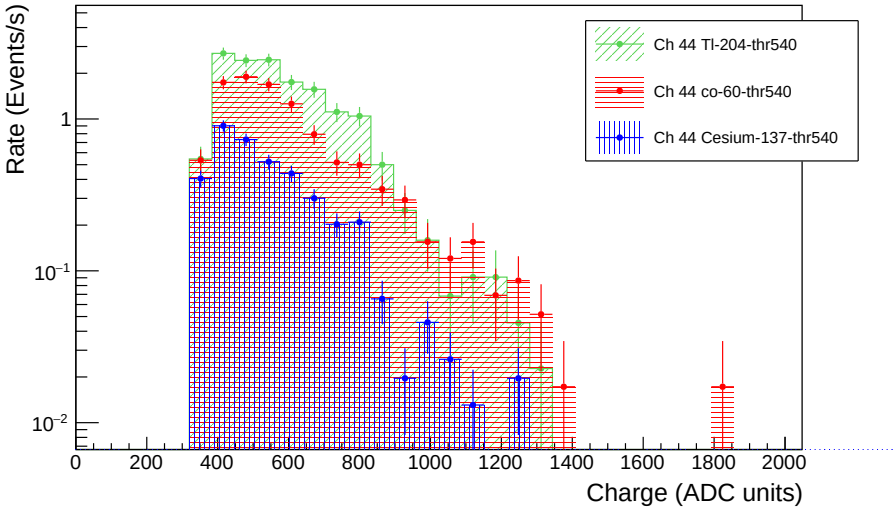

Figure 4.49: Events rate as function of charge for a radioactive source for ^{204}Tl, ^{60}Co and ^{137}Cs.

The thallium source is the source with higher rates of event, which is expected due to the β decay being the most energetic of the three as seen in figure 3.5(d). Then, should be the cesium the most energetic and at last cobalt, because the β decay of cesium is more energetic than cobalt. However, the cobalt γ decays are more energetic then cesium γ decays (see figures 3.5(a) and 3.5(b)).

Chapter 5

Conclusions

The work described in this document follows the characterisation of the full readout chain elements needed for the development of a microdosimeter for radiobiology studies in a proton therapy environment. The detection chain was built using scintillating plastic optical fibres (SPOF), a multi-anode photomultiplier (MAPMT) and a data acquisition (DAQ) system.

The first step was to characterise the performance of the 1 mm and 0.5 mm SPOFs, studying the behaviour of an isolated SPOF and the effects caused when placing them in ribbons. For isolated SPOF, basic properties were studied, such as attenuation lengths (150 to 225 cm for new 1 mm SPOFs and 100 to 160 cm for 0.5 mm) and light yields ($31 - 53\%$ for (0.5/1) mm SPOFs and $44 - 57\%$ for (old/new) 1 mm SPOFs). With this initial measurements it was also understood current difficulties associated with the fibrometers design parameters. These tests revealed that the plaques in the laboratory are not suitable for 0.5 mm, needing extra holders to maintain them positioned over the plaque. Since the future goal for the final prototype is to build the detector with 0.25 mm or even smaller SPOFs, either new plaques have to be designed or try using holders with sponges to hold the SPOFs in place.

For the SPOF's crosstalk study, two methods were developed to compare the response of an isolated fibre with a fibre in a ribbon: Approximation Method and the Normalised $3/4Y_{max}$ Method. The Approximation Method is not precise enough for analysing the curves, only serving for an initial quick comparison between the curves data, whereas the second method is more meticulous. It also allows us to compare the quality of the values with other tests, such as the χ^2 test, where it was verified that the differences between the fit and experimental data are not significant. However, the results are not conclusive to determine the presence of crosstalk nor quantify it. An explanation for this is that the crosstalk signals may be too small for the experimental system sensitivity. Too improve this issue, in the future, there should be the ability to read the optical fibre's signal individually, have more reliable or single homogeneous light sources and have more similar optical fibre's conditions. Furthermore, from the experimental setup two main issues were identified that increased the difficulty in the results analysis: the dependence of the fibre response comparisons on the used collimator and the different groove's shape to place the isolated fibres (v-shape) and ribbons fibres (u-shape). These and other minor issues may need a revised look during future measurements.

From the MAPMT's characterisation results, its performance was analysed by measuring it's crosstalk ($> 3\%$), dark noise, HV dependence for signal, following the expected power law, and cross talk decreasing with HV increase. To conclude linearity tests using neutral density filters were made and, from all the characterisation tests, was the one with most uncertainty

($> 9\%$), since between each measurement, the experimental setup changes with the exchange of the density filter and it is difficult to guarantee the same accurate setup achieved for all MAPMT cells. Moreover, the experimental setup itself is not the most ideal:

- The black box was very large for the current experimental setup which resulted in a larger difficulty during the different characterisation steps and its lid was heavy and if the black box is not carefully closed, the whole setup can be disrupted;
- The holes in the first manufacture connector do not have the same size, which can make the SPOFs not being at the equal distance to the photocathode cells. For the later measurements linearity and DAQ tests an optimised connector was used;
- An easier access to the anode pins at the MAPMT would have facilitated these tests;
- Better support for the MAPMT inside the box, so it does not tumble.

Some solutions for these problems can pass through implementing dedicated cables/wires in all MAPMT's pins through an interface board, thus eliminating the need to open the box to exchange each cell signal and pin in study. For the second point, a solution was implemented by producing a new connector and putting a plastic torus near the tip using thermo-retractile sleeve to set the SPOF at a controlled distanced from the photocathode while placed in the connector pinholes.

At the end, the detection chain was completed with the integration of the DAQ board. The characterisation of the DAQ started with the LEDs measuring and calibrated channels thresholds, frequency response and scanning over the dynamic range of the setup using a pulsed LED. One of the main problems encountered is the saturation of the system, which can be originated from the various elements from detection chain. Also, for every DAQ channel, the threshold must be measured due to the difference results. Then, the LEDs were swapped for radiation sources and the results compared with simulations. Even though the radiation source has an effect on the signal, it is difficult to interpret the results, since the individual decays are not distinguishable.

With this work, it was possible to study the three elements of the readout chain for the construction of the microdosimeter. Having evaluated each of the elements independently, it can be concluded that the present assembly could be used as adequate for a first prototype of the microdosimeter. However, it is necessary to study new approaches for the problems mentioned before, from changes to experimental setups to the creation of new data analysis methods with greater precision and clarity in data interpretation.

5.1 Achievements

During the development of this master thesis, I participated in:

- the 22nd Particles and Nuclei International Conference (PANIC2021) with a poster and follow-up article for Proceedings of Science (PoS);
- Investigator Day in the Faculty of Science of University of Lisbon with another poster;
- Master Classes Particle Therapy as a tutor;
- the LIP Mini-School on Charged Particle Therapy Applications as a speaker.

5.2 Future Work

Detector construction is almost completed, with the detector assembly and volume going through final drawing revisions. The current interface board, only allows two channels to extract data at once. However, the final goal is to have the 64 channels working simultaneously, thus a 64 channels interface board is needed and its design is being concluded. Then, the next step is the testing in beam installations, such as Instituto Português de Oncologia de Lisboa Francisco Gentil (IPO), Hospital Santa Maria and Instítuto de Ciências Nucleares Aplicadas à Saúde (ICNAS), to test prototype performance with X-ray and proton beams, after the test bench gets more optimised.

Bibliography

[1] W. H. Assembly, "Cancer." https://www.who.int/news-room/fact-sheets/detail/cancer. Accessed: 2021-01-30.

[2] H. Paganetti, *Proton Therapy Physics*. 2012.

[3] M. C. Support, "Proton beam therapy." https://www.macmillan.org.uk/cancer-information-and-support/treatment/types-of-treatment/radiotherapy/external-beam-radiotherapy/proton-beam-therapy. Accessed: 2021-06-23.

[4] P. Healthcare, "What is proton therapy for cancer treatment?." https://provisionhealthcare.com/about-proton-therapy/advantages-of-proton/. Accessed: 2021-06-16.

[5] S. Jia, A. Mowlavi, M. Hadizadeh, and M. E. Loushab, "Impact of range straggling and multiple scattering on proton therapy of brain, using a slab head phantom," 2014.

[6] L. Greene, S. Srinivas, S. Park, N. Hatami, T. Nobashi, L. Baratto, A. Toriihara, and S. S. Gambhir, *Novel Designs of Early Phase Trials for Cancer Therapeutics*. 2018.

[7] N. Education, "The relative scale of biological molecules and structures." https://www.nature.com/scitable/content/the-relative-scale-of-biological-molecules-and-14704956/. Accessed: 2021-10-22.

[8] R. Milo and R. Phillip, "How big is a human cell?." http://book.bionumbers.org/how-big-is-a-human-cell/. Accessed: 2021-10-22.

[9] T. Kron, J. Lehmann, and P. B. Greer, "Dosimetry of ionising radiation in modern radiation oncology," 2016.

[10] F. H. Attix, *Introduction to Radiobiological Physics and Radiation Dosimetry*. 1986.

[11] N. Connor, "What is type of radiation dosimeters – definition." https://www.radiation-dosimetry.org/what-is-type-of-radiation-dosimeters-definition/. Accessed: 2021-03-09.

[12] A. Murphy and D. A. G. et al., "Thermoluminescent dosimeter,"

[13] M. Akselrod and J. Kouwenberg, "Fluorescent nuclear track detectors–review of past, present and future ofthe technology," 2018.

[14] M.Weinstein, A. Abraham, A. Tshuva, and U.German, "Investigations of cr39 dosimeters for neutron routine dosimetry," 2004.

[15] G. S. Sahoo, S. P. Tripathy, S. Paul, S. D. Sharma, S. C. Sharma, D. S. Joshi, and T. Bandyopadhyay, "Neutron dose estimation via let spectrometry using cr-39 detector for the reaction ^{9} be (p, n)," 2014.

[16] M. Tecnologies, "Dis-1 dosimeter:user's guide,"

[17] N. Connor, "What is self-reading dosimeter – definition." https://www.radiation-dosimetry.org/what-is-self-reading-dosimeter-definition/. Accessed: 2021-06-08.

[18] S. DOZA, "Thermoluminescent dosimetry (tld)." http://www.doza.ru/eng/catalog/Personal_dosimeters_and_detectors/1094/. Accessed: 2021-10-23.

[19] Timstar, "Radiation film badge (dosimeter)." https://timstar.com/ra105600-radiation-film-badge-dosimeter.html?___store=int&___from_store=uk. Accessed: 2021-10-23.

[20] H. Canada, "Electronic personal dosimeters - technical specifications." https://www.canada.ca/en/health-canada/services/dosimetry/products/electronic-personal-dosimeters.html. Accessed: 2021-10-23.

[21] Britannica, "Ionization chamber." https://www.britannica.com/technology/ionization-chamber. Accessed: 2021-10-23.

[22] M. Wong and D. Bell, "Ionization chamber." https://radiopaedia.org/articles/71248.

[23] C. J. Mertens and et al, "Cosmic radiation dose measurements from the rad-x flight campaign," 2016.

[24] C. Guardiola, D. Quirion, G. Pellegrini, C. Fleta, S. Esteban, M. A. Cortés-Giraldo, F. Gómez, T. Solberg, A. Carabe, and M. Lozano, "Silicon-based three-dimensional microstructures for radiation dosimetry in hadrontherapy," 2015.

[25] F. Rêgo, M. da Conceição Abreu, and L. Peralta, "A scintillating fiber dosimeter for radiology and brachytherapy with photodiode readout," 2011.

[26] L. Beaulieu and S. Beddar, "Review of plastic and liquid scintillation dosimetry for photon, electron, and proton therapy," 2016.

[27] S. Beddar and L. Beaulieu, *Scintillation Dosimetry*. 2016.

[28] W. J. Yoo, S. H. Shin, K. T. Han, D. Jeon, S. Hong, S. G. Kim, H. I. Sim, K. W. Jang, S. Cho, B. G. Park, and B. Lee, "Feasibility study on development of cerenkov fiber-optic dosimeter for radiotherapy application," 2013.

[29] S. et al, "Luminosity measurement at atlas—development, construction and test of scintillating fibre prototype detectors," 2006.

[30] "A large scintillating fibre tracker for lhcb, the fifth annual conference on large hadron collider physics," 2017.

[31] W. Contributors, "Relative biological effectiveness." https://en.wikipedia.org/wiki/Relative_biological_effectiveness. Accessed: 2021-02-06.

[32] W. D. Newhauser and R. Zhang, "The physics of proton therapy," 2015.

[33] T. E. of Encyclopaedia Britannica, "Bremsstrahlung." https://www.britannica.com/science/bremsstrahlung. Accessed: 2021-06-16.

[34] B. Patyal, "Dosimetry aspects of proton therapy," 2007.

[35] H. Paganetti and T. Bortfeld, "Proton beam radiotherapy - the state of the art," 2005.

[36] H. E. S. Pettersen, "A digital tracking calorimeter for proton computed tomography," 2018.

[37] E. Shinohara, "Module 2: The physics of proton therapy." https://www.oncolink.org/healthcare-professionals/oncolink-university/proton-therapy-professional-education/oncolink-proton-education-modules/module-2-the-physics-of-proton-therapy. Accessed: 2021-03-23.

[38] T. C. for Proton Therapy, "How proton therapy works?." https://www.texascenterforprotontherapy.com/proton-therapy/how-does-proton-therapy-work. Accessed: 2021-06-22.

[39] R. Kurohi, "Precision cancer treatment expected by 2020," 2019.

[40] S. Global, "How proton therapy works 1." https://www.sahglobal.com/proton-therapy/how-proton-therapy-works-1/. Accessed: 2021-04-06.

[41] H. Paganetti, A. Niemierko, and et all, "Relative biological effectiveness (rbe) values for proton beam therapy," 2002.

[42] T. S. Underwood and S. J. McMahon, "Proton relative biological effectiveness (rbe): a multiscale problem," 2018.

[43] Y. Kase and et al, "Microdosimetric calculation of relative biological effectiveness for design of therapeutic proton beams," 2012.

[44] W. Contributors, "Proton therapy." https://en.wikipedia.org/wiki/Proton_therapy. Accessed: 2021-02-04.

[45] D. Wang, "A critical appraisal of the clinical utility of proton therapy in oncology," 2015.

[46] A. M. Kligman, "What is the 'true' function of skin?," 2020.

[47] A. Kern, C. Bäumer, K. Kröninger, J. Wulff, and B. Timmermann, "Impact of air gap, range shifter, and delivery technique on skin dose in proton therapy," 2020.

[48] A. Kern, C. Bäumer, K. Kröninger, J. Wulff, and B. Timmermann, "Impact of air gap, range shifter, and delivery technique on skin dose in proton therapy," 2020.

[49] A. Kern, C. Bäumer, K. Kröninger, L. Mertens, B. Timmermann, J. Walbersloh, and J. Wulff, "Determination of surface dose in pencil beam scanning proton therapy," 2020.

[50] T. Pfuhl, F. Horst, C. Schuy, and U. Weber, "Dose build-up effects induced by delta electrons and target fragments in proton bragg curves—measurements and simulations," 2018.

[51] X. Ding, X. Li, A. Qin, J. Zhou, D. Yan, C. Stevens, D. Krauss, and P. Kabolizadeh, "Have we reached proton beam therapy dosimetric limitations? - a novel robust, delivery-efficient and continuous spot-scanning proton arc (sparc) therapy is to improve the dosimetric outcome in treating prostate cancer," 2017.

[52] "Carbon ion therapy: A modern review of an emerging technology," 2020.

[53] W. Contributors, "Scintillation (physics)." `https://en.wikipedia.org/wiki/Scintillation_(physics)`. Accessed: 2021-04-24.

[54] W. Contributors, "Scintillator." `https://en.wikipedia.org/wiki/Scintillator`. Accessed: 2021-04-24.

[55] L. Archambault, J. C. Polf, L. Beaulieu, and S. Beddar, "Characterizing the response of miniature scintillation detectors when irradiated with proton beams," 2008.

[56] T. N. B. Richard C. Jaeger, *Microelectronic Circuit Design*. 4th ed., 2011.

[57] RECOM, "Led characteristics – book of knowledge-8.1." `https://www.eeweb.com/led-characteristics-book-of-knowledge-8-1/`. Accessed: 2021-10-21.

[58] LEDnique, "Iv curves." `http://lednique.com/current-voltage-relationships/iv-curves/`. Accessed: 2021-10-21.

[59] D. W. Ball, "Spectrometer, spectroscope, and spectrograph." `https://spie.org/publications/fg08_p02_spectrometerspectroscopespectrograph?SSO=1`. Accessed: 2021-03-07.

[60] K. G. Cafferty, "Application of bayesian and geostatistical modeling to the environmental monitoring of cs-137 at the idaho national laboratory," 2010.

[61] W. Contributors, "Cobalt 60 decay." `https://commons.wikimedia.org/wiki/File:Cobalt-60_Decay_Schemep.svg`. Accessed: 2021-06-30.

[62] B. Almutairi, S. Alam, T. Akyurek, and et al., "Experimental evaluation of the deadtime phenomenon for gm detector: deadtime dependence on operating voltages," 2019.

[63] D. Malain and P. Kanchana, "Evaluation of radiation safety for ionization chamber smoke detectors containing am-241," 2019.

[64] W. Contributors, "Optical fiber." `https://en.wikipedia.org/wiki/Optical_fiber`. Accessed: 2021-08-15.

[65] K. CO., *Plastic scintillating fibers (PSF)*. 2017.

[66] F. Carvalho, "Conception of a tissue equivalent plastic dosimeter using scintillating fibres for hadronic therapy and space radiation effects studies," 2019.

[67] Hamamatsu, *PHOTOMULTIPLIER TUBES: Basics and Applications*. 2007.

[68] Hamamatsu, "Flat panel type multianode pmt assembly: H8500 series/h10966 series," 2011.

[69] I. Keithley Instruments, *Model 6487 Picoammeter/Voltage Source Reference Manual*. 2011.

[70] R. J. B. Luz, "Development of the instrumentation and readout schemes of marta, an upgrade of the pierre auger observatory," 2020.

[71] P. Assis, A. Blanco, P. Brogueira, M. Ferreira, and R. Luz, "The marta (muon array with rpcs for tagging air showers) front-end acquisition system," 2018.

[72] Łukasz Kapłon., *Technical attenuation length measurement of long plastic scintillators for the total body J PET scanner*. 2017.

[73] L. Pereira, "Optical properties of scintillating materials for high resolution dosimetry using fluka and data," 2020.

[74] A. Dasgupta and A. Wahed, *Clinical Chemistry, Immunology and Laboratory Quality Control: A Comprehensive Review for Board Preparation, Certification and Clinical Practice*. 2014.

[75] Matrixlab, "Gaussian distribution – how to plot it in matlab." `https://www.matrixlab-examples.com/gaussian-distribution.html`. Accessed: 2021-09-01.

[76] Plant and S. S. eLibrary, "Chi-square test for goodness of fit in a plant breeding example." https://passel2.unl.edu/view/lesson/9beaa382bf7e/8. Accessed: 2021-10-19.

[77] E. Optics, "Kodak wratten 2 neutral density filters." https://www.edmundoptics.com/f/kodak-wratten-2-neutral-density-filters/13485. Accessed: 2021-10-19.

[78] M. Gamboa, "Study of a scintillant fibers microdosimeter on different radiation environments using fluka code," 2021.

Appendix A

Normalised Transverse Scan

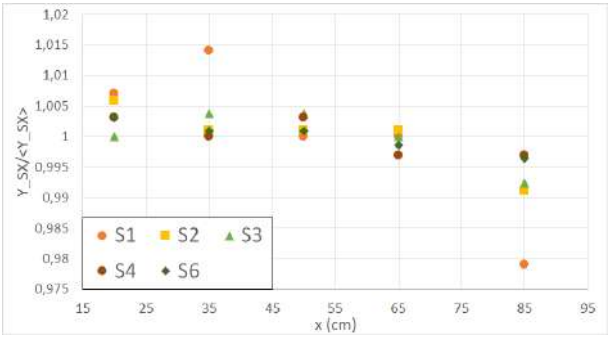

(a)

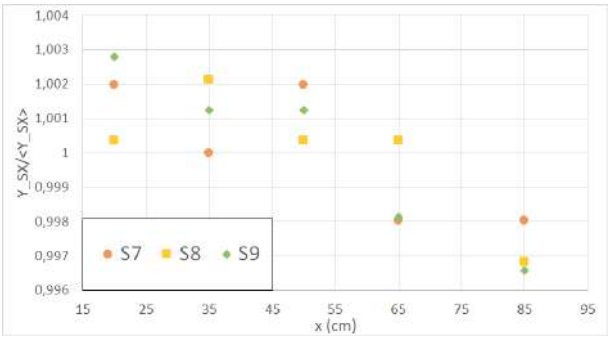

(b)

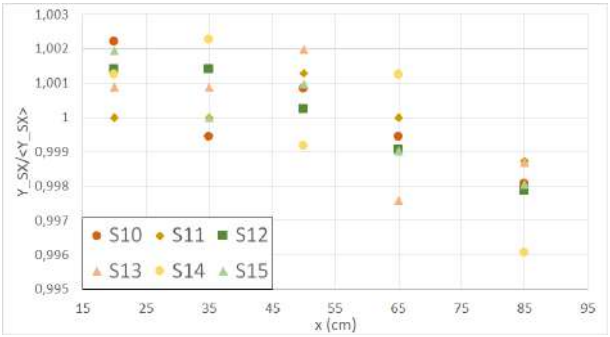

(c)

Figure A.1: Normalised values of the maximum Y-axis position as function of the distance of the excitation source to the PMT for (a) 1 mm SPOFs from 1 to 6 (b) 1 mm SPOFs 7 and 8 and WLS Y-11 and (c) 0.5 mm SPOFs from 10 to 15.